UNIVERSITY OF OKLAHOMA

GRADUATE COLLEGE

STUDY OF FLUID DYNAMICS EFFECTS FOR LOSS OF WELL CONTROL INCIDENTS IN SUBSEA WELLS

A DISSERTATION

SUBMITTED TO THE GRADUATE FACULTY

in partial fulfillment of the requirements for the

Degree of

DOCTOR OF PHILOSOPHY

By

RAJ KIRAN
Norman, Oklahoma
2019

STUDY OF FLUID DYNAMICS EFFECTS FOR LOSS OF WELL CONTROL INCIDENTS IN SUBSEA WELLS

A DISSERTATION APPROVED FOR THE
MEWBOURNE SCHOOL OF PETROLEUM AND GEOLOGICAL ENGINEERING

BY

Dr. Saeed Salehi, Chair

Dr. Prakash Vedula

Dr. Ramadan Ahmed

Dr. Catalin Teodoriu

Dr. Siddharth Misra

Dedication

I dedicate this PhD dissertation to God, my wife: Mrs. Neha, my parents: Mrs. Saroj Devi and Mr. Harendra Prasad Singh, and my siblings: Mrs. Priyanka Singh, Mrs. Sweta Rai, and Mrs. Manisha Singh.

Acknowledgment

I express my gratitude to Almighty for providing me a conducive environment for learning and apply it to complete my research work. My profound gratitude and appreciation go to my committee chair, Dr. Saeed Salehi. He has helped and motivated me throughout my journey of graduate school. Dr. Salehi has provided me every possible opportunity to learn and excel in my professional endeavor. He has mentored and taught me the nuances of technical writing and eventually helped me in publishing my research work. He has always encouraged me to participate me in local, national, and international conferences, symposiums, and meetings. I will always feel honored to have a mentor like you. Words will never be enough to describe your role in my story.

I would like to thank all the members of my dissertation committee for accepting to be in the committee and their time. Beginning with the outside committee member, Dr. Prakash Vedula (PhD), your guidance and insights were very useful. A special word of gratitude to Dr. Ramadan Ahmed (PhD), who has made this work possible. In addition, a thank you to Dr. Catalin Teodoriu (PhD), and Dr. Siddharth Misra (PhD). The contributions and feedbacks you all gave throughout my research were extremely valuable.

It was an honor to have worked closely with Mr. Jeff McCaskill at the OU Well Construction and Technology Center (WCTC). The experimental work would not have been possible without your help. Thank you for being there when I needed most.

I am also grateful to the Mewbourne School of Petroleum and Geological Engineering for granting me scholarships and travel awards to support my studies and research presentations. This acknowledgment is incomplete without the mention of Dr. Chinedum Ezeakacha. Thank

you for being with me at every step of this journey. Special mention goes to my colleagues, Dr. Olawale Fajemidupe and Dr. Rida Elgadaffi, who assisted me during this work.

Finally, to my wonderful family to whom this six years and PhD dissertation are dedicated to, I love you all, and I say thank you for your support in finishing this PhD program. To my wife, Mrs. Neha, thank you for supporting at every step and standing with my decisions. May God Almighty bless everyone mentioned herein and those not mentioned but have contributed in one way or another. I am grateful to all of you.

Thank you all.

Table of Contents

List of Tables

List of Figures

Abstract

The safety of well operations has become the focal point of the research paradigm since the Deepwater Horizon incident. The risks of wellbore blowouts cannot be neglected in any drilling operation, which makes the discharge of fluids a likely scenario. One of the critical observations while tackling the well control operation during the Deepwater Horizon incident was the fluid discharge rate with subsonic and sonic velocity. Lack of a comprehensive tool to estimate the worst-case discharge scenario constrained the tackling operations and exacerbated the side effects of blowouts. Keeping this in mind, an experimental and numerical investigation of multiphase flow was conducted, and consequently, an integrated reservoir and hydrodynamic model was developed to estimate the worst-case discharge (WCD).

A new multiphase vertical flow-loop was constructed, which included annulus and pipe as test sections. The flow loop was equipped with sensors and instruments to capture the flow characteristics. The experiments were conducted at high superficial gas (0-160m/s) and liquid velocity (0-2.35 m/s) to measure the pressure drop and liquid holdup. The high-speed video recording was implemented to capture the photographic images of flow dynamics. Experimental data were analyzed to understand the flow characteristics during high-velocity inlet conditions. Numerical investigations were carried out using computational fluid dynamics (CFD) and mechanistic modeling to mimic the experimental data.

The experimental results show the friction dominated trend of pressure gradients. The CFD modeling in ANSYS Fluent suggests that the volume of fluid multiphase flow model with different turbulence models can identify the flow regimes in high-velocity flow conditions. Furthermore, several mechanistic and empirical models were tested to verify the aptness in WCD

estimation. Finally, the suitable hydrodynamic model was incorporated in the newly developed tool to characterize the discharge rates. A new sonic correlation was developed based on which it can be established whether the sonic condition achieved in the well or not. These features were included in an integrated hydrodynamic and reservoir tool that can simulate the real-time event of WCD scenario. A sensitivity analysis was conducted to establish confidence in the software. The results were in good agreement with the commercial software in the base cases.

The novelty in this approach is the integrated use of numerical and experimental investigation to mimic the real field conditions of WCD especially for flow with Mach number greater than 0.3 (subsonic and sonic conditions). The new models and techniques can be used in flow characterization of high superficial gas velocity multiphase flow and estimation of flow rates during the worst case discharge.

Chapter 1: Introduction

1.1 Background

Over the past few years, huge efforts have been made towards oil and gas exploration and drilling in more challenging locations and harsher environments. These ultra-complex zones have led to greater uncertainties and necessitate robust well control strategies and techniques. The most critical events of well control include blowouts. Over the past decades, technology has been evolving and accompanied by several innovations and deeper understating to tackle these problems; however, the challenges have also been on a consistent upsurge. This upsurge is mainly attributed to increased activity in the completely new realm of hydrocarbon zones. If we look at the history of blowouts, it suggests that the small influx through the wellbore can be ultimately manifest into a blowout. There are several unexplored issues prevailing on this front as depicted in Figure 1.1.

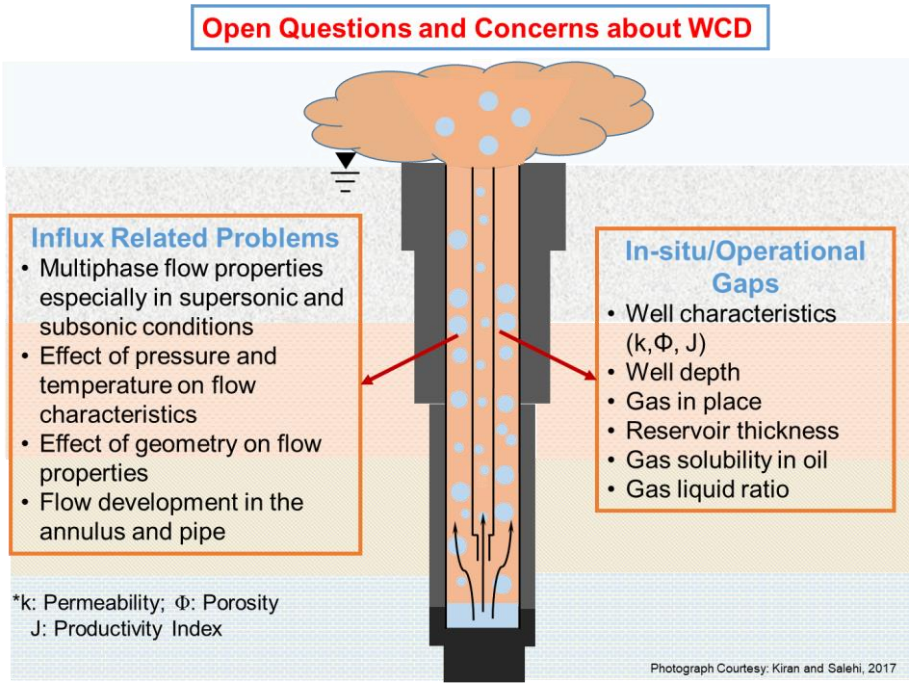

Figure 1.1 Open Questions on Fluid Dynamics Implications in Subsea Wells

Well control strategies are always planned before the execution of any drilling operation. During the blow out the gas and liquid travels in the wellbore section with enormous speed and eventually comes out of the wellbore. These phenomena are mainly studied in terms of worst-case discharge. In this post Macondo era, with the advent of highly advanced control systems, numerous studies had been conducted to develop reliable models to predict the discharge rate. These models include the hydrodynamic and reservoir flow models. However, there are several complications that still exists in these models. The gas can be soluble in fluid and solubility is affected by in-situ conditions. In addition to this, if the pressure in the wellbore reaches the bubble point, the free gas comes out of the liquid phase, and hence the phasic composition of the fluid starts changing. Apart from the complications with the fluid properties, the flow characteristics are quite complex considering the range of variation in in-situ conditions. These flow characteristics are quantified in terms of parameters such as flow rates, liquid holdup/void fraction, and flow patterns which subsequently impact the pressure gradients. The pressure gradients in-turn influences the flow rate of the fluid coming out of the domain under consideration. There are various outflow models available to predict flow rate, pressure drop, and liquid holdup. However, the validity of these models has never been verified for harsher in-situ conditions as pointed out by BSEE. Therefore, it is necessary to evaluate the performance of the existing models, determine their limitations in anticipating the conditions and develop suitable models for predictions.

1.2 Motivation and Research Hypotheses

In the past several decades, various studies had been conducted to understand the multiphase flow characteristics such as flow pattern, pressure profiles, and liquid holdup variation in the pipe and annulus. These models are combined with the reservoir models to characterize the discharge rate from the wellbore under unforeseen incidents such as blowouts. In the subsea wells, extreme high

temperature and high pressure can exist. The high pressure can result in the complete dissolution of the gaseous phase in the liquid phase under reservoir condition. However, as the fluid travels upward in the tubing/annulus, the pressure reduces significantly due to the reduction in hydrostatic head and pressure loss due to friction or acceleration component. Eventually, if the multiphase fluid reaches its bubble point pressure, the dissolved gas starts coming out which can increase the volumetric flow rate and consequently the superficial velocities of different phases. Many times, extremely high fluid velocity is achieved as the fluid approaches to the surface. In case of undesirable events, the flow might achieve sonic conditions at the surface while exit, which was the case expected in the Deepwater Horizon incident. Apart from the fluid flow in the wellbore, the bottom hole flowing pressure also creates strong coupling between inflow and outflow. As a result, a minor change in outflow condition can significantly impact the worst cased discharge (WCD) rate. Hence, the estimation of outflow condition is significant to the accuracy of WCD rate prediction. At present, different outflow models are available to predict flow pattern, pressure drop and liquid holdup. However, the validity of the models has never been verified for high Mach number flows especially in subsonic and sonic conditions. Therefore, it is necessary to evaluate the performance of the existing models for multiphase flow in pipe and annulus. The evaluation of these models requires experimental data for multiphase flow at such higher velocities. Hence, an extensive experimental study needs to be conducted to study the multiphase flow characteristics and determine the limitations of the models for high Mach number two-phase flows. These models further need to be integrated with the reservoir flow models to simulate the worst-case discharge conditions.

1.3 Research Objectives

The main objective of this study is to develop a user-friendly computational tool to imitate the worst-case discharge phenomenon under field conditions that might exist in the wellbores during extreme circumstances. The ideal tool can potentially integrate the reservoir (inflow) model and wellbore two-phase (outflow) flow models which are not available for the complex scenarios. In doing this, an evaluation of existing empirical, analytical, and mechanistic models to analyze the fluid flow in the wellbore is necessary. The experimental measurements and computational fluid dynamics (CFD) simulations for characterization of the velocities, pressure drop, flow patterns, and liquid holdup/void fraction will be highly desired for understanding the underlying mechanism.

Hence, a comprehensive effort has been made to simulate the high Mach number (Ma > 0.3) two-phase flow through the experimental and modeling studies. Several sets of experiment with different flow rates had been conducted and associated multiphase fluid flow parameters were obtained and analyzed. This data was eventually used to formulate a robust two-phase flow model which is the main objective of this study. The modeling studies were based on Computational Fluid Dynamics (CFD) techniques and mechanistic models. Results obtained from these techniques were combined to facilitate the upscaling of worst-case discharge (WCD) calculation based on actual field conditions of the Gulf of Mexico (GoM) wells. The specific project objectives are:

1. Develop a user-friendly computational tool to simulate the worst-case discharge based on different inflow/outflow models considering suitable operational conditions.
2. Validate the existing hydrodynamic models to simulate the wellbore fluid flow scenarios using the experimental data for different flow patterns.

3. Validate the proposed model and conduct the sensitivity analyses for operational parameters by considering various in-situ parameters.
4. Develop the CFD models for flow in the annulus and simulate the experimental data.
5. Verify the hydrodynamic models using the two-phase flow experimental data under high-velocity conditions.

Overall, this study takes the understanding of multiphase flow characteristics forward, and simultaneously develop a robust model to predict worst-case discharge suitable for simulation for loss of well control incidents.

1.4 Research Methods

The methodology adopted for this research included theoretical, experimental, and numerical investigation of the multiphase flow in the pipe and annulus. The overall research can be summarized in the following points:

1. **Theoretical Study:** A thorough literature review on the loss of well control incidents and multiphase flow characterization was performed. It included the study of past experimental reports for multiphase flow in pipe and annulus. The experimental data under investigation included flow characterization parameters such as pressure drop, liquid holdup/void fraction, and flow regimes. In addition, the review on the numerical part highlights the key objectives tied to multiphase flow theory and models. It also deals with the relevant past studies and theoretical aspects of computational fluid dynamics (CFD) modeling. An honest effort has been made to study the past work on subsonic and sonic multiphase flow characterization.

2. **Laboratory Experiments:** The main objective of the experimental work is to verify the hydrodynamic models used for the development of a worst-case discharge computational tool. This segment presents details of the experimental setup and results for multiphase flow experiment. It includes a description of the test setup to carry out experimental studies in vertical pipe and annulus. An extensive analysis of results and their interpretations are presented in this section. A comprehensive discussion on flow parameters such as pressure gradient, flow patterns, and liquid holdup at a relatively high Mach number of two-phase flows is presented, which is expected to influence the landscape of worst-case discharge (WCD) estimation.
3. **Computational Fluid Dynamics (CFD) Modeling:** This section is aimed to investigate and improve the understanding of two-phase flow characteristics in the annulus using computational fluid dynamics based on the available experimental data. Two flow patterns (churn and annular) were simulated. A comparative study was conducted to understand the relevance of different methods in high gas velocity scenarios in the annular/churn flow. Pressure gradient patterns and void fraction behavior were captured during the simulation. Probability density functions were implemented on time series evolution of void fraction to identify the flow regime for the CFD results.
4. **WCD Computational tool:** This part is comprised of a description of computational tool formulation, validation of hydrodynamic flow mechanistic models, and sensitivity analysis of the developed tool. A brief description of the nodal analysis is also presented. The focus of hydrodynamic models' investigation is limited to the annulus section. The flow in a pipe is beyond the scope of this work; however, a brief description is included. It presents the comparison of pressure gradient predictions for single and two-phase flow in a vertical

annulus with experimental data and other existing studies. In addition, a modified model for annular flow in the annulus is developed to improve the efficiency of the past mechanistic model.

1.5 Scope of Study

The scope of this study has been limited to the multiphase flow in the pipe and annulus section. The flow characterization for the pipe section is not presented in detail. However, an extensive investigation for flow in the annulus is conducted using the experimental and numerical approach. Various aspects of the worst-case discharge computational tool are presented; however, the focus is not on the reservoir aspect of the tool.

Chapter 2: Literature Review and Background Study

2.1 Past Incidents of Blowouts

The systemic risk for offshore drilling has become a new normal especially for deep-water wells where challenging in-situ conditions are complemented with the lack of technical understanding. A retrospective look at the past incidents reveals the fragility of complex technical systems (CSB report, 2016). Loss of well control incidents (LOWC) has existed in oil and gas operations since its inception. As per BSEE, LOWC is defined as the uncontrolled flow of formation or other fluids which may be to an exposed formation (underground blowout) or at the surface (surface blowout) or flow through a diverter or uncontrolled flow resulting from a failure of surface equipment or procedures. The LOWC incidents are categorized into blowouts (surface and underground), well release, and diverted well release. Typical categorization of blowouts is presented in **Table 2.1**.

Table 2.1 Blowouts Categorization

Category	Subcategory	Examples
Blowout (Surface flow)	• Uncontrolled flow from a deep zone • Uncontrolled flow from a shallow zone • Shallow gas "controlled" subsea release only	Uncontrolled incidents with surface/subsea flow Diverter system fails In riser-less drilling well starts to flow
Blowout (Underground flow)	• Underground flow only • Underground flow mainly, limited surface flow	Minor flow appears, and BOP is activated to shut the surface flow.

Some of the major catastrophic well control incidents leading to uncontrolled fluid discharge happening since the '80s. The first incident with fatalities reported in 1984 on the Zapata Lexington in the Gulf of Mexico to the recent Macondo incident on Deepwater Horizon are all examples of loss of well control incidents as depicted in Fig. 2.2 (Blake et al., 1988; CSB report, 2016).

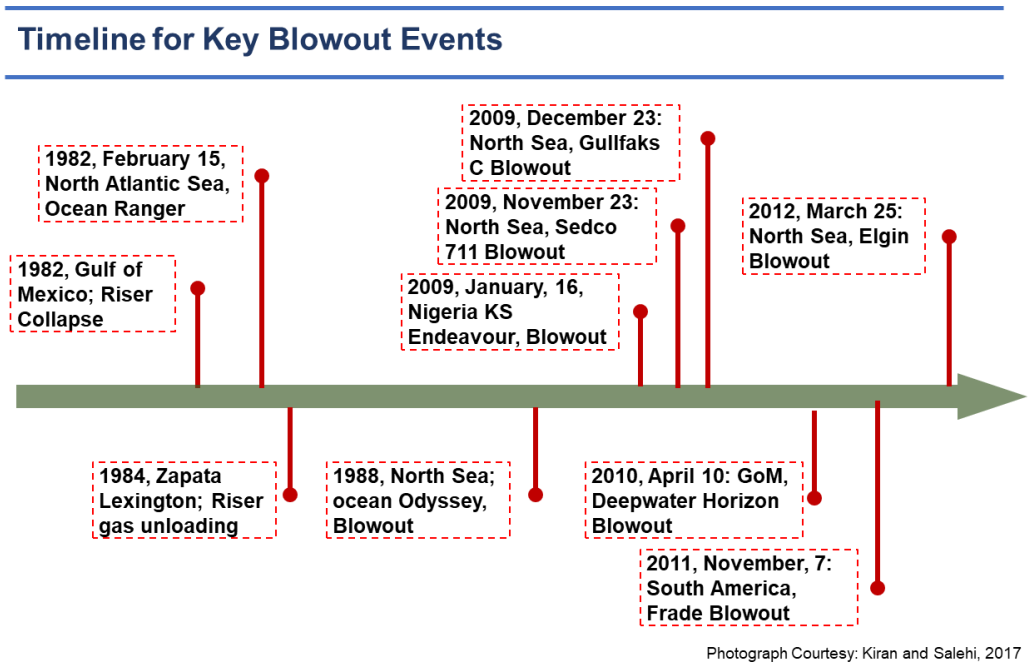

Figure 2.1 Key Blowout Events

Beside these blowouts, BSEE report (Per Holand, 2017) suggest that 58 blowout incidents occurred between 2000 to 2015, including the deep and shallow zone in the US Gulf of Mexico (GoM). In these blowouts, there were 12 fatalities. Apart from that, 74 worldwide fatalities reported in the period 2000-2015. Besides the fatalities, these blowouts led to severely impacted the nearby environments. Furthermore, there are huge financial consequences attached to such an incident. For instance, the deep-water horizon cost more than $60 billion which is ten times the Mars One's mission. Apart from that, huge oil spills also occur during such an incident. Some of the critical incidents and the resulting oil spills are presented below:

- Montara, Australia (2009): 29000 bbls
- Macondo, USA (2010): 4250000 bbls
- Frade, Brazil (2011): 3700 bbls

These incidents include external causes, loss of the well control barriers, and human errors. The well control integrity barriers are categorized into two independent barriers, usually referred to as

the primary and the secondary barrier envelopes. The primary barrier is normally the barrier closest to the potential source of the flow (a reservoir). For operations in a killed well, the hydrostatic pressure from the drilling mud is regarded as the primary barrier, and the blowout preventer (BOP), wellhead, drill pipe, the and casing is regarded as the secondary barrier envelope. In a production or injection well, the primary barrier envelope would typically be the packer that seals off the annulus, the tubing below the surface control subsurface safety valve (SCSSV), and the SCSSV. The secondary barrier envelope would then be the tubing above the SCSSV, the X-mas tree main flow side, the casing/wellhead, and the annulus side of the X-mas tree (Per Holand, 2017).

For a completion or workover operation, the barriers will change during the operation. For certain parts of the operation, the barriers will be based on the drilling barriers. For other parts of the operation, the barriers will be mechanical only, similar to the barriers that exist in the production phase. Strictly, when drilling the top-hole of the well before the BOP has been installed on the wellhead, there is a one-barrier situation. A mechanical device cannot close in the well. If the well started flowing in this situation, the well fluids would be diverted for a bottom fixed installation and released on the seafloor for a floating operation (Per Holand, 2017).

Typical secondary barrier failures are (US GoM exploration drilling since 1980 – 2015):

- BOP closes late for some reason causing limited release.
- BOP fails to close or fails after closure.
- Some dry BOPs lack blind shear ram and thereby cannot cut tubular and seal the well.
- Wellheads, where the BOP needs to nipple down to energize the casing seals after the casing has been cemented, have caused flow when BOP is not present.
- Jack-up type casing heads and casing spools with associated holding bolts and valves.
- Inadequate casing program, underground flow, and flow outside casing.

- Casing leaks due to not good enough casing design.

In case of drilling in shallow sections of well, there is only one well integrity barrier which is drilling fluid. The shallow zone loss of well control (LOWC) events are caused due to the low hydrostatic head leading to failure of the primary barrier. The shallow section is often drilled using sea water, and a slight presence of over-pressure zones lead to flow initiation. Another major factor in shallow zone LOWC incidents is related to flow after cementing. Immediately after the cement placement and prior to its setting, sometimes becomes self-supporting and loses its hydrostatic pressure. This situation leads to underbalanced conditions and eventually result in LOWC incidents. In addition, sometimes equipment failure also contributes to LOWC incidents. When shallow gas blowouts are contained, it may cause a tilt in bottom-supported platforms. Moreover, corrosion of diverter line due to the flow of gas and sand, diverter leak, leak of gas past the flowline seals, failure to close the diverter are major reported occurrences contributing to shallow zone LOWC.

2.1.1 Offshore Blowouts (Per Holand, 2017)

In the deep zone drilling, primarily the loss of well control (LOWC) incidents occurred during drilling activity in addition to the running casing and cement activity. In the US Gulf of Mexico (GoM) 13 of 24 LOWC were surface blowouts in the period from 2000 to 2015. While in rest of world, including Norway, UK, the Netherlands, Australia, Canada East Coast, US Pacific Offshore Continental Shelf (OCS), Denmark, and Brazil; 11 out of 12 LOWC events were surface blowouts. The main reasons in such blowouts were loss of primary barrier, loss of BOP, underbalanced conditions due to improper setting of cement, failure to close the Kelly valve, wellhead and casing head failure, unexpected high well pressure, casing plug failure, trapped gas release at rig floor,

failure to close the BOP, low marine riser package (LMRP) disconnect, and leak in annular preventer.

Other activities during which blowouts observed are workover, completion, production, and abandonment. During workover activities, 13 out of 33 LOWC events were attributed to surface blowouts in US GoM, UK and Norwegian waters, and rest of the world. Six of them happened due to low hydrostatic pressure while four of them occurred due to tubing leak and surface controlled subsurface safety valve (SCSSV) leak. Four out of 10 LOWC events occurred during the completion operation were surface blowouts. Out of them, two happened in US GoM and UK, which were attributed to too low mud weight. In US GoM, Walter Oil and Gas blowout on Hercules 265, the BOP was not closed against very high flow while in UK case the drill pipe pushed out of well, buckled, and split above the drill floor due to high well pressure. Despite activating the shear rams, the pipe was not sheared, and flow continues. During the production phase, primary and secondary barriers are mechanical barriers. The primary barrier which is closest to the reservoir comprised of packers that can seal off the annulus, SCSSV, and tubing below the SCSSV. The secondary barriers are the packers which seal off the tubing above the SCSSV, the casing/wellhead, the Xmas tree main flow side, and the annulus side of the Xmas tree. The main cause of these blowouts is due to normal causes and external loads such as ship collision, storm, and fire. There were 26 LOWC incidents reported during 2000-2015 worldwide in which 19 were surface blowouts. Four of the five incidents that occurred in the US GoM OCS were caused by damages from hurricanes. Other four in US GoM state waters, occurred due to ship collision. Apart from these seven blowouts were caused due to tubing leaks, casing leaks, multiple casing leaks, formation breakdown, and surface leak in the X-mas tree and then the failure of SCSSV. Three of the five reported incidents of LOWC in abandonments were considered as blowouts. In this, UK

Elgin blowout is well known which happened in 2012. Despite plugging of well for a year, the gas and condensate believed to originate from a rock formation located above the reservoir migrated. The corroded casing was fractured, and the flow was stopped after 53 days. Another blowout reported in offshore operation which was not categorized to any phase of the operation was Brazilian Platform P-7 in 2001.

For the period 2000–2015, 52% of the LOWC events come from the US GoM OCS. Further, 45% of the LOWC events occurred during drilling, 21% during workovers, and 17% during production (Per Holland, 2017).

2.1.2 Onshore Blowouts

Typically, before Macondo, the onshore blowouts are not usually not reported as it is due to lack of regulation. However, after this, the blowout incidents were reported strictly. Out of 336 LOWC incidents, 35 were blowouts as reported on the Texas Railroad Commission website. The details of these blowouts are presented in Appendix A.

2.2 Worst Case Discharge

The wellbore blowouts are always accompanied by the risks of discharge of drilling fluids and hydrocarbon. Massive blowout from a well is very difficult to manage. Lack of an integrated system to estimate the worst-case discharge scenario constrains the tackling operations and exacerbate the environmental side effects of oil and gas well blowouts. To cater with issues related to these well control scenarios, there are several guidelines established by federal and government bodies. One of the government body is the Bureau of Ocean Energy Management (BOEM). After the Macondo incident, BOEM established guidelines for worst-case discharge (WCD) calculation to improve wellbore safety (Moyer et al., 2012; Bowman, 2012). According to BOEM, the worst-

case discharge is defined as the daily rate of an uncontrolled flow from all producing reservoirs into the open wellbore. The fluid under consideration includes all hydrocarbon-bearing zones in each open-hole section as per the drilling plan. The unrestrained flow assumes pipe configuration with the unobstructed casing and liner and the hole without drill pipe. In addition, WCD rates are based on uncontrolled flow at the seafloor with a hydrostatic water head or atmospheric pressure at sea level with well work on an existing platform of deep-water wells.

The WCD estimate cannot be discarded because of its extremely low probability of occurrence as it can compromise the safety during drilling or completion stage of well construction. Current exploration in harsher paradigms of oil and gas reservoirs leads to drilling in overpressure zones. In case of insufficient drilling margin, the influx of formation fluid in the annulus at small scale can be encountered, which might manifest into uncontrolled flow considered as WCD. Over-pressurized formations are naturally occurring formations or created due to water or gas injections in nearby wells. The WCD rate significantly varies among wells based on reservoir inflow and wellbore outflow parameters and can be implemented in the risk assessment process. However, the risk assessment is highly dependent on the accuracy of WCD rate prediction. With greater accuracy, proper designing and holistic monitoring of the operation can be implemented to contain such scenarios. The core issue here is WCD rate predictions, and hence it is important to identify the parameters for WCD rate prediction. The main parameters for WCD rate prediction can be categorized into two parts, namely parameters for reservoir inflow and wellbore outflow. The inflow parameters comprise of reservoir characteristics such as permeability, porosity, pressure, and temperature, while the outflow parameters include parameters impacting the fluid flow in the wellbore such as depth, flow pattern, phase velocity, geometry. The permeability and porosity of a formation determine the fluid movement in the

formation as it is a governing factor for the formation influx rate. The change in pressure and temperature throughout the wellbore provides the necessary condition for the fluid to flow from the bottom to the top of the wellbore. The temperature affects the fluid properties and can exacerbate the flow issues (Oudeman and Kerem, 2006). The total depth of the well influences the change in the pressure gradient in the wellbore and consequently affect the discharge rate.

Besides the conventional inflow parameters, the time dependence of the formation characteristics depending on steady-state and transient reservoir models also influence the WCD rate. Steady state refers to the consistent formation characteristics independent of time, while the transient case depicts the dynamic characteristics. The transient case can effectively mimic the in-situ dynamic pressure and temperature and allows to define the control sequence for the occurrence within the on-site operational limitation. This dynamic rate is influenced by reservoir characteristics, pressure data, drive mechanisms, depletion rates, wellbore completion configurations, casing and production tubing sizes, production history, static and flowing bottom-hole pressures, wellbore flowing temperature, hydraulic roughness, and water intrusion (Replogle, 2009).

Apart from the reservoir side, the fluid dynamics in the wellbore is an important aspect of WCD rate prediction. The fluid flow in the wellbore is generally multiphase flow, and hence it is crucial to understand the underlying mechanism and physics of multiphase flow system in the wellbore. The efforts on this aspect have been made quite significantly over time by conducting experiments and developing the representative models. The modeling effort started with empirical correlations and shifted towards numerical modeling and simulation approach with the advancement in technology and computational powers. The empirical correlations consisted of statistical interpretation of the experimental results while the numerical approach is based on the

understanding of the dynamics and phenomena involved and consequently frame the governing equations with the imposed boundary conditions.

The fundamental aspect of every multiphase model depends on flow patterns or flow structures. However, several flow structures can exist in the flow domain based on in-situ conditions. Hence, it becomes very difficult to find a single model suitable for its characterization. In addition, there are several confusions, and disagreements also exist within the research community. Various models have been developed to address and improve the understanding of the phenomenon or process, but each inherently has limitations. There are consistent disagreements among the two schools of thought, empiricists and theoreticians. The empiricists claim that the data-based models have a better practical value because of the infinite complexity of the underlying phenomena and provides reasonable predictions. The theoreticians stress the (theoretically) better cognitive and predictive potential of mechanistic models, as the empirical models do not cover the wide range of field conditions. The empirical models are formulated by establishing a mathematical relationship based on experimental data. The theoretical models, however, are based on physics of flow dynamics and includes conservation of mass, momentum, and energy during the flow and can be extended to field conditions.

Having these advancements, the WCD estimations are limited to the empirical correlations. The models implemented are based on more generic and simple lab experimental data, and not tested for the harsher conditions as specified by regulatory bodies in post Macondo era. One of the main criteria which is not tested is flowing at high Mach number. Mach number, a dimensionless quantity is given as the ratio of flow velocity to the local speed of the sound. The speed having Mach number 1 represents the speed of sound. With Mach number 0.65 is about 65% of the speed of sound represents the subsonic condition, and Mach number 1.35 is about 35% faster than the

speed of sound represents supersonic conditions. The existing models used for pressure gradient calculation in WCD models are two-phase flow models, developed for low Mach number (Ma) flows (i.e., Ma < 0.1). To meet the requirements of the regulatory bodies, these models need to be tested and improved for high Mach number flow and other existing factors.

There are several fluid flow models used in the industry to estimate the WCD rate combined during nodal analysis. These models include the reservoir models for inflow characteristics and fluid dynamics model for outflow, which incorporate the factors as mentioned above. The details of the nodal analysis are described in the next section which includes the inflow models. In addition to nodal analysis, several other complementary models such as empirical, analytical, mechanistic, and numerical can be used in outflow and is discussed in section 2.4. Apart from the modeling aspect, experimental work is required to verify and validate the models. An extensive review of past experimental studies is discussed in Section 2.5.

2.3 Nodal Analysis

As mentioned in Section 2.2, the worst-case discharge (WCD) estimation requires two types of models: (a) inflow models and (b) outflow models. The inflow model represents the fluid influx into the well from the reservoir. It should be noted that the inflow models are beyond the scope of this study; hence, a brief description is only provided in the nodal analysis.

Nodal analysis is based on the construction of inflow performance relationship (IPR), which is developed using the flowing bottom-hole pressure (BHP) and liquid production rate. The inception of nodal analysis came with work conducted by Gilbert (1954) when two-phase flow and well capabilities were analyzed by matching the inflow performance and outflow performance. The same approach was named nodal analysis by Brown and Lea (1985). Afterward, this technique has been evolved over time to monitor the optimum production from oil and gas wells. Every

component in the production systems, static reservoir pressure and including inflow performance, as well as flow across the completion packer, up to the tubing string, across the surface choke, through horizontal flow lines, and into the separation facilities and many others, can be determined to have an economical production. The well components of this system have a broad impact on the nodal analysis.

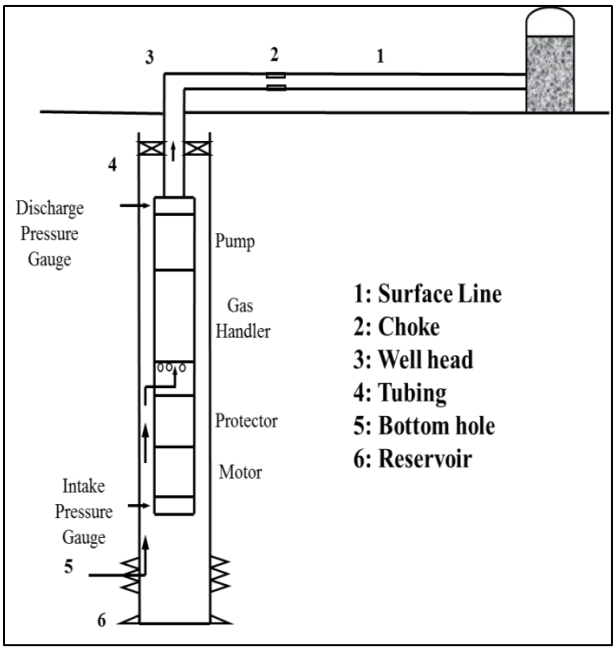

Figure 2.2 Flow across the Operation system

Figure 2.2 shows a schematic of a simple production system with nodal analysis architecture. The production system can be categorized into five system components: (a) reservoir, (b) bottom hole, (c) wellbore/tubing, (d) wellhead, (e) chole, and (f) surface line. Each system component affects production rate and pressure loss in different ways. The existing pressure gradient between reservoir and surface facility is the main driving force in oil and gas well. To characterize the pressure and flow rate profile in the system, it is divided into several nodes based on the system components. These nodes are iteratively solved for governing equations. The governing equations are framed in two ways which are eventually matched to get the desired profile. First, the bottom

hole pressure (BHP) is calculated using inflow performance relationship (IPR), and secondly, the outflow performance relationship (generally known as tubing performance relationship, TPR) are obtained for specific production rate. Several correlations exist to determine the inflow performance relationship based on Darcy and non-Darcy criteria (Guo et al., 2007).

Vogel (1968) came up with the equation to calculate BHP and flow rate for pressure below the bubble point. Bubble point refers to a pressure below which the free gas starts leaving the liquid phase from the crude oil. Vogel equation is represented by:

$$q = q_{\max}\left[1 - 0.2\left(\frac{p_{wf}}{\bar{p}}\right) - 0.8\left(\frac{p_{wf}}{\bar{p}}\right)^2\right] \tag{2.1}$$

where q_{max} is absolute open flow (theoretically estimated based on reservoir pressure and productivity index above bubble point pressure), p_{wf} is the bottom hole pressure, and $\bar{p}$ is the average pressure. For the pseudo-steady state (transient conditions), the absolute open flow is given by:

$$q_{\max} = \frac{J * \bar{p}}{1.8} \tag{2.2}$$

where J is the productivity index. Another well-known IPR equation is given by Fetkovich (1973) and considered to be more accurate which has been tested for reservoir permeability range of 6 mD to 1000 mD. It can be represented as follows:

$$q = q_{\max}\left[1 - \left(\frac{p_{wf}}{\bar{p}}\right)^2\right]^n \tag{2.3}$$

Brown and Lea (1985) used the non-Darcy flow and turbulence characteristics and presented a second order polynomial equation for the flow rate to calculate the pressure difference between reservoir pressure and bottom hole pressure. Standing incorporated the depletion effect in Vogel's

equation by introducing the zero-drawdown concept. The standing correlation incorporates the productivity index when bottom-hole pressure (BHP) tends to reservoir pressure. It also uses average pressure, $\bar{p}$ which is dependent on relative permeability of oil, the viscosity of othe il, and formation volume factor. The equation represents the single-phase flow. Hence, it can be valid for flow at the bottom of the well. However, other part of the wellbore can be under multiphase flow conditions. Some free gas is produced along with the liquid and it complicates the pressure loss calculation. As the pressure changes, the phase change takes place, and consequently, there is a change in density, velocity, the volume of each phase, and fluid property. Besides this, the pressure change is also accompanied with the change in temperature, which also affects the fluid flow. The primary equations characterizing the fluid flow is based on the general energy equation. The differential form of the energy equation is given below:

$$dU + d\left(\frac{P}{\rho}\right) + \frac{vdv}{g_c} + \frac{g}{g_c}dZ + dq + dW = 0 \tag{2.4}$$

Where U is total energy, P is the pressure, ρ is density, v is velocity, g is gravity, Z is compressibility, q is the heat change, and W is the work done on the system. Applying the first law of thermodynamics, Equation 2.4 becomes:

$$\frac{dP}{dL} = \frac{\rho v dv}{g_c dL} + \frac{\rho g}{g_c} + \left(\frac{dP}{dL}\right)_f \tag{2.5}$$

Equation 2.5 is applicable for vertical pipes and annuli. The equation consists of three components, acceleration, gravity, and friction pressure loss. The acceleration component is dependent on the kinetic energy of the system. The last term, $\left(\frac{dP}{dL}\right)_f$ represents the pressure loss due to friction, which can be calculated using existing multiphase models. In order to determine the two-phase friction factor accurately, the effects of the liquid holdup, density, velocity, viscosity, and surface

tension need to be investigated. The two-phase friction factor is more complicated due to the presence of different flow structures. The two-phase flow pattern is dependent on the superficial gas and liquid velocity. The details of the multiphase flow are described in the next section.

2.4 Multiphase flow

Multiphase flow exists in several industrial systems such as chemical reactors, power plants, heat exchangers, biological systems, nuclear reactors, and transport systems, apart from the petroleum industry. The underlying flow phenomenon exhibits different characteristics in each system. Hence, various correlations and models have been developed for the analysis of the system due to lack of the generalization. Apparently, because of the lack of generalization, the dynamics of multiphase flow has evolved slowly over time. The design of the engineering system is also limited to available experimental data and fitting conceptual mathematical models depicting the accuracy of physical processes. To understand and replicate the real-time scenarios, various characteristics and physics of multiphase flow are required.

For single-phase flow, the continuum concept is used, and the governing laws of physics are applied. To obtain the solution, the governing equations are combined with other models such as the thermodynamic equilibrium equations, constitute equations and heat transfer models. The continuum concept is difficult to apply for multiphase flow. The complexity of multiphase flow originates from the existence of multiple interfaces and non-homogeneous material discontinuities (Ishii and Hibiki, 2010).

As the petroleum industry deals with the flow of hydrocarbons regularly, the study of multiphase flow is imminent. One of the critical elements of the petroleum industry is the wellbore construction. The wellbore construction requires drilling. During this process, the two-phase flow

of hydrocarbon (gas or liquid) and drilling fluid may exist in the wellbore. The phase composition changes due to change in the in-situ wellbore temperature and pressure with depth and time. The origins of this change are variations in density and miscibility. The term flow pattern is introduced to characterize these variations and associated phenomenon. Flow pattern helps in distinguishing the consistent change based on the relative magnitude of the forces involved. Several other terms such as liquid holdup, superficial gas velocity, slip velocity, and superficial liquid velocity is introduced to assist the understanding of the flow patterns and multiphase flow hydraulics. Before going into more details, it is essential to have a knowledge of these terminologies in the context of multiphase flow in the wellbore.

The liquid holdup is the in-situ volumetric fraction of the liquid phase in the wellbore. The void fraction, which is the gas holdup, is also used in two-phase flow analysis. It represents the volume fraction occupied by the gas at the in-situ condition. Due to the difference in viscosity and density, the two phases travel at different velocities, and the flow is slip flow. The no-slip liquid holdup is defined as a liquid holdup that would exist if the liquid and gas phases travel at the same speed at the in-situ condition. Another common term is the superficial velocity, which is an average velocity of each phase calculated based on flow rate and the total cross-sectional area of the flow. The mixture velocity is the main velocity of the two phases together. The in-situ speed is the actual velocity of a given phase when it flows with other phases simultaneously. Properties of the mixture are calculated for no-slip and slipcases. Mixture density and viscosity are determined by applying the weighted averaging technique.

Different flow patterns develop due to variation in the distribution of the phases in the flow. The flow pattern is generally affected by gas and liquid rates, wellbore geometry, and thermodynamic properties of the phases. In addition, the flow pattern varies with wellbore pressure and

temperature. Flow patterns in multiphase flow can be classified from different perspectives. One approach is based on the existence of interfaces and discontinuities at the interfaces. According to this concept, it can be classified as a gas-solid mixture, gas-liquid mixture, liquid-liquid mixture, and immiscible liquid mixture (Pai, 2013). Another approach is based on the continuity of the medium and can be categorized as continuous and discontinuous flows. In continuous flow, there is no interruption between the phases and both phase travels simultaneously. Discontinuous-flow is based on consideration of both phases as a discrete entity.

In this study, the scope of work is limited to the flow of gas and liquid in the vertical pipe and annulus. Hewitt and Hall-Taylor (1970) classified the gas-liquid flow pattern of vertical upward flow based on the geometry of the interfaces. Hence, the flow pattern is described as bubbly flow, slug flow, churn flow, and annular flow. Similar flow patterns are also observed and reported in many other studies (Mcquillan and Whalley, 1985; Rozenblit et al., 2006; Taitel et al., 1980; Weisman et al., 1979). Figure 2.3 shows the most commonly used flow pattern classifications in vertical pipes.

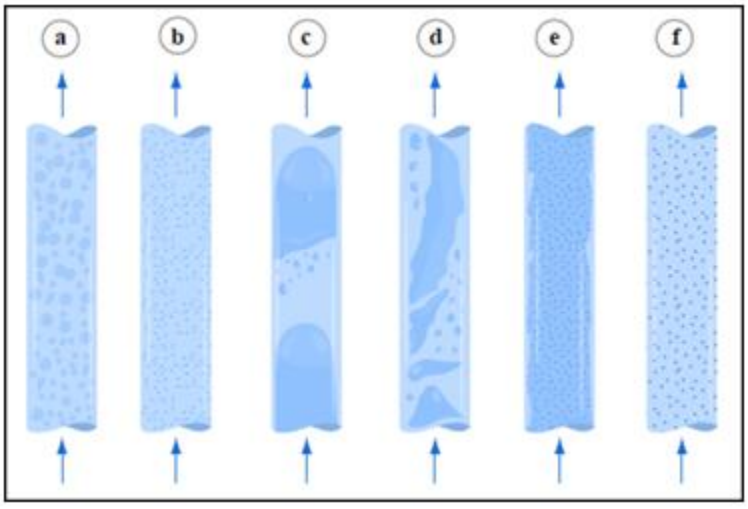

Figure 2.3 Typical flow pattern of in vertical pipeline: a) bubbly flow, b) dispersed bubbly, c) plug/slug flow, d) churn flow, e) annular flow, and f) mist flow (After Image by MIT-OCW)

Bubbly flows exist in vertical pipes at low gas flow rates. With increasing the gas flow rate, the bubbles coalesce and form larger bubbles. With further increase in gas flow rates, the coalesced bubbles grow and occupy the full pipe cross-section. The large bubbles (Taylor bubbles) split the liquid phase and form gas and liquid slugs. The liquid slugs regularly have small entrained-gas bubbles. A thin liquid film surrounds the gas slugs. This type of flow pattern is categorized as slug flow. Increasing gas flow rate further increases the shear stress between the Taylor bubble and the liquid film. The stress increase eventually ruptures the liquid film resulting in churning motion, which is often categorized as the churn flow pattern. At the extremely high gas rate, the gas phase flows as a plug occupying the central part of the pipe, and the pattern is recognized as annular flow. Depending on the flow condition, a limited number of liquid droplets can be entrained in the gas while the remaining part of the liquid flows as a film. In the vertical wellbore, different flow-patterns are expected to develop at various depths. For instance, near the bottom of the hole, a single-phase fluid is expected. As the fluid moves upward, the in-situ pressure gradually decreases causing the dissolved gas to liberate and form the bubbly flow pattern. As pressure decreases further, more gas may come out of the solution, and slug type flow-pattern develops.

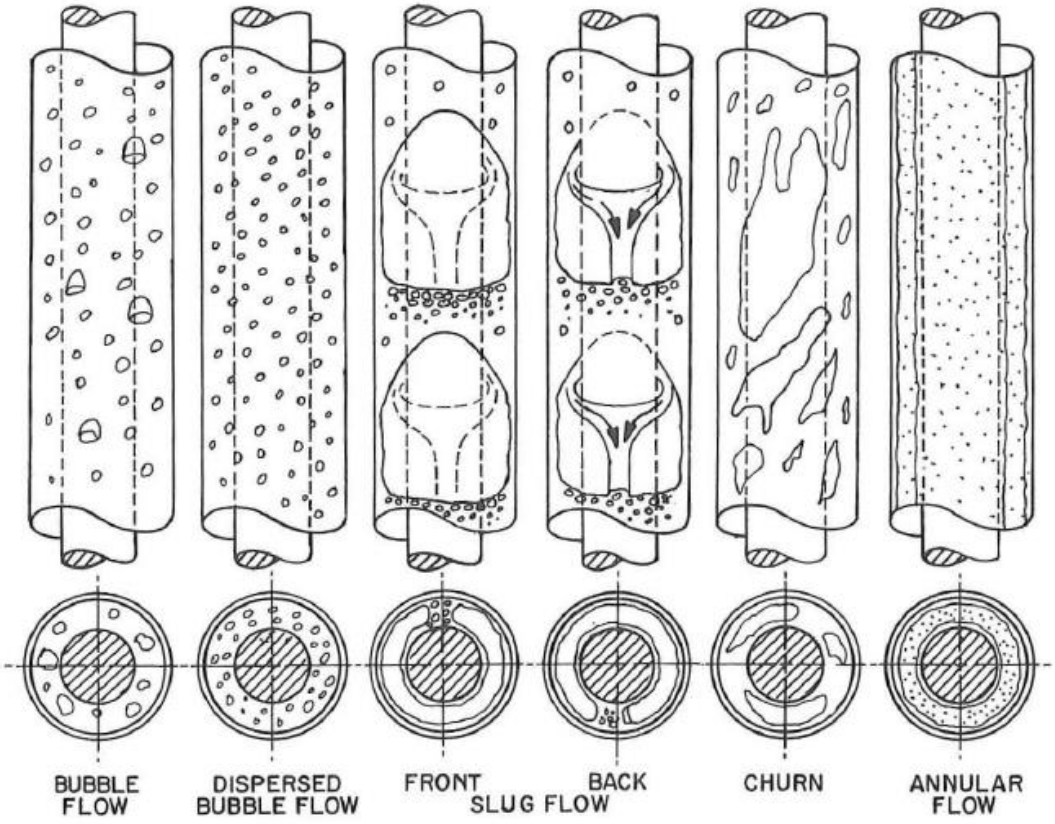

Figure 2.4 Flow Patterns in Annular Geometry (Caetano et al., 1992a)

Overall, the flow pattern maps in the annulus and pipe resemble each other. Caetano et al. (1992a) collected experimental data to establish flow pattern map for a vertical annulus and revealed that the flow pattern map is similar to a pipe; however, some differences exist (Figure 2.4). The flow patterns observed in annuli were mainly: bubbly, dispersed bubbly, slug, churn, and annular. In the bubbly flow, the gas phase is uniformly dispersed in the liquid phase as discrete bubbles. The bubbles have mainly two shapes: spherical and cap-type bubbles. The upward movement of spherical bubbles is random, while the cap-type bubbles move at a faster speed in a straight line. The dispersed bubble flow contains only small spherical discrete bubbles, moving upward in a straight path. The mixture velocity is the same as the liquid velocity with no slippage between the phases. Slug flow comprised of moving large bubbles, accompanied with liquid slugs at the tail. The large bubbles are termed as Taylor bubbles similar to the pipe flow. Liquid phase moves

backward in the form of films, which creates high turbulence behind the Taylor bubble. Churn flow is more chaotic and independent of geometry in comparison to the slug flow. With high gas concentration, the Taylor bubbles are destroyed, and the liquid falls backward. In the annular flow, continuous gas phase flow constitutes the core of the annulus. Liquid films form at the casing and tubing walls and move upward. Some liquid droplets are entrained in the gas core. The casing wall film is thicker than the tubing wall film. Overall, the Taylor bubbles in annular geometry are asymmetric, and liquid phase moves backward through a flow channel. The flow pattern is a function of tubing to casing diameter ratio (Caetano et al., 1992a).

It is essential to understand the features of various two-phase flow patterns. Flow pattern maps are developed as a means of characterizing two-phase flows. They can be used to predict transitional boundaries between two or more distinct flow patterns and other relevant flow parameters needed to perform the hydraulic analysis. The maps have consistent principles for the flow patterns, a broad database, and a semi-theoretical basis for determining flow pattern boundaries. Flow pattern maps are drawn in a two-dimensional graph, to split the map into regions of different flow patterns. Simple flow pattern maps employ identical coordinates for all flow patterns and transitions, while complex flow-pattern maps utilize different coordinates for flow transitions (Awad, 2010). Variety of flow pattern maps for vertical upward flow can be found in the literature. These are produced based on different coordinate systems such as modified superficial velocities (Hewitt and Roberts, 1969; Hewitt and Hall-Taylor, 1970), dimensionless parameters (Dun and Ros, 1963), and superficial velocities (Ansari et al., 1994). The coordinate parameters are based on flow conditions, gas-liquid physical properties, pipe material and diameter, and superficial velocities. A typical flow-pattern map for vertical pipes, which is based on the superficial velocity of liquid and gas, is presented in Figure 2.5 (Griffith, 1984).

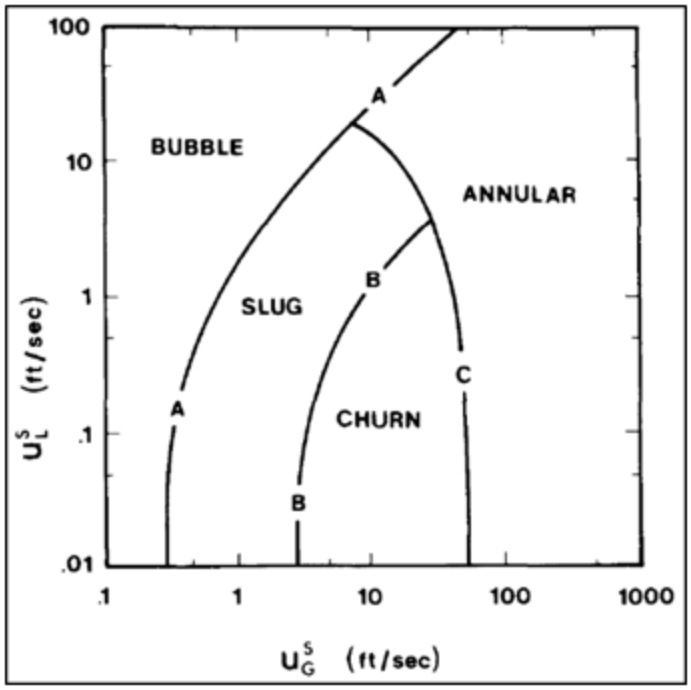

Figure 2.5 Flow pattern map for air and water in vertical up flow (Griffith, 1984)

Figure 2.6 shows different flow patterns existing in a pipe, based on dimensionless gas velocity number (RN) and liquid velocity number (N), which can be computed using Equations 2.6 and 2.7. Waltrich et al. (2015) conducted an experimental analysis and established the existence of annular flow in case of high superficial gas velocity where the ratio of gas and liquid velocity is greater than 100. The experimental data was superimposed on the flow pattern map developed by Duns and Ros (1963).

$$RN = V_{sg} \sqrt[4]{\frac{\rho_l}{g\sigma}} \tag{2.6}$$

$$N = V_{sl} \sqrt[4]{\frac{\rho_l}{g\sigma}} \tag{2.7}$$

where, V_{sg} denotes the superficial gas velocity, V_{sl} denotes the superficial liquid velocity, σ represents the surface tension, ρ_l represents the liquid density, and g stands for acceleration due to gravity. Black solid lines in the figure represent the flow regime based on Dun and Ros (1963)

model. The dashed line indicates the transition model based on Waltrich et al. (2015) study. Green, red and blue shaded regions are bubbly, churn, and annular flow regime, respectively.

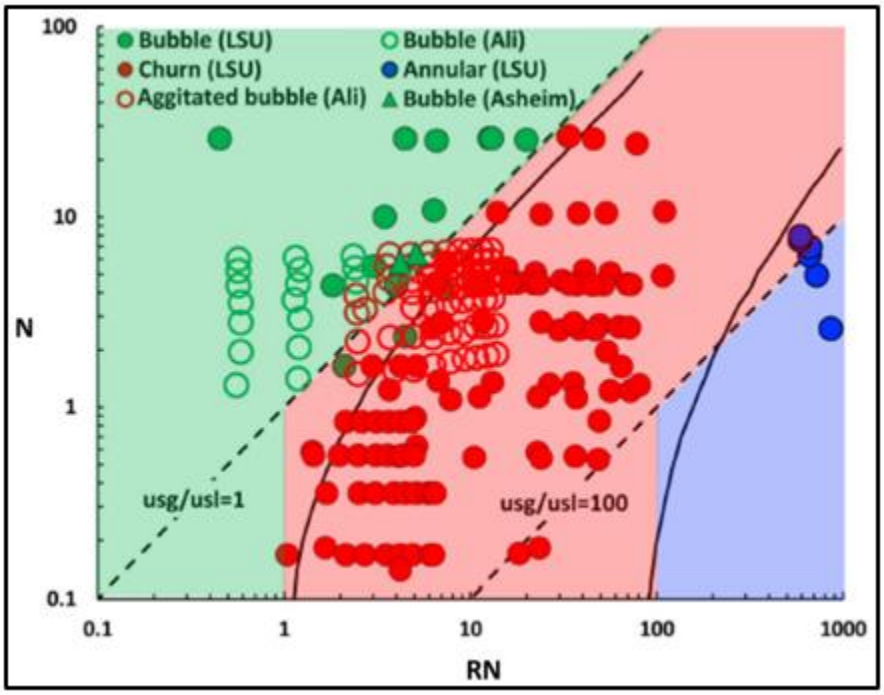

Figure 2.6 Experimental flow regime map (After Waltrich et al., 2015)

Even though flow patterns in the annulus and pipe are similar, there are some differences. Caetano et al. (1992a) proposed different flow pattern maps for air-water and air-kerosene flow through a concentric annulus (Figures 2.7 and 2.8). Air-kerosene mixture had lower flow transition superficial gas velocities, which is attributed to the change in the fluid properties. Hence, the impact of fluid properties on the transition from one flow pattern to another is important. To characterize these transitions, models have been proposed based on the flow characteristics. Mathematically, the bubble flow regime occurs in case of high Taylor velocity in comparison with discrete bubble velocity as described in Equation 2.8.

$$0.345\sqrt{gD_{EP}} \geq 1.53\left[\frac{(\rho_l - \rho_g)g\sigma}{\rho_l^{\,2}}\right]^{0.25} \tag{2.8}$$

where D_{EP} represents equi-periphery diameter (sum of tubing and casing diameter), g is acceleration due to gravity, ρ_l is liquid density, ρ_g is the gas density, σ denotes surface tension of the liquid in the presence of air. The bubble to slug transition is dictated by the agglomeration mechanism at low superficial velocity. During the test, the gas void fraction was 0.20. The in-situ liquid and gas superficial velocities are related by Equation 2.9 (Caetano et al., 1992a).

$$V_{sg} = \frac{V_{sl}}{4} + 0.306\left[\frac{(\rho_l - \rho_g)g\sigma}{\rho_l{}^2}\right]^{0.25} \tag{2.9}$$

where V_{sg} represents superficial gas velocity, V_{sl} represents superficial liquid velocity, g is acceleration due to gravity, ρ_l is liquid density, ρ_g is the gas density, σ is surface tension of the liquid in the presence of air.

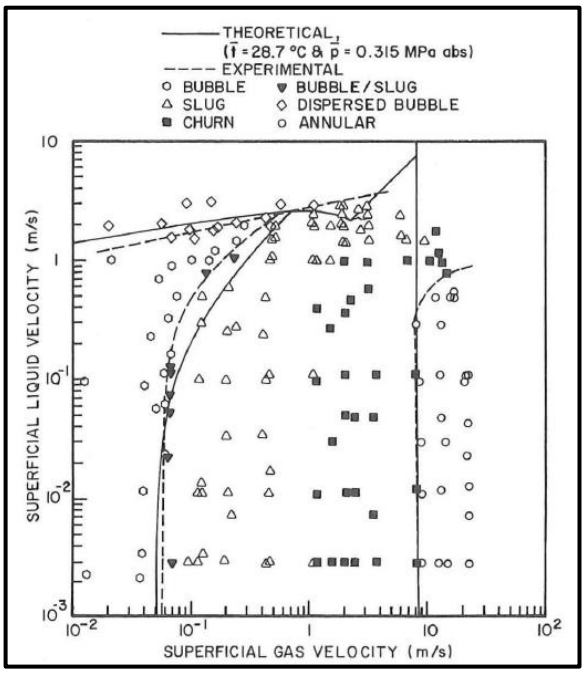

Figure 2.7 Flow pattern map for air-water mixture in concentric annulus (Caetano et al., 1992a)

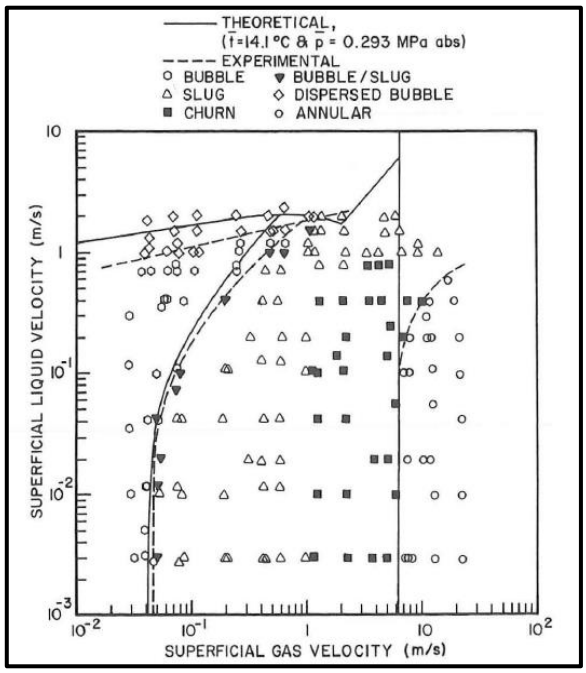

Figure 2.8 Flow pattern map for air-kerosene in concentric annulus (Caetano et al., 1992a)

The transition from bubble to slug is also modeled using the concept of hydraulic diameter in which high turbulent forces break the gas phase into the dispersed bubbles. The transition is defined by the following relation:

$$2\left[\frac{0.4\sigma}{(\rho_l-\rho_g)g}\right]^{0.5}\left(\frac{\rho_l}{\sigma}\right)^{0.6}\left(\frac{2}{D_H}\right)^{0.4}(f)^{0.4}(V_m)^{1.2}=0.725+4.15\left(\frac{V_{sg}}{V_m}\right)^{0.5} \quad (2.10)$$

where V_{sg} represents superficial gas velocity, V_m represents mixture superficial velocity, g is acceleration due to gravity, ρ_l is liquid density, ρ_g is the gas density, σ is surface tension of the liquid in the presence of air, D_H is a hydraulic diameter, and f is fanning friction factor.

The establishment of annular flow is dependent on the minimum gas velocity to move the largest liquid droplet entrained in the gas core and can be determined by comparing the gravity and drag forces. Equation 2.11 gives the transition condition after neglecting the effect of film thickness at the wall.

$$V_{sg}\geq 3.1\left[\frac{(\rho_l-\rho_g)g\sigma}{\rho_l^{\,2}}\right]^{0.25} \quad (2.11)$$

where V_{sg} represents superficial gas velocity, g is acceleration due to gravity, ρ_l is liquid density, ρ_g is the gas density, σ is surface tension of the liquid in the presence of air.

Besides the regular flow, the critical flow conditions might present in the worst case discharge. The critical flow of a single-phase gas occurs, when the Mach number is equal to 1 at the smallest cross-section or chokes (Wallis, 1980). For a single-phase flow, the sonic velocity can be determined based on the isentropic and equilibrium assumptions (Hsu, 1972). Several studies were conducted on supersonic two-phase flows. For two-phase flow, due to the existence of interfacial transports of mass, heat, and momentum, the isentropic and equilibrium assumptions will be no longer valid, and the dominant flow pattern plays a crucial role in flow characterization (Brown et

al., 1960; Baxendell and Thomas, 1961). In these critical flow conditions, the subsonic and supersonic flow conditions occur. These conditions are represented by different Mach numbers. The subsonic condition refers to the Mach number 0.3 to 1. The supersonic condition is represented by the Mach number above 1. The supersonic phenomenon is accompanied by shock generation in the system.

The supersonic shock phenomena in the two-phase tunnel were investigated by Eddington (1970). It was observed that the propagation velocity of a shock wave in a two-phase continuum corresponds to the velocity obtained by considering the two-phase medium as an isothermal continuum for the propagation of pressure waves. These waves exhibit finite structure, which depends on volume ratio, phase distribution, and wave strength of both phases. Later, Hsu (1972) extensively investigated the critical flow rate and sonic velocity in two-phase flow. The study investigated the flow pattern and slip ratio. A semi-empirical model was developed and validated using experimental measurements. Then, a theoretical model (Wallis, 1980) has been developed applying two-phase flow theories and conservation equations. Due to simplifying assumptions, theoretical models also require calibration to fit the experimental data. Furthermore, accurate critical flow models need to account for non-equilibrium (transient flow) phenomena. A model to predict sonic velocity in the one-dimensional stratified, slug, and homogeneous two-phase flow in a vertical pipe was presented by Nguyen et al. (1981). This model is based on the theory of pressure propagation without phase transformation. According to the modern, the interface of one phase acts as an elastic wall of the other phase. The critical limitation of this model was neglecting frictional forces and surface tensions.

The treatment of multiphase flow at lower velocity is explained in detail in this section, but the dynamics of flow in critical conditions (subsonic and supersonic) are different. A brief outline of

the supersonic/subsonic flow is provided in this section. However, Section 2.7 is fully dedicated to high-velocity multiphase flow.

2.5 Mathematical Models

There are different modeling approaches (empirical, analytical, mechanistic, and numerical) adopted in the industry for prediction of pressure drop, volumetric liquid holdup, and flow pattern of two-phase flow in pipes and annuli. The review of these models is presented in the sub-sections below.

2.5.1 Empirical Models

The most simplistic approach for two-phase flow characterization is based on experimental data. It can be formulated by establishing the mathematical correlations based on statistical evaluation of experimental results. However, the use of empirical models is limited to the range of data which is used to create the model. Though, this technique yields reasonably accurate prediction of two-phase flow parameters such as frictional pressure loss and volumetric liquid holdup. Although the empirical correlations require knowledge of system characteristics, there is difficulty in deciding on the accuracy of correlation in each flow pattern (Dukler et al., 1964). The pressure drop in multiphase flow in comparison to single-phase flow is different in several aspects. One of them is slippage arising between the phases. The slippage is the consequence of different velocity of different phase which in turn depends on the fluid properties. Based on these characteristics, empirical correlations can be divided into three categories, i) no-slip no-flow pattern (Poettman and Carpenter, 1952); ii) slip no-flow pattern (Eaton et al., 1967, Hagedorn and Brown, 1965; Zuber and Findlay, 1965); and iii) slip and flow pattern (Beggs and Brill, 1973; Hasan and Kabir, 1992; Mukherjee and Brill, 1985; Shi et al., 2005). Based on the geometry of the flow, some other

well-known correlations are as follows: Beggs-Brill Correlation (Beggs and Brill, 1973), Hagedorn-Brown Correlation (Hagedorn and Brown, 1965), Hasan-Kabir Correlation (Hasan and Kabir, 1992), Duns and Ros Correlation (Dun and Ros, 1963), and Orkiszewski Method (Orkizewski, 1967).

In this section, some of the empirical correlations of two-phase flow in the vertical wellbore are reviewed to get an understanding of the assumptions and conditions under which they were developed and their inherent limitations. The equations for pressure gradient calculations and flow pattern predictions are summarized in Appendix B.

Hagedorn & Brown Correlation (1965) was developed using data from 1500-ft vertical wellbore with tubing diameters ranging from 1-2 in. Five different fluid types, water and four types of oil with viscosities ranging from 10 to 110cp at 80°F are considered during the experimental investigation. The main contribution of this work was the development of correlation independent of flow patterns. Duns and Ros correlation was developed for the vertical flow of gas and liquid mixtures in wells. It is valid for a wide range of oil and gas mixtures and flow regimes. Although it was intended for use with 'dry' oil/gas mixtures, it can also be applicable to wet mixtures with a suitable correction. Orkiszewski correlation is limited to two-phase pressure drop in vertical wellbores and is an extension of Griffith and Wallis work. This correlation is valid for different flow regimes such as bubble, slug, transition, and annular mist. It is worth mentioning that the liquid holdup is evaluated using data from the Hagedorn and Brown model. Beggs & Brill correlation was developed from experimental data obtained in a small scale test facility. The range of parameters studied were included gas flow rate (0 to 300Mscf/D), liquid flow rate (0 to 30 gal/min), average system pressure (35 to 95 psia), pipe diameter (1 to 1.5 in.), liquid holdup (0 to 0.870), and pressure gradient (0 to 0.8psi/ft). Air and water were the fluids used in the experiment.

Dun and Ros, Orkiszewski, and Beggs and Brill considered flow regimes in vertical pipes by considering the slip conditions in vertical pipes. The flow regimes considered by them are bubble flow, slug flow, transition flow, and mist flow. In bubble flow the pipe is filled with liquid and free gas is present in small bubbles. The bubbles move at a different velocity and have little effect on the pressure gradient. Pipe wall is mainly in contact with the liquid phase. In slug flow, the gas phase is more distinct. The liquid phase is continuous, but the gas bubbles form plug or slug across the pipe section. Gas velocity is more than liquid, and liquid film around bubble moves downward with relatively low velocity. In this gas and liquid velocity, both have a noticeable effect on the pressure gradient. In transition flow, gas bubbles become more significant, and liquid entrains between the gas bubbles. The gas phase has a more dominant effect than a liquid phase in this case. Mist flow has a continuous gas phase, and liquid droplets are formed in the gas. All the correlations used Duns and Ros method for flow in the mist region. Dun and Ross observed the effect of wall roughness by viscosity and liquid film along the wall which causes a drag on gas and quantified by incorporating a non-dimensional number in Weber number. The summary of some of the correlation evolved is depicted in Table 2.2.

Table 2.2 Summary of empirical correlations

Authors	Flow Patterns addressed	Validation	Remark
Poettmann and Carpenter (1952)	No flow patterns considered	Flow rate > 420 STB/day; GLR < 1500 scf/STB; 2-3 in. pipe; Oil, water and air	Used solubility concepts
Duns and Ros (1963)	Bubble, slug, transition, annular-mist	3.5 in tubing; Oil and gas	3-10% deviation from the measure data
Hagedorn and Brown (1965)	No flow patterns considered	1500 ft experimental well data; 1, 1.25, 1.5 in tubing; Oil (10-110 cp) and gas	Correlation for friction factors and liquid holdup developed based on Reynolds number
Orkiszewski (1966)	Bubble, slug, transition, annular mist	1-3 in pipe size; Oil, water, and air	Griffith Wallis work extended to high-velocity, Annular-mist flow pattern not evaluated, Flow in casing annulus not evaluated
Bregg and Brills (1973)	Mist, bubble, slug, plug, annular, wavy, stratified	90 ft long pipe Gas flow rate (0-300 Mscf/D) Liquid flow rate (0-30 gal/min) System pressure (35-95 psia) Liquid holdup (0-0.87) Pressure gradient (0-0.8 psi/ft)	Correlation for inclination angle correction, Froude number, liquid content, and no slip holdup Correlation for predicting two-phase friction factor normalized with no slip friction factor from Moody diagram

*GLR: Gas Liquid ratio

2.5.2 Analytical Models

As we know the multiphase flow can be characterized using the conservation laws for mass, momentum, and energy. The analytical equations are derived using these conservation principles with certain assumptions and simplifications. These models quite successfully handle wide ranges of flow parameters with certain limitation in their accuracy due to modeling constraints and simplifications considered. Different analytical modeling approaches (Homogenous Model, Separated Flow Model, Interfacial Pressure Gradient (IPG) Model, Two-Fluid Model, and Drift

Flux Model) have been developed and used for designing and optimization purposes in the petroleum industry. In this section different analytical models are reviewed.

One of the simplistic models is the homogeneous model, also known as the no-slip model (Darcy, 1857). The main constraint of this model is due to no-slip condition (ratio of phase velocity) and model independent of flow pattern. This approach is generally not used in practice, except with single-phase simulators to provide a quick approximation of multiphase flow effects. This approach may also be used to benchmark the improvements gained from considering slip effects of more refined multiphase models. This model considers the two-phase flow as a single-phase flow having average fluid properties depending on phase composition.

Another model is the separated flow model which was introduced by Lockhart and Martinelli (Lockhart and Martinelli 1949) and later improved by Martinelli and Nelson (Martinelli and Nelson 1948). In this model, liquid and gas phases are considered individually and hence the name. It accounts for slippage between phases. The Lockhart-Martinelli procedure is one of the simplest methods for calculating two-phase flow pressure drop and liquid hold up (Awad, 2012). The merit of the Lockhart-Martinelli method is that it can be used for all flow patterns. The model is well applied in the power plant industry. It contains only one parameter to differ for the two phases, while in two-phase modeling approaches, separate equations of continuity, momentum, and energy for each phase along with rate equations are solved simultaneously. Different formulations of separated flow models (Muzychka and Awad, 2010; Turner 1966) are presented in the literature. In continuation of the Lockhart-Martinelli scheme, the interfacial pressure gradient is used to characterize gas-liquid flows, and the model is named Interfacial Pressure Gradient model. This approach considers small and large Lockhart-Martinelli parameters (Xm and Ym) which represent single-phase gas and liquid flow, respectively. The two-phase frictional pressure gradient is

defined as a linear combination of three pressure gradients; single-phase liquid, single-phase gas, and interfacial pressure gradients. It can be formulated as one, two, or multiple-parameter method addressing the complexity of flow pattern.

Another model based on the separated flow model is the drift flux model. It is based on relative motion rather than on the motion of the individual phases as used in the separated flow model. This model has been widely applied in bubbly and slug flow analysis with acceptable accuracy. However, it shows poor predictions to annular flow, which has two characteristic velocities (liquid film and liquid drop velocities) in one phase. The merit of the drift flux model is the reduction in the total number of field and constitutive equations required in comparison with the two-fluid model. The drift-flux model is expressed in terms of four field equations: the mixture continuity, momentum, energy equations, and the gas continuity equation. In 1970, the drift flux model for two-phase void calculation in different patterns of boiling flow was utilized by Rouhani and Axelsson (1970). They validated the model based on a wide range of experimental data, and the reported error is negligible. A similar study was performed to analyze flow in vertical wells. The drift flux model was used for predicting the void fraction in tubing for bubbly flow. The model was validated based on a different source of experimental data, and the acceptable match was reported. Moreover, to improve the accuracy of the drift flux model, studies were conducted to develop correlations for predicting model parameters for vertical and inclined pipe flows. Accuracy of the drift flux model highly depends on flow pattern which considered the slug and churn flow for gas-oil flow in vertical and inclined wells (Hasan and Kabir 1992, Kabir and Hasan 1990).

The most advanced model in the area of analytical modeling is the two-fluid model, which is used as a predictive tool for two-phase flow characterization in engineering applications. The real

benefit of this model is that it accounts for the dynamic and non-equilibrium interactions existing between the phases. The model considers each phase as a distinct fluid and applies the governing equations. As a result, each phase has its own pressure, temperature, and velocity profiles. In this manner, the differences between the two phases can be accurately pinpointed. Also, this model has been well applied for analyzing two-phase flow in shell-sides of large heat exchangers with different gas and liquid velocity directions such as steam generators and kettle reboilers. However, the model is computationally very expensive in comparison to other analytical models (Schlegel et al., 2010). In addition, the use of two momentum equations presents considerable complications in modeling interfacial interaction between the two phases (Hibiki and Ishii (2003). Table 2.3 presents the summary of different well know analytical models developed for two-phase flow.

Table 2.3 Summary of analytical models

Authors	Model type	Validation	Remark
Kawanishi et al. (1990)	Drift Flux model	Steam-water/Air-water ID: 0.6-61 cm	Relative error was 0.168 Annular condition not studied in detail
Shi et al. (2003)	Steady-state Drift-Flux model	Oil, water, and Nitrogen gas 15.2 cm diameter and 10.9 m long test section	Optimized drift flux parameters to study large diameter, vertical and inclined pipes
Hibiki and Ishii (2003)	Steady-state Drift Flux model	Air-water adiabatic flow 2 in pipe diameter	Constitutive equation developed for bubble, slug, churn, and annular flow Model showed 70% deviation for velocity at 10 m/s
Schegel et al. (2010)	Drift Flux model	Test sections under 0.15 and 0.20 m Liquid velocity up to 1 m/s Void fractions up to 0.85	Review of drift-flux models for different diameter No effect on drift flux parameter for non-dimensional diameter above 30
Bhagwat and Ghajar (2014)	Drift-Flux model	Range of Parameters: Diameter: 0.5-305 mm Liquid Viscosity: 0.0001-0.6 Pa-s System pressure: 0.1-18.1 MPa	Correlation development: Distribution parameter and drift velocity as function of pipe diameter, pipe orientation, phase flow rate, fluid properties, and void fraction Void fraction independent of flow patterns

*ID: Inner diameter

Due to reasonable efficiency and accuracy, the drift-flux model is frequently used in the Petroleum industry. The same model can be used for the WCD study, considering the steady-state formulation. Drift-flux model (DFM) has been consistently used and improved in the Petroleum industry since its inception due to its simplicity, and continuous and differentiable behavior (Zuber and Findlay, 1965; Hasan and Kabir, 1988; Ansari et al., 1994). DFM relies on slip property

between gas and liquid, which is determined by two factors namely, gas concentration and the tendency of the gas to move upward due to buoyancy.

2.5.3 Mechanistic Model

The complex physical phenomena of multiphase flow cannot be addressed by the generalized empirical correlations and simplified analytical models. Mechanistic models have been introduced to predict flow behavior more accurately under different flow conditions. This class of models is based on a phenomenological approach that takes into account basic principles (conservation of mass, momentum, and energy). Continuity is preserved by applying simultaneous mass balances of the phases. The early mechanistic models (Orkiszewski 1967, Caetano et al., 1992 a and b) were developed to predict flow pattern transition and pressure drop during steady gas-liquid flow in vertical tubes. The models incorporate the effect of fluid properties and flow geometry. The models do not have severe limitations as the empirical models. Later, improved and more advanced mechanistic models (Ansari et al. 1994; Hasan and Kabir, 1988; Gomez et al. 2000) for two-phase gas-liquid flow were developed considering different flow patterns and geometries. To simulate real flow in oil and gas wells, the models are coupled with PVT models. Other applications of mechanistic models in analyzing two-phase flows have been widely reported in the literature (Gomez et al., 2000; Liu et al., 2005). The most important achievement of mechanistic models was that following flow regime determination, separate models for predicting the vertical wellbore hydraulic characteristics, such as pressure drop, liquid holdup, and temperature profile was also developed. Mechanistic models are practical in extensive conditions.

Various mechanistic and empirical models are reviewed to ascertain the assumptions under which they were developed and their inherent limitations. Bijleveld et al., (1988) developed the first

steady state mechanistic model where bottom-hole pressure and two-phase flow parameters were calculated by using a trial and error procedure. In this model, the stratified flow was assumed initially and then checked for its validity. In the case of non-existence of this flow pattern, another flow pattern is assumed, and the same procedure is repeated. An average absolute error of 10% was reported compared with an average absolute error of 12% shown by Beggs and Brill. In the continuation, several other mechanistic models evolved to characterize different flow parameters such as flow pattern, film thickness, rise velocity of gas bubbles in liquid columns, and liquid holdup. Ansari et al. (1994) developed a model for upward vertical two-phase flow in pipes. Gomez et al. (2000) also used a unified mechanistic approach for predicting the flow parameters.

Caetano et al. (1992b) developed a mechanistic model for upward vertical flow in the annulus geometry. The bubble to slug transition criteria is assumed to be the void fraction of 0.2; however, other studies (Hasan and Kabir, 1988; Kelessidis and Dukler, 1989; Lage and Time, 2000) proposed slightly different transition point (void fraction of 0.25). It should be worth noting that the slug geometry is assumed to be asymmetrical, which might not be the case for slug flow regime. Hasan and Kabir (1988) developed a model to predict two-phase upward flow in annuli for bubble, dispersed bubble, and slug flow regime. The model predicts the gas void fraction using the drift-flux approach considering liquid slugs and Taylor bubbles. Recently, an improved mechanistic model was developed (Lage and Time, 2000) to analyze two-phase upward flow in the concentric annulus. This model does not incorporate the liquid entrainment effect in the gas core. Similar models (Ansari et al. 1994) predict the flow variables and flow pattern transition (bubble flow, dispersed flow, slug flow, and annular flow) in the pipe as shown in Figure 2.3. The models developed by Ansari et al. (1994) is based on the fundamentals and governing equations proposed by Caetano et al. (1992b). The study conducted by Ansari et al. (1994) suggests the significant

improvement in annular flow model which is presented in Table 2.4. After determining the flow pattern, the flow variables are determined. The model was validated using a wide range of experimental data and field measurements.

Table 2.4 Statistical result of the comparative study of models for annular flow (After Ansari et al. 1994)

Model	Relative Performance Factor
Aziz et al. (1972)	5.9
Hagedorn and Brown	8.6
Duns and Ros	11.3
Mukherjee and Brill	17.4
Beggs and Brill	20.5
Orkiszewski	45.8
Ansari et al. (1994)	5

Table 2.5 summarizes different mechanistic models developed over time.

Table 2.5 Summary of mechanistic models

Authors	Flow Patterns addressed	Validation	Remark
Aziz et al. (1972)	Bubbly, slug, and froth	Field data: ID: 1.992-2.436 in Oil rate: 44-1850 bbl/d GOR: 143-9975 Scf/bbl API: 18.7-47.3	Model for flow in Pipe Error similar to Orkiszewski but superior to Hagedorn and Brown and Duns and Ros
Hasan and Kabir (1988)	Bubble, slug, and annular	Beggs and Brill data and Lau's data	Model for flow in pipe and annulus New correlation for flow parameters for bubbly flow Maximum error of 4.6%
Hasan and Kabir (1992)	Bubbly, slug, churn, and annular	Test data Maximum OD: 127 mm Maximum ID: 87 mm Maximum Vsg: 15.24 m/s	Model for flow in annulus Drift flux approach adapted to model slip
Caetano (1992 a and b)	Bubble, dispersed bubble, slug, and annular	Experimental data Air-water and Air-Kerosene 3 X 1.66 in test section	Model for flow in annulus Strong dependence on liquid entrainment Film thickness ratio dependent on adopted droplet deposition mechanism
Ansari et al. (1994)	Bubble, slug, and annular	Field data from different sources	Model for flow in pipe Used the concept of Caetano (1992 a and b) model for slug flow Better performance than other empirical correlations and Aziz et al. (1972) and Hasan and Kabir (1988) model
Gomez et al. (2000)	Stratified, slug, bubble, annular, and dispersed bubble	Lab data: Maximum ID: 3 in	Unified model for flow in Pipe Absolute average Error for databank: 12.6%

Lage and Time (2000)	Bubble, dispersed bubble, slug, and annular	Used Caetano (1985) data and another full-scale Experiment setup with 6.276 X 2.764 in test section	Model for flow in annulus Same film thickness to tubing and Casing wall Less than 10% absolute errors

Model evaluation (Caetano et al. 1992b) for all flow patterns except the annular flow demonstrated discrepancy of less than 5 percent between predictions and measurements. The annular flow model performance was strongly dependent on the liquid entrained fraction. In addition, the liquid film thickness ration is dependent on the scattering isotropy and independent of liquid droplet size. However, previous studies state that the rate of deposition is highly dependent on the liquid droplet size. A study conducted by Aggour et al. (1996) on the field data concluded that the Beggs and Brill correlation has an overall minimum relative error for tubing size as well total liquid rate in the pipe flow. However, at the higher flow rate more than 20,000 B/D, Hasan and Kabir's model exhibits better accuracy. The findings are presented in Figures 2.9 and 2.10.

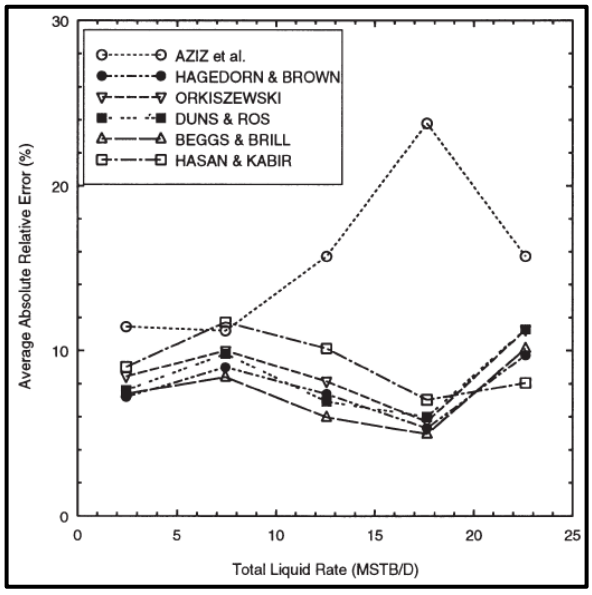

Figure 2.9 Effect of rate of liquid on the accuracy of different flow correlations (Aggour et al., 1996)

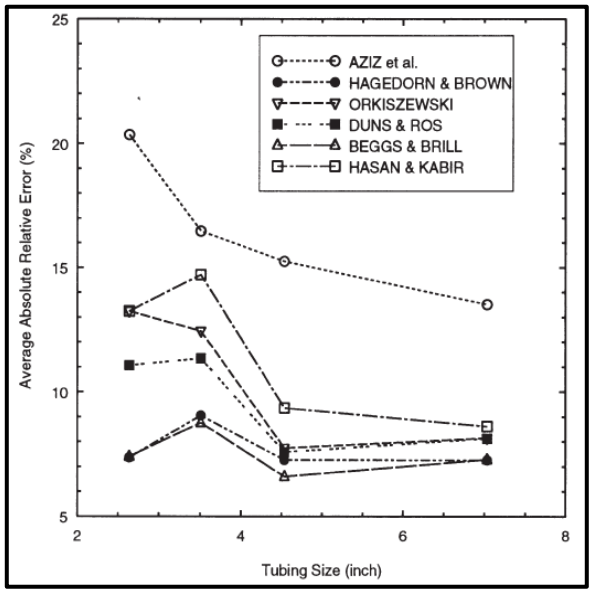

Figure 2.10 Effect of tubing size on the accuracy of different flow correlations (Aggour et al., 1996)

2.5.4 Computational Fluid Dynamics Modeling

2.5.4.1 Theoretical Background

The fluid dynamics of two-phase flow is very important in petroleum operations (Barati and Liang 2014; Torsvik et al., 2017; Kiran and Salehi 2018; and Hulsurkar et al., 2018). The movement of two distinct phases together complicates the flow characteristics (Shirdel and Sepehrnoori, 2017). Different modeling approaches (empirical, analytical, mechanistic, and numerical methods) have been developed for characterizing multiphase flows (Ibarra et al., 2017; Caetano et al., 1992b and Mukherjee and Brill, 1985). Though the numerical method is computationally intensive, it has a broader potential for characterization of the flow. In the numerical techniques, there are several approaches which have been developed in the past. For multiphase flow analysis, there are two types of approaches: Eulerian-Lagrangian and Eulerian-Eulerian. The Eulerian-Lagrangian models are applied for discrete phase modeling in which continuous phase treated as a continuum, and dispersed phase flow is solved by tracking many bubbles or droplets. The dispersed phase can

exchange momentum, mass, and energy with the continuous phase. This method is not suited for flows in which the volume fraction of the second phase is considerable (Fluent, 2016a). On the other hand, the Eulerian-Eulerian approach treats distinct phases as interpenetrating continua using the concept of phasic volume fraction. The idea of phasic volume fraction relies on the premise that the volume fractions are a continuous function in the spatial and temporal domain and the total sum of the volume fraction of all phases are unity. Conservation principles are applied for each phase and equations are closed by empirical correlations or use of the kinetic theory. The Eulerian-Eulerian approach has three modeling formulations: mixture model, the volume of fluid (VOF) model, and the Eulerian Model.

The mixture model considers the phases as interpenetrating continua and uses the momentum equation for the mixture and recommends relative velocity of the dispersed phase. The Eulerian model considers a more sophisticated approach. In this study, the VOF method is used due to its comparative simplicity and lesser computational effort. The VOF model is a surface tracking technique implemented for immiscible fluids in which the fluid interface is studied. In this method, a single momentum equation is used, and the volume fraction of each phase in each cell is tracked. The equations of motion are solved by applying the boundary conditions, and the volume fraction of each phase is tracked eventually. It can be applied for the steady or transient tracking of any gas-liquid interface, and the motion of large bubbles in the liquid. The governing equations used in this model are continuity and momentum equations. The continuity equation for the secondary phase is solved to characterize the development of an interface in the spatial and temporal domain. For the i^{th} phase, the continuity equation can be written as follows:

$$\frac{1}{\rho_i}\left[\frac{\partial}{\partial t}(\alpha_i\rho_i) + \nabla.(\alpha_i\rho_i\overrightarrow{v_i}) = S_{\alpha_i} + \sum_{i=1}^{n}\left(\dot{m}_{ij} - \dot{m}_{ji}\right)\right] \quad (2.12)$$

where ρ_i is the density of the i^{th} phase, α_i is the volume fraction of the i^{th} phase, $\dot{m}_{ij}$ refers to mass transfer from phase i to j and $\dot{m}_{ji}$ refers to mass transfer from phase j to i, and $S_{\alpha i}$ is the source term. The VOF model considers the general momentum equation for a solution which is depicted in Equation 2.13. The momentum equation is solved for shared velocity among phases which makes the model vulnerable to substantial velocity differences between the phases.

$$\frac{\partial(\rho\vec{v})}{\partial t} + \nabla.(\rho\vec{v}\vec{v}) = -\nabla p + \nabla.(\bar{\bar{\tau}}) + \rho\vec{g} + \vec{F} \tag{2.13}$$

where p is static pressure, $\vec{g}$ is the acceleration due to gravity, $\vec{F}$ is external body forces, $\bar{\bar{\tau}}$ is stress tensor which is given by Equation 2.14.

$$\bar{\bar{\tau}} = \mu\left[(\nabla\vec{v} + \nabla\vec{v}^T) - \frac{2}{3}\nabla.\vec{v}I\right] \tag{2.14}$$

where μ is the molecular viscosity, and I is unit tensor. After solving the volume fraction for the secondary phase, the volume fraction of primary phase is determined by the closure relation, which suggests that the sum of the volume fraction of each phase is unity. The material properties are calculated using mixture rule which can be represented by the following equation:

$$\rho = \sum \alpha_i \rho_i \tag{2.15}$$

The VOF model mainly relies on the momentum conservation of the fluid phases with their corresponding properties (Fluent, 2016a). The VOF model can be used in combination with different turbulence models suited to the need for the study. Considering various multiphase flow models offered in the ANSYS software package, the volume of fluid (VOF) model is one of the universally accepted approaches. The advantage of the VOF model is its gas-liquid interface tracking proficiencies. Besides, sharp interfaces between two phases (gas-liquid or solid-liquid) can be determined by using this technique. Hence, it has been widely employed to predict the flow pattern (fluid flow behavior) and perform a quantitative comparison.

Furthermore, turbulence structures evolve over time. Two of the widely used turbulent models are *k*-ε and *k*-ω models. *k* refers to the turbulent kinetic energy, ε stands for turbulent dissipation rate, and ω is the specific dissipation rate. There are several models for *k*-ε. In this study, the realizable model is implemented. The *k*-ε realizable model is based on two conservation equations as stated below:

$$\frac{\partial(\rho uk)}{\partial x}+\frac{\partial(\rho vk)}{\partial y}=\frac{\partial}{\partial x}\left(\mu+\frac{\mu_T}{\sigma_k}\right)\frac{\partial k}{\partial x}+\frac{\partial}{\partial y}\left(\mu+\frac{\mu_T}{\sigma_k}\right)\frac{\partial k}{\partial y}+\mu_T G-\rho\epsilon-2\mu\left(\frac{\partial k^{1/3}}{\partial y}\right)^2 \quad (2.16)$$

where turbulent kinetic energy and dissipation rates are combined in the governing equation by the relation of turbulent viscosity, μ_T. The dissipation rate of kinetic energy is given by:

$$\frac{\partial(\rho u\varepsilon)}{\partial x}+\frac{\partial(\rho v\varepsilon)}{\partial y}=\frac{\partial}{\partial x}\left(\mu+\frac{\mu_T}{\sigma_k}\right)\frac{\partial \varepsilon}{\partial x}+\frac{\partial}{\partial y}\left(\mu+\frac{\mu_T}{\sigma_k}\right)\frac{\partial \varepsilon}{\partial y}+\frac{\varepsilon}{k}C_1 f_1\mu_T G-\frac{\varepsilon^3}{k}C_2 f_2\mu_T\rho+\frac{2\mu\mu_T}{\rho}\left(\frac{\partial^2 u}{\partial y^2}\right)^2 \quad (2.17)$$

The turbulent viscosity is expressed as:

$$\mu_T=\frac{f_\mu C_\mu \rho k^2}{\varepsilon} \quad (2.18)$$

where model parameters are described as: $\mu_k=\mu_m+{\mu_t}/{\sigma_k}$, σ_k=1, σ_ε=1.3, Cμ=0.09, C_1=1.92, and C_2 = 1.3. The wall damping functions (f_1, f_2, and f_μ) are incorporated using the functions suggested by Lam and Bremhorst (1981). In addition, the realizable turbulence model imposes mathematical constraints on Reynolds stresses and follows the schwarz inequality which makes the *k*-ε turbulent model more robust for boundary layers under adverse pressure gradients and flow separation conditions.

$$\overline{U_i'U_j'}>0 \quad (2.19)$$

$$\left(\overline{U_i'U_j'}\right)^2\le\overline{U_i^2U_j^2} \quad (2.20)$$

where U_i' and U_j' are fluctuating velocities. Wilcox (1993) introduced the *k*-ω turbulence models to ease the limitations of the *k*-ε model (further details are presented in Sections 4.2.4). In the

shear stress transport (SST) k-ω turbulence model, ε equation is replaced by substituting ε for k-ω in the transport equation, whereas the conservation equation for k is considered the same. In addition, Menter et al. (2003) suggested improved model parameters and incorporated blending functions and limiters to enhance numerical stability. They also proposed a revised eddy viscosity correlation for k-ω turbulence model.

2.5.4.2 Related Studies

Numerous CFD simulation studies have been used to characterize the intricacies of multiphase flow especially in pipe geometry (Zabaras et al., 2013; Waltrich et al., 2015; Chen, 2004; Sanati, 2015). These studies included flow regime identification, pressure loss, and void fraction predictions using different multiphase flow simulation approaches.

Bubbly two-phase flow condition establishes at low superficial gas velocities (Figure 2.3). Taha and Cui (2006) used the Volume of Fluid (VOF) approach to investigate the propagation of Taylor bubbles in the stagnant and flowing fluid and compared the results with experimental data. The study suggested that bubble shape is dependent on liquid viscosity and surface tension, which affects the liquid film thickness around the bubble. In the case of high viscosity, wavelet around the bubble tail was also observed in the simulation results. A similar study was conducted by Ajauro et al. (2013) to characterize the rising bubble dynamics. Simulation results showed that the nose shape of trailing bubbles becomes more evident with an increase in Eotvos number. For bubbly two-phase flow in a pipe, Rzehak and Kriebitzsch (2016) compared the predictions of two CFD codes (ANSYS CFX and OpenFOAM) with published measurements (Liu et al. 1998; Lucas et al. 2005). The results showed high discrepancies in turbulent characteristics (turbulent kinetic energy and turbulent viscosity) in the near-wall region while a good agreement was observed in

the core region of the pipe. In addition, the OpenFOAM showed higher discrepancies in predicting gas void fraction in the vicinity of the pipe wall.

In two-phase flow, slug and churn flow regimes occur at the intermediate superficial gas velocities. Lun et al. (1996) carried out a sensitivity analysis on grid density for slug flow characterization and identified critical regions in which the gas-liquid interface is susceptible to the mesh density. Parvareh et al. (2010) used electrical resistance tomography (ERT) system to visualize the two-phase flow pattern in horizontal and vertical tubes. They compared their experimental measurements with results of CFD simulation performed using VOF scheme with two inlet systems. Different flow regimes (slug and annular) identified using CFD simulation were found to be consistent with ERT observations. Da Riva and Del Col (2009) used the VOF technique to simulate the development of churn flow at different superficial gas velocities (0.8 - 6 m/s) and pipe diameters (10 - 32 mm). The simulation showed the existence of a pulsating flow pattern of the liquid phase with flow reversal. The study confirmed the flooding mechanism of churn flow and demonstrated the formation of high-amplitude flooding-type waves due to air pockets.

Annular flow regime occurs at high superficial gas velocities. A two-phase flow simulation study (Dai et al. 2013) used the Eulerian-Eulerian and multi-fluid VOF method to characterize different flow regimes in vertical pipelines. The study compared gas holdup measurements with simulation results and found a reasonable match. However, the existence of the annular flow regime at 1 m/s of superficial gas velocity was reported, which might need further investigation as it comes under the slug flow regime in the flow pattern map.

Two-phase flow simulation studies in annular geometry are very limited. A recent study (Sorgun et al. 2013) encompassed the modeling of different flow patterns including dispersed bubbly, dispersed annular, plug, slug, and wavy annular flows using the mixture model in ANSYS CFX.

The inhomogeneous model was used with interphase force transfer considering the mixture and free surface models. At the inlet, the velocities and volume fraction of both phases were specified while the pressure boundary condition was implemented at the outlet. It was inferred that the pressure gradient would be higher for concentric annuli in comparison to the flow in fully eccentric annuli.

2.6 Experimental study

Experimental investigations are essential aspects of multiphase flow, which can provide insight into the flow characteristics. Besides this, experimental measurements can be used for model calibration and validation purposes. The problems with gas-liquid flows at high velocities and large pipe diameters have not been explored yet. Several experimental studies have been conducted in the past. However, the studies were limited to low velocity and small diameter pipes. Some of the experimental data and field measurements are presented in this section.

2.6.1 Two-phase flow in pipe

The experimental studies have been conducted in the past to characterize the multiphase flow in the pipe geometry. The flow characterizations are based on several parameters such as flow patterns, pressure gradient, volumetric liquid holdup, and void fraction. These parameters have been used to understand the mechanism of flow structures under certain operating conditions. In the context of WCD, the fluid flow velocities (flow rate) and liquid holdup/void fraction are related to the pressure gradient. Hence, the review of past experimental work is important to understand the nuances of multiphase flow in the pipe.

Several studies have investigated the pressure drop characteristics in two-phase flow properties (Sawai et al., 2004; Zangana et al., 2011; and Waltrich et al., 2015). Sawai et al. (2004) classified

the pressure gradient against the superficial gas velocity plot in four regions compared to the classical flow pattern map with variation in slope corresponding to superficial gas velocity. Zangana et al. (2010) presented the pressure drop and liquid holdup measurements for a wide range of superficial gas (3 - 16.25m/s) and liquid velocities (0.01 - 0.7 m/s). The experimental setup included 10.97 m long test section with 127 mm diameter. The results suggested that the variation in the superficial liquid velocities is the main contributing factors for the change in pressure gradients. Tang et al. (2013) conducted the experiments to study the bubble, slug, churn, and annular flow patterns in 0.5-inch (12.27 mm) diameter vertical pipe section. The study showed an increasing pressure gradient trend in the annular flow regime which was observed at the void fraction greater than 0.7.

Another experimental investigation was carried out by Zubir and Zainon (2011) using three different pipe diameter sizes (21, 47, and 95 mm). The main objective of the research included the study of void fraction and flow pattern transitions with variation is fluid flow velocities (superficial gas velocity: 0.1-2 m/s; and superficial liquid velocity: 0.08-1 m/s). The void fractions were captured using a constant electric current method (CECM) which is an extension of conventional conductance probe method. The flow structures were recorded using the high-speed video camera. The study suggests that the void fraction increases with an increase in superficial gas velocity while decreases with increase in superficial liquid velocity. It was also mentioned that the variation in superficial liquid velocity doesn't affect the flow transition behavior for higher pipe diameters (47 and 95 mm). Damir (2012) extended the experimental work and used 0.13 m diameter of the vertical pipe. The study included the superficial gas velocity up to 16 m/s. The main flow patterns observed were annular and churn during the test. The trends of the void fraction with respect to superficial gas and liquid velocities were similar to that reported by Zubir and Zainon (2011).

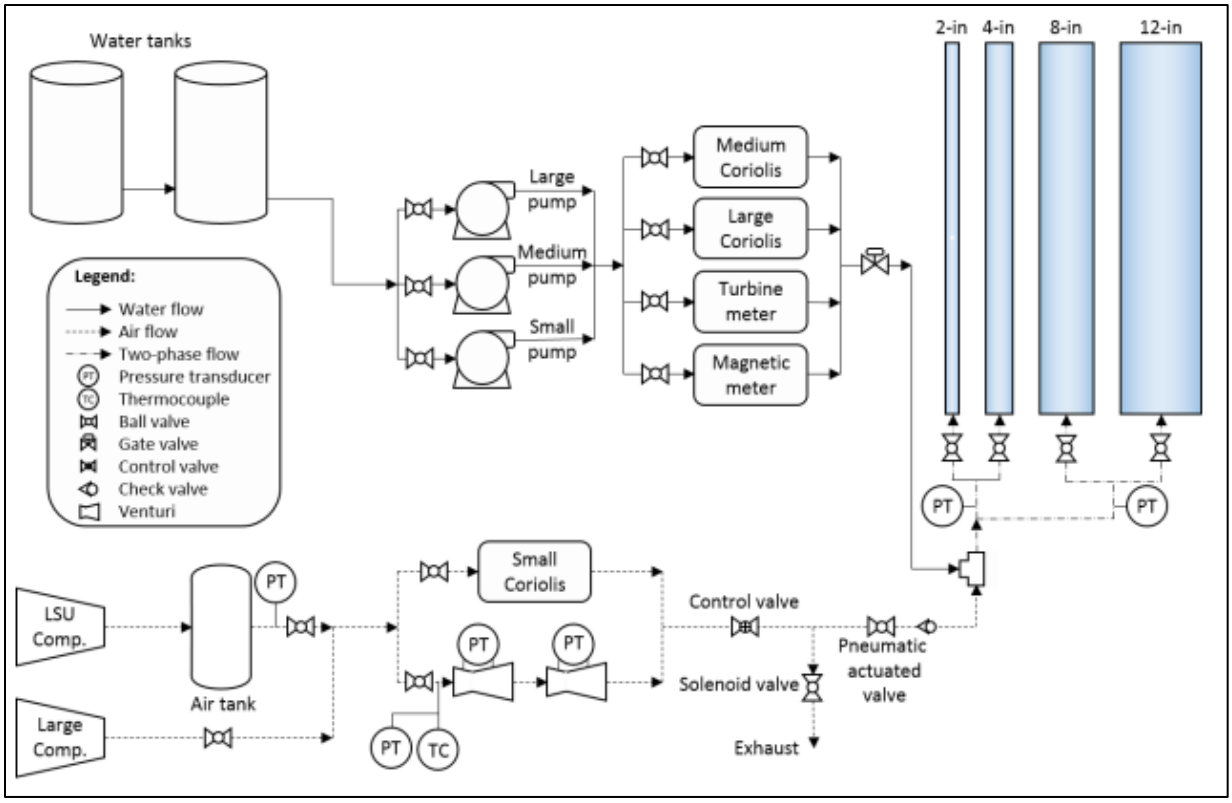

Figure 2.11 Schematic diagram of the test setup (Waltrich et al. 2013)

A recent study by Waltrich et al. (2015) sheds light on two-phase flow characteristics in the various pipe diameters. The experimental set-up included four sets of vertical clear PVC pipe diameters (2, 4, 8, and 12 in) as depicted in Figure 2.11. Experimental measurements covered an extensive range of flow rates (water: 6.26 to 795 gpm, air: 4.17 to 1666 scf/min). The flow patterns observed during the experiments included bubbly, slug, churn, and annular. Flow patterns maps were constructed using the experimental data from current and past studies as depicted in Figure 2.12 (Ohnuki and Akimoto, 1996 and 2000; Ali 2009; Waltrich et al., 2013). There are two major transition zones pointed out in this map: bubble to non-bubble and churn to annular.

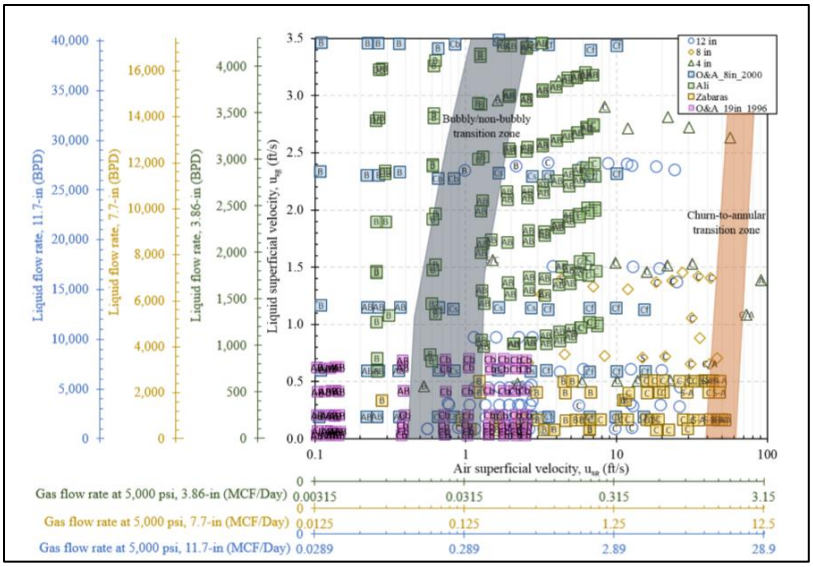

Figure 2.12 Flow regime map for large ID pipes (Waltrich et al., 2015).

Similar trends for liquid holdup and superficial gas velocities were reported in the experimental investigation as that of past studies. The study suggests that the liquid holdup decreases with gas flow rate regardless of the pipe diameter and not impacted by the liquid flow rate for pipe diameter below 4 in. The observation was attributed to the occurrence of slug flow. It was also noticed that the liquid holdup increases with superficial liquid velocity for 8 and 12 in pipe diameter. Cheng et al. (1998) used air and water for two-phase flow experiment in 0.0289 and 0.15 m pipe. The study suggests the absence of slug flow at higher diameter pipe (0.15 m) experiments. However, the lower diameter pipe (0.0289 m) experiment showed the presence of slug flow with oscillatory waves.

Shen et al. (2006 and 2010) investigated the localized phase distribution characteristics in 0.2 m vertical pipe diameter. The maximum superficial gas and liquid velocities investigated during this experiment were 1.12 and 0.218 m/s. The main flow patterns observed in this study were bubble, churn, and slug depending on the fluid flow velocities at different location of the test section. The bubble flow pattern occurred at relatively low superficial gas, and liquid velocities while slug and churn at relatively higher gas velocities. The churn flow was characterized by large deformed

bubbles contrary to the coalescent bubbles for slug flow. In addition to these flow patterns, two types of void fraction distribution peaks (wall and core peaks) were observed in the phase distribution data. The cause of such formations was attributed to radial velocity gradient, liquid and gas velocities, and bubble coalescence and breakup.

2.6.2 Two-phase flow in the annulus

Multiphase flow in the annulus is a challenging area of research, but its applicability is immense especially in the petroleum industry. In drilling and production operation, there is often a drill pipe inside the wellbore, and this arrangement is referred to annulus geometry where the fluid flows through the space between the two circular boundary walls. Such an arrangement is analogous to the pipe geometry; however, the flow dynamics are more complicated. Multiphase flow in an annulus has been subjected to analytical and experimental investigations in the past. However, past studies are limited to low fluid velocity (<30 m/s). Considering the extreme operational and in-situ conditions especially in deeper wellbores, it is essential to investigate the flow characteristics in the annulus at the higher side of the superficial gas velocity spectrum (>30 m/s). Furthermore, the available models have also not been tested for higher velocity. The past modeling results have only been compared with low-velocity experimental data. So, it will be crucial to investigate the workability of past models for the higher velocity and modify it as required.

The two-phase flow system has different topological flow configurations termed as flow regimes. The main flow regimes in the vertical fluid flow in the annulus are: (a)bubble, (b)dispersed bubble, (c)slug, (d)churn, and (e)annular (Venkateswararao et al., 1982; Kelessidis and Dukler, 1989; Caetano et al., 1992a; and Ozar et al., 2008). These flow regimes are identified by phasic interfacial structures which depends on various parameters such as phase characteristics, fluid flow velocities, geometries, and size (Julia et al., 2011). The investigation of vertical co-current upward flow at

low gas flow rates shows the presence of the bubbly flow pattern when the discrete gas bubbles are distributed in the liquid continuum. With the increase in the gas flow rate, the bubbles coalesce and form bullet shaped bubbles commonly known as Taylor bubbles or slugs. These bubbles move upward with the gas velocity, and the existing flow pattern is referred to as slug flow (Taitel et al., 1980). Further increase in gas flow rates destroys the slug flow geometry and consequently forms a chaotic flow regime known as churn flow (Ozar et al., 2008). At higher flow rates, the liquid flows adjacent to the walls with the core of the annulus filled with the gas continuum exists. This flow geometry is commonly referred to as the annular flow regime (Kelessidis and Dukler, 1989; and Caetano et al., 1992a). The basic characteristics of these flow geometries are like the flow in the pipe. However, the flow rates (both phases) criteria for the existence of these regimes differ.

The characterization of multiphase flow in the annulus had been on the focus of researchers over several decades. Sadatomi et al. (1982) conducted the single-phase and two-phase experiments in non-circular channels (concentric annulus, rectangular, and triangular) and used quick closing valve method to determine the void fraction in two-phase flow. The study concluded that the transition boundary of the bubble to slug is not influenced by hydraulic diameter greater than 10 mm. Ozar et al. (2008) investigated the values of distribution parameters (C_0 and C_1) for flow patterns in the annulus and concluded it to be consistent with those of a circular channel. The authors also studied the flow structure of the bubbles and concluded that the small bubbles move towards the wall where as large bubbles stay in the center due to lift and interfacial wall forces. In addition, the study included the modification of drift velocity correlation proposed by Hibiki and Ishii (2002) based on the asymptotic nature of void fraction measured in the experiment.

Caetano (1992a) investigated two-phase flow (air as gas phase and water as liquid phase) in the concentric annuli and concluded that the bubble rise velocity is inversely proportional to the

hydraulic diameter. The authors also showed a consistency of bubble rise velocity prediction with Sadatomi et al. (1968) model. The study comprised of the experimental and theoretical treatment of flow characterization. Though the work itself is wonderful, it only dealt with the friction dominated regime of the fluid flow. Most of the practical application of fluid flow has a continuous change in fluid velocity with the flow. A controlled test design was lacking in this experimental study required to capture the pattern of pressure drop and liquid holdup with the fluid flow velocity. Also, it was reported that the asymmetric Taylor bubbles change the fluid dynamics in the slug flow regime for the annulus compared to the flow in the pipe. However, the modeling work assumes the presence of symmetric Taylor bubbles in the annulus. The similar observation regarding the presence of asymmetric nature of Taylor bubbles had been made by other researchers too (Ferukawa and Sekoguchi 1986; Kelessidis and Dukler 1990; and Das et al., 1999a and 1999b). Kelessidis and Dukler (1990) developed the mechanistic model for slug flow transition including the asymmetric bubbles. Das et al. (1999a and b) incorporated the asymmetric Taylor bubbles in the characterization of the slug flow regime using Drift flux method. The study also proposed the mechanistic model for the slug to churn transition based on the flooding mechanism. Sun et al. (2004) presented a neural network model on conductance probe data to characterize the transition from cap bubble to slug flow. Julia et al. (2011) extended the experimental work for cap-slug to churn flow transition. In addition, Julia and Hibiki (2011) presented the transition model for the slug to churn flow regime based on drift flux approach.

Another important aspect of multiphase flow study is the pressure drop variation with superficial liquid and superficial gas velocity. The pressure drop prediction is flow regime specific. For the bubble flow regime, Caetano (1992b) used the concept of slippage between two phases and bubble swarm effect suggested by Harmathy (1960), Wallis (1969), and Fernandes et al. (1983). Hasan

and Kabir (1992) implemented the drift flux method to calculate slip velocity for bubble rise and suggest the flow parameter value to 1.2 for smaller pipes and 2.0 for larger pipes. Lage and Time (2000) used a similar approach to slippage and used the slip velocity calculation suggested by Papadimitriou and Shoham (1991). For the slug flow modeling, Hasan and Kabir (1992) used the approach from Barnea and Shemer (1986) to obtain the coefficient in the Taylor bubble rise velocity. The same value of the coefficient was also validated by Sadatomi et al. (1982). Caetano et al. (1992b) developed the hydrodynamic slug flow model using the film thickness evaluation method suggested by Fernandes et al. (1983) and McQuillan and Walley (1985). However, the method does not incorporate the effect of asymmetric Taylor bubble during slug flow. Very few studies have been reported for modeling the churn flow in the annulus. Hasan and Kabir (1992) suggested the method like slug flow for its characterization. Das et al. (1999b) Caetano (1992b) developed the mechanistic model for annular flow regime using the conservation of mass and momentum. Lage and Time (2000) used the mechanistic model by Keledessis and Dukler (1989) for flow regime characterization and extended it for prediction of pressure drop. However, this model neglects the entrainment of liquid droplets in the gas core.

2.7 High Mach Number Multiphase Flow

Mach number refers to the speed of sound. High Mach number (>0.3) multiphase flows generally exist in extreme conditions and termed as subsonic and supersonic flow. The subsonic condition is described as flow with Mach number ranging from 0.3 to 1, while the supersonic condition is attributed to flows with Mach number greater than 1. Multiphase flows encountered in regular oil and gas operations have low magnitude velocities (Mach number < 0.3). However, high velocities have been reported during catastrophic well control incidents. Reports from deep-water horizon blowout suggest the occurrence of cavitation of escaped gas and consequently leading to

supersonic discharge conditions. In the wake of similar incidents, a comprehensive effort must be made to understand the underlying problems arising in the flow field beneath such high-velocity discharge. Such high-velocity conditions are associated with the formation of shock waves. The generated shock waves lead to a change in velocity and density abruptly in the flow domain and consequently induces a discontinuity in the system. Earnshaw (1851) established these shock wave phenomena theoretically for thunder propagation with the supersonic velocity for the first time (Krehl, 2000). The shock wave propagation occurs in several engineering applications such as exploding coal dust in mines, accidental explosion in long pipes transmitting natural gas, exhaust pipes of reciprocating engines, volcanic eruptions, a rupture in nuclear vessels, and blast waves.

Shock waves are often associated with the speed of sound. The speed of sound in the single and two-phase fluid is different depending on the characteristics of in-situ parameters and medium properties. For example, the sound speed is approximately 4.2 times in water in comparison to the speed in the air. Also, introducing 1% of the air in water results in a sound speed of 100 m/s. Kieffer (1977) developed a model to predict the speed of sound in a two-component system. The model is applied in an adiabatic or isothermal condition which is expressed as:

$$c = \eta\rho_{LA}\left(\frac{G_{ait}}{P}\right)^{1/\gamma} + \exp\left(\frac{P_a - P}{K}\right)\left\{\left[(1+\eta)\rho_{LA}\right]^{1/2}\left[\frac{\eta\rho_{LA}G_{ait}^{1/\gamma}}{\gamma P^{(1+\gamma)/\gamma}} + \frac{1}{K}\exp\left(\frac{P_a - P}{K}\right)\right]^{1/2}\right\}^{-1} \quad (2.21)$$

where c is the speed of sound, η is the gas mass fraction, ρ_{LA} is the density of the liquid in the reference state (considered as 1 g/cm^3 at atmospheric condition), P is the pressure, P_a is reference pressure (considered as 1 bar/14.5 psi), K is the bulk modulus of water (2.2 x10^6 bars), G_{air} is the gas constant given by $T_0R_0/M\rho_0^{\gamma-1}$ (T_0 is reference temperature, R_0 is universal gas constant, M is molecular weight of air), γ is the adiabatic constant and depends on the thermodynamic properties of the gas. The equation showed reasonable agreement with the experimental data from Karplus

(1958) for air and water mixture. The sensitivity analysis was performed on several parameters such as void fraction, pressure, and temperature. The speed of sound was shown to increase with an increase in pressure which can be attributed to the effect of compressibility. At low pressure, with an increase in gas void fraction, the speed of sound was found to decrease at a low void fraction, reached a minimum value, and then followed an increasing trend as the void fraction approached one. However, at high pressures, a monotonically decreasing trend was observed. Similar trends were observed for isothermal as well as adiabatic cases.

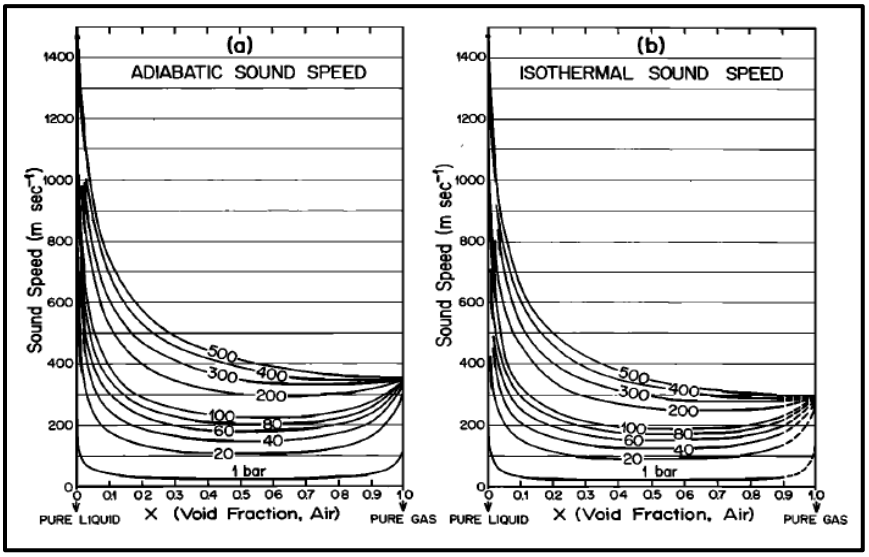

Figure 2.13 Variation of (a) adiabatic and (b) isothermal speed of sound in air-water mixture with gas void fraction and pressure (Kieffer, 1977)

Every fluid dynamics problem has specific characteristics. In order to understand the intricacies, experimental studies are traditionally conducted. Results of experimental investigations are the basis of the development of any theoretical model. Keeping this in mind, an extensive survey of past experimental works has been performed. The experimental investigations include two-phase high-velocity flow in tubes and shock waves in tunnels, chokes, and ducts. The next section present reviews of such studies.

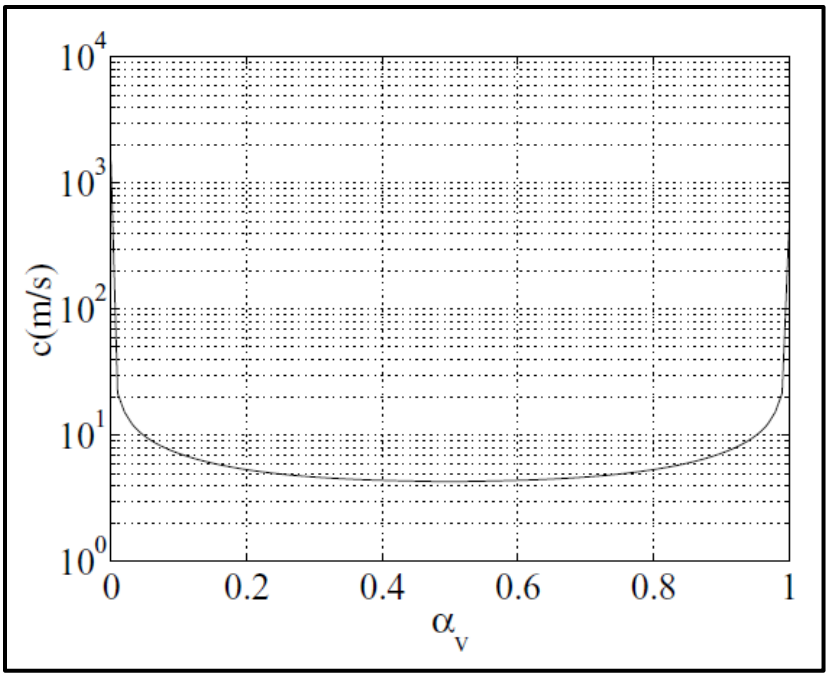

Figure 2.14 Variation in the speed of sound in multiphase mixture flow with a void fraction (Venkateswaran et al., 2002)

Venkateswaran et al. (2002) developed a numerical model to study the effects of compressibility in multiphase flow with transonic/supersonic conditions (Figure 2.14). It was assumed that the incompressible flow and low Mach number compressible flow exist for the pure liquid phase and pure vapor phase, respectively. The primary issue with such mixture flows with compressibility effects are a strong coupling of an acoustic phenomenon which can be resolved by characterizing the local regions. The model used time marching techniques for high-speed compressible flow. Different numerical techniques such as eigenvalue analysis, perturbation analysis, and preconditioning were employed to solve the equation of motion for volume fraction and mass fraction. The model was validated using the results for the standard shock tube problem. It is worthy to notice that in computational fluid dynamics, the numerical models are tested using a shock tube problem. The reason for using a shock tube problem as a means of validating the numerical scheme is the availability of an analytical solution for the shock tube problem.

2.8 Current WCD Modeling

The NTL No. 2015-N01 indicates that the WCD scenario should consider all hydrocarbon-bearing zones in each open-hole section as it is planned to be drilled. The dynamic and spatial changes in rock and fluid properties, multiphase flow pattern, saturation, operating pressure and temperature, and relative permeability are essential for accurate estimation of WCD (Hopper, 2015). Comprehensive modeling of such a dynamic and complex scenario cannot be decoded with conventional analytical models. With the advent of modern technology, the blowout tends to decrease. Nevertheless, unfortunate situations such as equipment failure and geological uncertainty invariably lead to incidents that in turn results in loss of wells, equipment, and even human life. To minimize the risk and, a priori estimation of WCD through holistic modeling is necessary.

There are several models which have evolved over time to predict the discharge rate in case of blow-out or explosion. One of the earlier works was carried out by Das et al. (1993). The model incorporated fluid dynamics, heat transfer, and pollutant dispersion effect. It can predict the quantity of spill, velocity, and the temperature at the outgoing jet, radiation intensity profile, and pollutant dispersion around the well. However, the effect of formation damage, sand migration, collapse, and coning are not included in the model. Similarly, a blowout simulator was developed by Oudeman et al. (1993) to conduct a sensitivity analysis of input parameters such as reservoir properties and consequently define the suitable relief well design or well killing sequence. It includes the inflow and outflow performances calculations to determine the existence of multiphase sonic flow condition across the choke geometries in a blowout well. The earlier presumption regarding the blow-out rate calculation at the point of intersection of inflow performance curve with well intake pressure curve for ambient pressure was studied. It was

concluded that the above presumption was true only for low to medium blow-out rate and in case of extreme blow-out rate, the outflow rate at sonic conditions across choke is more realistic. Pressure and temperature profiles are calculated simultaneously, using a modified form of Gray's correlations for wet gas and high GLR (Gas/liquid ratio) wells and, Dun and Ros correlation for low GLR wells. In addition to that, the Joule-Thompson effect was considered to simulate fluid properties. They observed that when the actual flow velocity approaches the sonic velocity, the total pressure drop tends to increase sharply resulting in an equilibrium flow rate (maximum flow rate).

Oudeman (2010) presented a validation for blowout rate simulator for subsea wells encompassing a comparison of calculated rate and estimates based on observable phenomena such as flame length and heat release rate. The nodal analysis method was applied for matching the inflow performance of the well to the vertical lift performance of the wellbore to estimate the blowout rate. It was observed that for onshore wells, the blowout rate is often controlled by the sonic outflow conditions because the pressure in the well exceeds atmospheric pressure by a factor of two or more. Another earlier study showed that the connection between high noise level around the well and erosion of wellhead components to the establishment of supersonic conditions at the surface (Oudeman et al., 1993). On the other hand, in offshore wells, there is hydrostatic pressure of water column at the mudline, which can be used for determining the flowing wellhead pressure of the blowing well. Hence, in offshore wells, the sonic condition is not likely to develop at the wellhead, and the total system performance is the critical factor.

Hasan et al. (1998) developed a combine wellbore-reservoir simulator to investigate the pressure-transient behavior of two-phase flow in deviated and vertical wellbores. The model analyzes wellbore flow numerically, and reservoir flows analytically. The convective and conductive heat

transport mechanisms are considered in the formulation of the model. A transient model was used to simulate the flow conditions at the onset of the maximum discharge. The model uses a numerical method to solve the mass, momentum, and energy balance equations for the wellbore fluid and analytical models for fluid flow in the reservoir. Fluid properties are estimated using black-oil model, and a mechanistic model (Hasan and Kabir 1992) was used to characterize the liquid holdup based on flow patterns. Another important consideration in this model was the tracking of gas bubble migration throughout the wellbore. The isentropic expansion was assumed to compute the theoretical sonic velocity. According to the model, the flow rate increases with increasing well productivity, tube diameter, pressure in the reservoir, and the gas-oil ratio (GOR). Blowout rate simulators have been useful tools to forecast and manage a blowout. In 1990, dynamic flow simulator OLGA (a Schlumberger proprietary software) was used in a blowout well control in the North Sea by Rygg and Gilhuus. The dynamic blowout rate, wellbore flowing temperature and dynamic wellbore pressure profiles were considered in their analysis. Liu et al. (2014) developed a simulator using a wellbore flow and heat transfer model. The model formulation combines flow in the reservoir, wellbore, and their interaction. The model treats a blowout as a type of drawdown changing over time. Therefore, flow equations applied for drawdown test analysis are used by neglecting the superposition in time for blowout calculation. It was reported that the existence of sonic velocity rarely occurs for single-phase oil well blowout because of high hydrostatic pressure gradient, which does not allow such high velocity in the wellbore. Recently, the more advanced version of OLGA, a dynamic kill simulator was used to analyze worst-case blowout scenarios and evaluate the impacts of different operational parameters during the killing process (Yuan et al., 2015). Among several other available multiphase flow models implemented in simulators, the OLGA steady-state model (OLGAS, 2016), the LedaFlow

Point model (Ledaflow, 2016), and the TUFFP Unified model are capable of analyzing two-phase gas-liquid flows for all inclination angles, pipe diameters, and fluid properties (Shippen and Bailey, 2012). OLGAS can analyze 300-1320 psia operating pressure, superficial gas velocity up to 43 ft/s, and liquid superficial velocity up to 13 ft/s. This simulator was validated using TILDA databased. LEDA-PM was also confirmed using additional experimental data to TILDA database. TUFF unified model is based on the rule of 10. According to the rule of the tomb, this simulator can be used in deviation angles in the range of +/- 10^{o}, liquid holdup more than 10%, internal pipe diameter less than 10 in., and oil viscosities less than 10 cP. The comparison of the software is presented in Table 2.6. The Gemini simulator developed by Gemini Solutions predicts the WCD rate of oil and gas well blowouts. However, the basis of the worst case discharge calculation in this software is based on nodal analysis and uses empirical correlations for the estimation of pressure drop in the system (Worst Case Discharge, 2016).

Table 2.6 Comparison of available industry software

Features	TUFF	Leda-PM	OLGA
Continuity	Three mass Equation	Nine Mass Equations	Five Mass Equations
Momentum	Three Equations: Gas pocket in slug Oil and water in film zone Oil and water in slug body	Three Equations: Gas bulk + liquid Droplets Oil bulk + gas bubble and water droplet Water bulk + gas bubble and water droplet	Three Equations: Gas-liquid Droplets Hydrocarbon Film Water Film
Viscosity Model	Brinkman	Continuous Phase	Pal and Rhodes
Flow Regimes	Stratified Intermittent Annular Bubbly Dispersed Bubble	Stratified smooth Stratified wavy Slug Annular Bubbly	Stratified smooth Stratified wavy Slug Annular Bubbly
Model type	Unified mechanistic	Transient mechanistic	Steady-state Mechanistic

2.9 Chapter Summary

Worst-case discharge (WCD) generally arises during well control events. Hence, a review of past well control incidents and their relevance in the context of worst-case discharge are presented. The WCD estimation requires integration of reservoir models and hydrodynamic models through nodal analysis. The hydrodynamic models depend on the accuracy of multiphase flow characterization. Past studies on multiphase flow suggest that the effect of geometry, setting up the governing equations, and solution approach pose a severe challenge for tackling the multiphase flow modeling problem. Most of the errors reported for pressure gradient in the past literature study are around 10% percent for empirical correlations. However, these correlations are mainly used in the industry for WCD estimation. Analytical and mechanistic models are more sophisticated than empirical models, but these models are complex and need rigorous testing for its suitability in full-fledged WCD estimation program. In addition, these models are never tested for high-velocity conditions. Numerical models have the potential to address the intricacies of multiphase flow characteristics but are computationally costly. Hence, it can be used to facilitate the understanding and development of multiphase flow modeling.

Most of the experimental studies suggest a significant change in axial pressure profile at high velocities. In addition, multiphase flow characteristics in the annulus exhibit considerable deviation from pipe flow. The investigation of subsonic and sonic conditions in multiphase flow experiments are very limited. However, the speed of sound in multiphase flow depends on several parameters such as upstream pressure, void fraction, and ambient conditions.

Chapter 3: Experimental Study

3.1 Overview

Experiments are conducted to get an insight into the real phenomenon. Past experimental works have not been focused on the high fluid velocity conditions in the vertical annulus and pipe. This study is used to capture the pressure gradients and liquid holdup in high-velocity conditions. The idea behind the experimental work is to use the experimental data for verification of hydrodynamic models relevant for worst-case discharge estimation. As a part of this study, a high-velocity flow loop was constructed, and experiments were carried out to mimic the flow characteristics in such conditions. In addition, the sonic conditions in the flow loop were also investigated. Several pieces of evidence were used to confirm the sonic condition which was later used to develop a correlation for a sonic model for two-phase flow. The details of sonic correlation are discussed in section 5.5. Following are the main contribution of this study:

- An experimental study is presented for superficial gas velocity range 5 to 137 m/s and the superficial liquid velocity ranging from 0.294-1.795 m/s. Air and water are used for gas and liquid phase, respectively. The details can be found out in Section 3.6.
- An extensive flow pattern map for the flow in annulus and pipe was created using the current and past experimental data. The current flow regime is quantified using the videos recorded during the experiments.
- The pressure gradient and liquid hold-up were primary measurements and are investigated and presented in Section 3.6.1 and 3.6.2.

- The sonic conditions were observed during the flow in the pipe which was verified using several means such as the pattern of upstream pressure, the pressure gradient development, and sound captured during the experiment. The details are presented in section 3.6.2.6.

3.2 Description of the Flow Loop

A new 28 ft high multiphase vertical flow loop was constructed. The flow loop was comprised of several instruments and parts such as test section, pump, compressors, Coriolis flow meters, high frame speed camera, pressure and temperature sensors, quick closing and modulating control valves, and differential pressure cells. The test section included pipe and annulus test sections. The annular geometry consisted of 83 mm as the outer diameter and 35 mm as inner diameter while pipe geometry consisted of 83 mm diameter. The concentricity of the inner pipe was maintained by the prototype centralizer which was fixed at the exit and entrance section of the test set up for the annulus. The whole test section was mounted on a steel frame attached to the vertical wall to contain the vibrations during the high-velocity fluid flow and incurring water hammering effect during the test. In addition, the test setup was insulated using foam to minimize the heat loss during the experiment.

Three differential pressure transmitters were used, one for the liquid hold up (L1) and two for pressure gradient measurements (DP) in each test section. These transmitters had an accuracy of 0.05%. One is located at the base to measure liquid hold-up while two of them were installed at the top and used for the pressure gradient measurement. Five pressure gauges were installed throughout test sections as depicted in Figure 1. These pressure transducers had 0.68 MPa limit with an accuracy of 0.5%. In addition, three temperature sensors were used to characterize the temperature profile of fluid during the tests. Two centrifugal pumps equipped with Variable Frequency Drives (VFD) and connected in series, were used to pump water from the tank in the

test section. Coriolis flowmeter was used to measure the liquid flow rate and was installed on the flowline. Three compressors were used to pump the air in the system to achieve the desired gas flow rate. Two Coriolis flowmeters were installed to measure the gas flow rates in the section. The modulating valves in the input line were used to control the gas flow rate. Two fast reacting butterfly valves were installed at the inlet and outlet section of the flow loop to control the flow rates. The butterfly valves were controlled by prototype program implemented in the data acquisition system so that the inflow and outflow from the system were maintained smoothly and avoid any dangerous side effects of high-velocity experiments. The operating pressure of these valves was 0 - 1.6 MPa and operating temperature are -50 to 200^{o}C. Bypass valves were used to return the water to the tank after the completion of the experiments. The check valve was used to prevent the air from entering the water flow line and contain the water hammering effect over the course of the experiment. The experimental setup allowed the determination of liquid holdup base on liquid level measurement. Moreover, transparent polycarbonate viewing port on the test section was used for visual observation of the flow regimes, and the flow evolution was recorded with a high-speed camera.

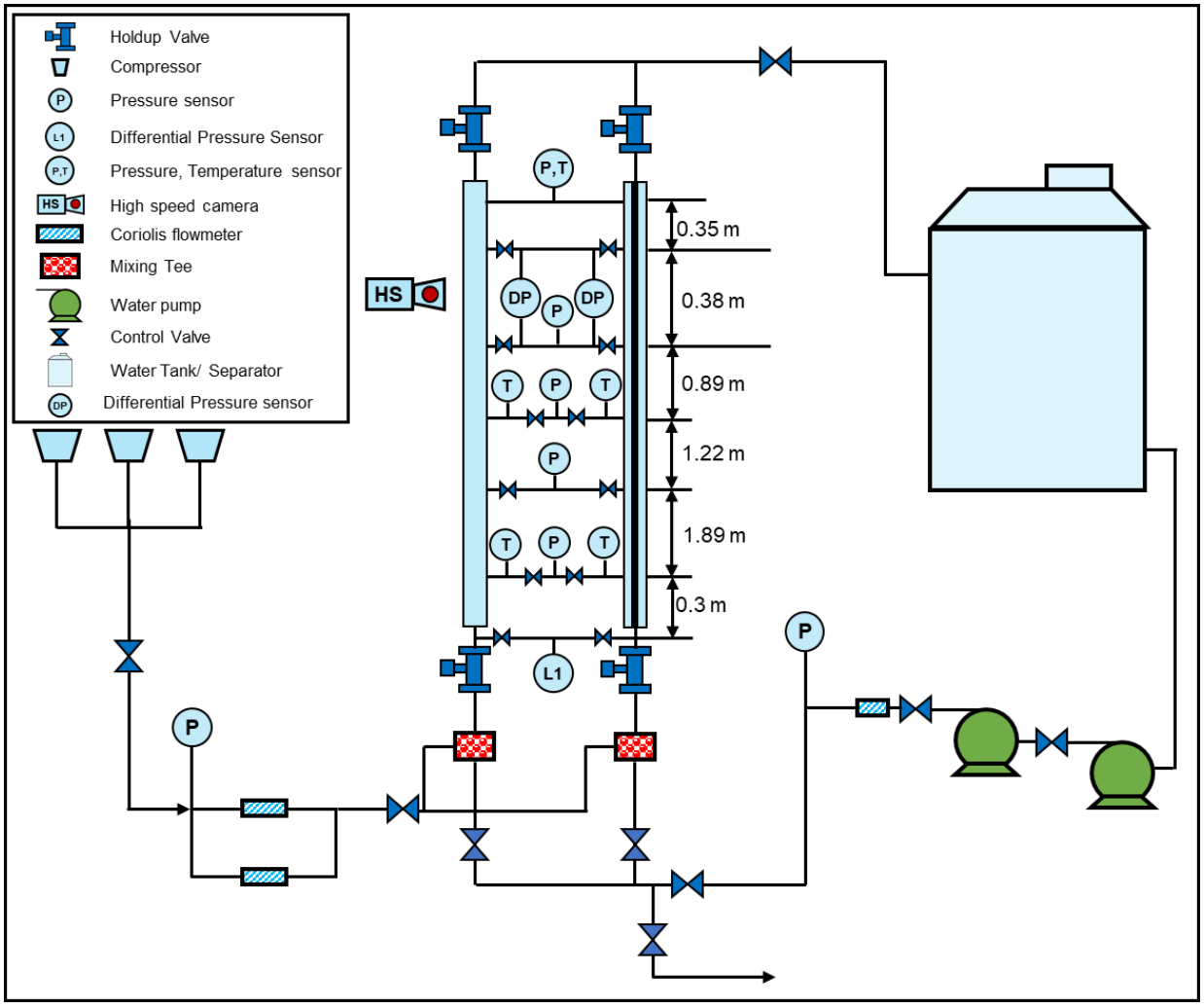

Figure 3.1 Schematic of the experimental flow loop

Measuring instruments installed on the test sections are differential pressure transmitters, gauge pressure transducers, and temperature transmitters. The instruments are used to monitor pressure and temperature change occurring in the test sections during the experiment. The experimental setup allows the determination of liquid holdup base on liquid level measurement. Moreover, transparent polycarbonate viewing ports on the test sections permit flow regimes detection by recording video clips during the experiments. Table 3.1 summarizes the operational range and accuracy of the incorporated instrumentation.

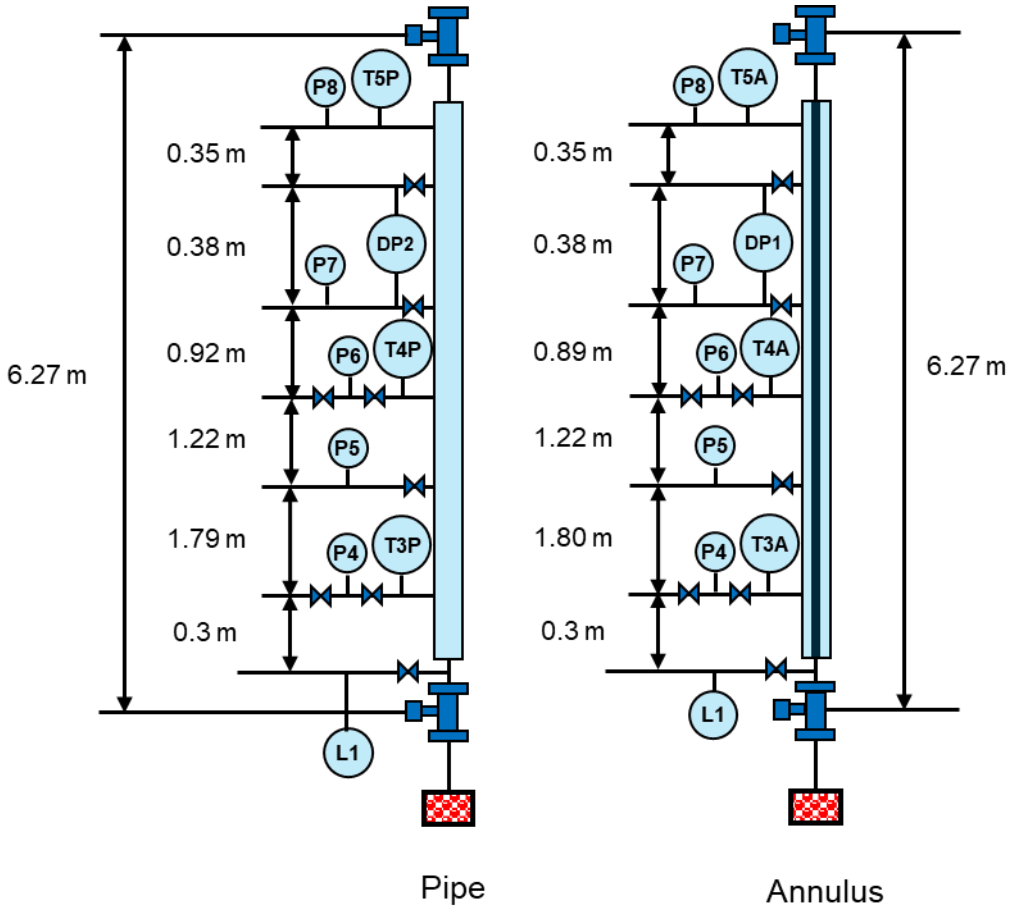

Figure 3.2 Schematic of the test sections

Table 3.1 Overall instruments description

Instrument	Accuracy	Range
Flowmeters	$\pm 0.35\%$	0 to 2564 lbm/min
Differential Pressure Transmitter	$\pm 0.05\%$	0.025-4 kPa
Gauge Pressure Transducer	$\pm 0.5\%$	0 to1378.21 kPa
Temperature Transmitter	$\pm 0.2\%$ and $\pm 0.1\%$	$-50℃$ to $500℃$ and $-50℃$ to $200℃$

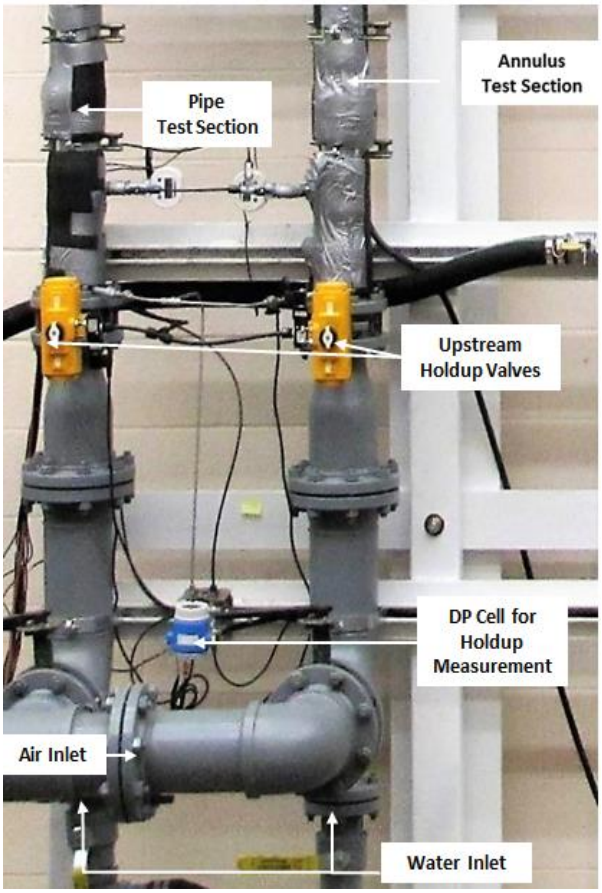

Figure 3.3 Snapshot of the bottom test section

3.3 Flow Loop Components

The different components of the flow loop are described in Appendix B.

3.4 Experimental Procedure

In the high-velocity experiments, the proper experimental procedure is required to make the tests efficient and safe. During the current experimental investigation, a proper methodology was outlined. First of all, the air control valves were opened to initiate the air injection in the flow loop. Consequently, the water was slowly injected into the system using a variable frequency drive (VFD) control system from centrifugal pumps. The air and water injection were gradually increased, and the flow was continued at desired rate till the steady state was achieved. The whole

test condition was monitored through an in-house data acquisition (DAQ) system. The test data was collected in the real-time though DAQ system. After the establishment of steady-state conditions and collection of the desired data for enough time, the videos were recorded to capture the visual observation of flow pattern using the high-speed camera. Then, holdup valves were closed by initiating the quick closing valve to trap the fluid in the test section. The liquid holdup was measured using the differential pressure transducer (DP cell for holdup as depicted in Figure 3.2). After gathering the holdup data, the fluid was slowly vented out from the test section using the control valve.

3.5 Experimental Program Description

Preliminary experimental tests were conducted to verify the accuracy of measurements. Water was used as a test fluid in the preliminary test. The data obtained from the preliminary tests are analyzed and compared with predictions of established correlations for smooth pipe and annulus. After completion of the preliminary test, the main experiments were performed. The experimental test matrix is shown in Table 3.2.

Table 3.2 Experimental test matrix

Test	Superficial Water Velocity (m/s)	Superficial Air Velocity (m/s)	Type of test
Preliminary Test	0.47-1.2	-	Single (Water)
Low Velocities	0.23 – 3.5	8 - 20	Multiphase flow
Medium Velocities	0.23 –3.5	21 - 80	Multiphase flow
High Velocities	0.23 – 3.5	80 - 160	Multiphase flow

3.6 Experimental results and discussion

3.6.1 Multiphase flow in the annulus

3.6.1.1 Validation

The experimental data was compared with the established correlation for the friction pressure loss in the annulus. Equations 1 is the standard formula for friction pressure loss.

$$\Delta P = f\frac{2L}{D_h}\rho V^2 \tag{3.1}$$

where ΔP is the pressure loss, L is the length, D_h is the hydraulic diameter, ρ is fluid density, V is the mean fluid velocity, and f is the fanning friction factor. The single-phase friction factor can be calculated from the correlation suggested by Caetano (1992a):

$$\frac{1}{\left\{f(a)^{0.45e^{\frac{-(Re-3000)}{10^6}}}\right\}^{0.5}} = 4.0log\left[Re\left\{f(a)^{0.45e^{\frac{-(Re-3000)}{10^6}}}\right\}^{0.5}\right] - 0.4 \tag{3.2}$$

where R_e is the Reynolds number, and a is the friction geometry parameter and can be calculated from the equation below:

$$a = \frac{1+K^2-\frac{1-K^2}{ln(1/K)}}{(1-K)^2} \tag{3.3}$$

where K is the ratio of the outer and the inner diameter of the annulus. The single-phase experiments were conducted at the ambient conditions by varying the liquid flow rate from 151.4 to 378.5 Liters per minute (LPM). The corresponding velocities for flow rates were 0.573, 0.86, 1.146, and 1.432 m/s. The experimental data for pressure loss and friction pressure loss calculated using the above-described equations showed a reasonable match. The maximum difference between the calculated and measured pressure loss was up to 17% corresponding to 1.432 m/s of

water velocity in the annulus. The difference between the measured and predicted data can be attributed to the entrance effects and pipe roughness of the annular test section.

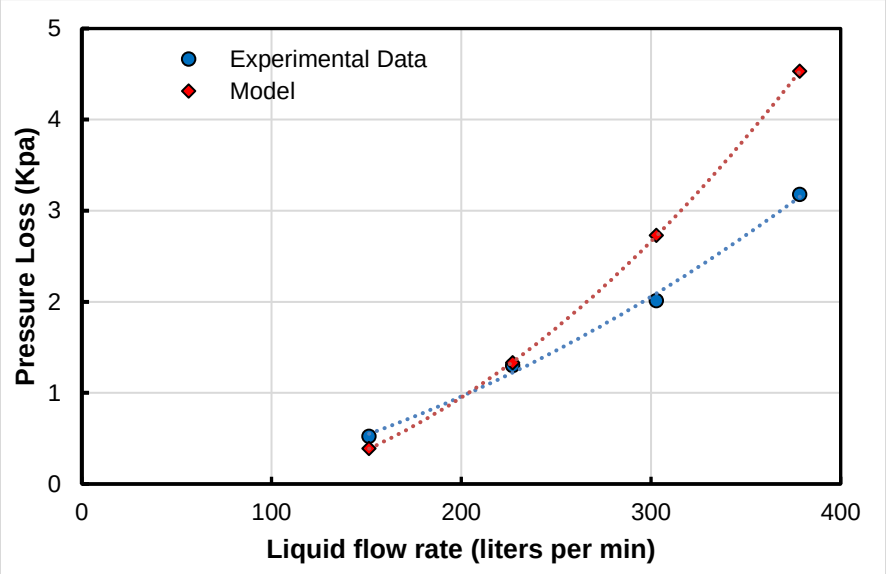

Figure 3.4 Measured and predicted pressure drop for single-phase flow in the annulus

The experimental setup is calibrated using the single-phase calculation. However, it is also important to validate the two-phase flow measurements. Due to the unavailability of any standard formulation for the multiphase flow characteristics, it is challenging to validate the multiphase flow experimental data in the annulus. In addition, the annulus experiments conducted in the past had different geometrical dimensions compared to the one used in the current setup. Furthermore, it is difficult to match the superficial gas-liquid velocities from any reported data exactly. Caetano (1985) experimental set-up had the closest dimension (76.2mm × 42.2mm) of the test section in comparison to this study (83mm × 35mm). Hence, the data from Caetano (1985) experiments were chosen for the validation. Table 3.3 presents the comparison of the Caetano (1985) data and the current experimental data. The current study showed a lower pressure gradient and higher liquid holdup in comparison to Caetano's experimental data. This difference can be attributed to the

change in geometry and superficial velocities in both cases. The higher annular space resulted in the higher holdup and reduced pressure gradient in the present study.

Table 3.3 Experimental data validation

	Caetano (1985) experimental data				Current experimental data			
Cases	Gas Velocity	Liquid Velocity	Liquid Holdup	Pressure gradient	Gas Velocity	Liquid Velocity	Liquid Holdup	Pressure gradient
	m/s	m/s		KPa/m	m/s	m/s		KPa/m
1	13.023	0.30	0.13	3.167	13.05	0.32	0.16	2.275
2	8.093	0.30	0.17	2.737	9.41	0.29	0.21	2.268
3	16.61	0.52	0.12	4.682	16.83	0.51	0.18	3.039
4	16.68	0.55	0.13	5.112	16.61	0.52	0.20	3.043
5	13.535	0.97	0.17	7.08	13.86	0.97	0.19	3.918
6	12.708	1.17	0.19	7.51	13.02	1.12	0.25	4.446

To establish additional confidence in experimental data collection, the trends of both studies (current and Caetano, 1985) were compared especially at higher superficial gas velocity. Three data sets from Caetano (1985) experiments were identified which had the same superficial liquid velocities and different superficial gas velocities as shown in Table 3.4. It should be noted that the higher superficial gas velocity range was chosen. Comparison of each case reveals that the pressure gradient increases with an increase in superficial gas velocity. This observation is contrary to the usual trends where the pressure gradient decreases with an increase in superficial gas velocity. However, it is worth noting that this prediction is based on a gravity dominated flow regime. However, at higher superficial gas velocities, the flow characteristics (pressure gradient) are dominated by frictional pressure loss. This increasing trend is in sync of the current lab test data and can be seen more evidently in overall results (Section 3.6.1.4).

Table 3.4 Past experimental data (Caetano, 1985)

Cases	Gas Velocity	Liquid Velocity	Liquid Holdup	Pressure gradient
	m/s	m/s		KPa/m
1	14.9	0.003	0.03	0.571
	9.0	0.003	0.00	0.516
2	13.0	0.299	0.13	3.177
	8.1	0.299	0.17	2.736
3	14.4	0.031	0.05	1.003
	8.9	0.031	0.09	0.952

3.6.1.2 Flow Regimes in Annulus

The main flow regimes observed in the annulus are bubble, slug, dispersed bubble, churn, and annular as shown in Figure 2.4. However, at the higher superficial gas velocity, the annular flow regime exists. As this study caters with high superficial gas velocity, mainly two flow regimes (churn and annular) were encountered during the experiments. The churn flow mechanism in the annulus is yet not adequately understood. Various studies have outlined a different mechanism for its formation even in a vertical pipe (Mishima and Ishii, 1984; Hewitt, 1985; Dukler and Taitel, 1986). Mishima and Ishii (1984) and Hewitt (1985) postulated that the liquid waves are carried through the large waves and pick up the liquid from the falling film on the walls. Dukler and Taitel (1986) ascribed the entrance effect as the main contributor to the evolution of churn flow. In the current experimental study, churn flow pattern consisted of a chaotic frothy mixture of gas-liquid moving upward and downward in the entire annulus. During the flow, the liquid film falls and mixes with the gas phase, forms a temporary bridge, and lifted upward again by the fast-moving gas. Figure 3.5a-3.5c shows a sequential flow in different frames of flow structure within 1 second. It is clear from figures 3.5a and 3.5b that the liquid is vigorously interacting with the gas while in Figure 3.5c the liquid mixed with the gas moves upward. In the real-time video, it was observed that this mixture moves upward and then, the same sequence is repeated.

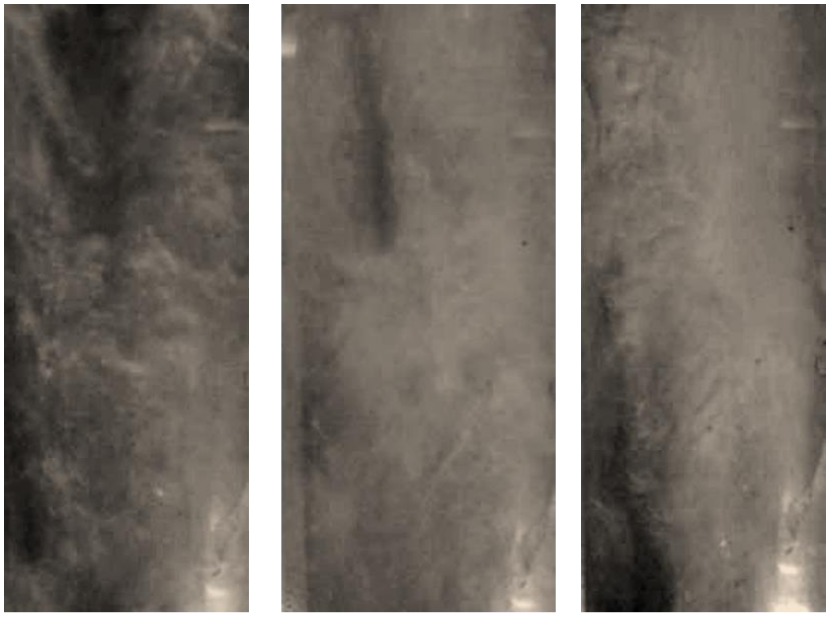

Figure 3.5 Visual images of churn flow regime in the annulus (Vsg = 9.181 m/s and Vsl = 0.296 m/s)

Further increase in gas velocity, the flow changed to the annular type of flow, where the flow was more streamlined toward the direction of the flow. The flow became smoother, where the gas phase moves upward in the core of the annulus and liquid film on the walls as shown in Figure 3.6. It was also observed that with an increase in the gas velocity, the gas starts entraining the liquid film on the wall. The gas eventually destroyed the liquid film on the wall, and a gas dominated mist flow was encountered.

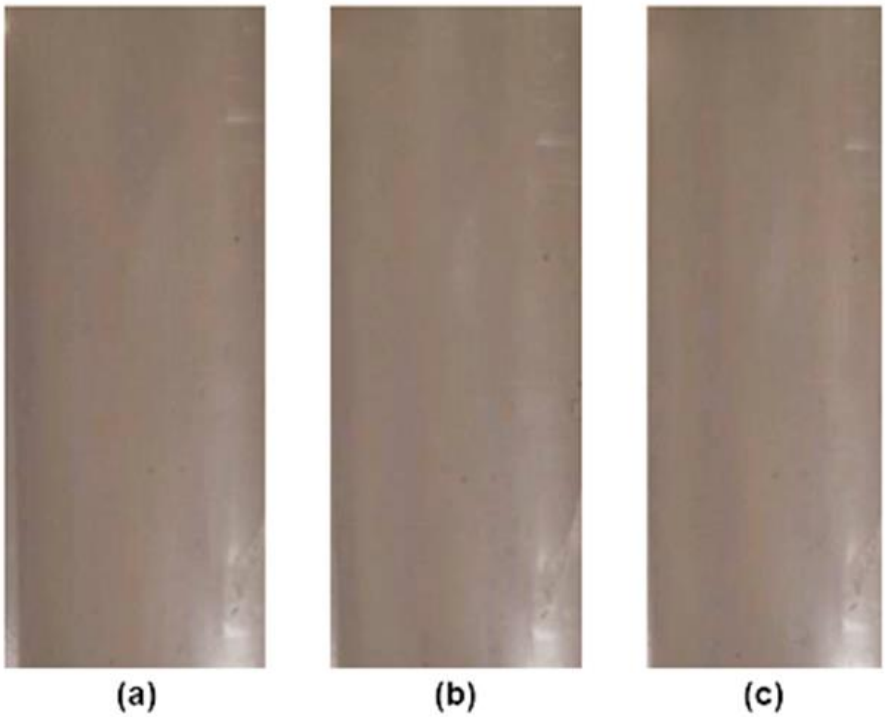

Figure 3.6 Visual images of annular flow regime in the annulus (Vsg = 18.553 m/s and Vsl = 0.303 m/s)

The flow pattern map is developed by adding the Caetano (1985) experimental data to the current experimental data on the superficial gas velocity vs. superficial liquid velocity plot. The map (as shown in Figure 3.7) includes five distinct flow patterns data: (a)bubble, (b) slug, (c) dispersed bubble, (d) churn, and (e)annular. The boundary of the bubble to slug transition is based on the modified Taitel et al. (1980) model as depicted in equation 3.4.

$$V_{sg} \geq \frac{V_{sl}}{4} + 0.306\left[\frac{(\rho_l - \rho_g)g\sigma}{\rho_l^2}\right]^{0.25} \tag{3.4}$$

where, Vsg is superficial gas velocity, Vsl is superficial liquid velocity, ρl is the density of the liquid phase, ρg is the density of the gas phase, σ is surface tension, and g is the acceleration due to gravity. The theoretical boundary of the bubble/slug to dispersed bubble is developed based on the Taitel et al. (1980) criteria using the hydraulic diameter concept as depicted in the following equation.

$$2\left[\frac{0.4\sigma}{(\rho_l-\rho_g)g}\right]^{0.5}\left(\frac{\rho_l}{\sigma}\right)^{0.6}\left(\frac{2f}{D_h}\right)^{0.4}V_m{}^{1.2}=0.725+4.15\left(\frac{V_{sg}}{V_m}\right)^{0.5} \quad (3.5)$$

where f is the Fanning friction factor calculated using a homogenous mixture of gas and liquid phase, Vm is the mixture velocity (sum of superficial gas and liquid velocity), Dh is the hydraulic diameter (difference of the outer diameter, Dc and the inner diameter, Dt). There are two boundaries (slug/bubble to dispersed flow) which are presented in the flow regime map. This difference is due to different hydraulic diameters corresponding to the Caetano and current laboratory set up. The other theoretical boundary for dispersed flow to slug flow is based on the criterion represented by equation 3.6 (Caetano, 1985).

$$V_{sg}\geq 1.083V_{sl}+0.796\left[\frac{(\rho_l-\rho_g)g\sigma}{\rho_l^2}\right]^{0.25} \quad (3.6)$$

Apart from the above-discussed boundaries, three experimental boundaries are also suggested to characterize the transition from churn to annular and slug to churn.

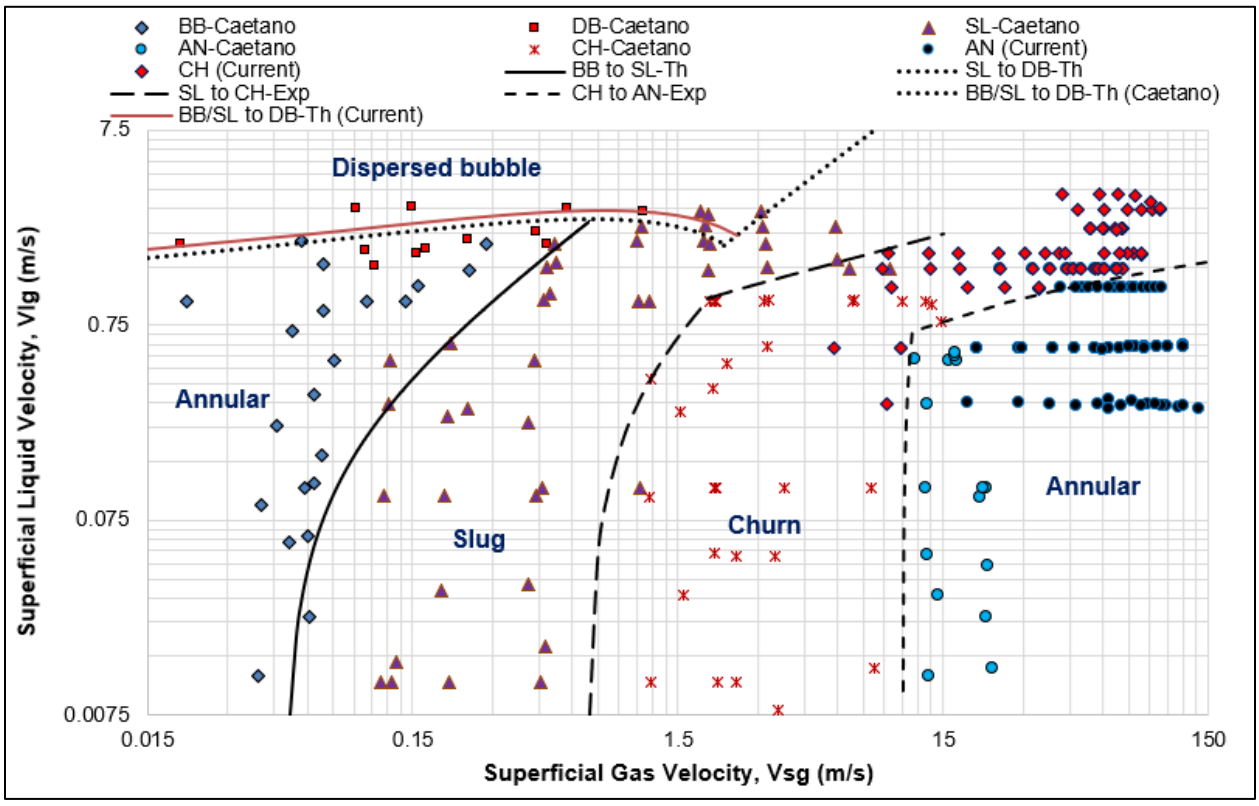

Figure 3.7 Flow regime map for annulus

Note BB: Bubble, DB: Dispersed bubble, SL: Slug, AN: Annular, CH: Churn, Th: Theoretical, Exp: Experimental.

3.6.1.3 Liquid Holdup Measurement in Annulus

In multiphase flow experiments, the liquid holdup significantly affects the flow patterns and consequently pressure drop. Therefore, the accuracy of its measurement to vital to characterize the dynamics of the flow. Nowadays, there are several methods such as conductance probe, impedance method, and closing valve technique, which can be implemented to capture this parameter. The conductance and impedance probes are based on putting up the wire mesh in the flow conduit. Ozar et al. (2008) used the conductivity probe and normalized probe signals to capture the local flow parameters such as interfacial area concentration, bubble interface velocity, and void fraction in the radial direction. Das et al. (1999a) used the electrode probes at different azimuthal and axial positions to understand the physical mechanism of transition boundaries of different flow regimes (bubbly-slug and slug-churn). The study used the probability density function analysis on the

signal data to characterize local phase distribution based on the methods proposed by Jones and Zuber (1975). Harvel et al. (1999) presented the void fraction distribution study in the annulus using real-time neutron radiography, and a high-speed X-ray computed tomography.

However, considering the high-velocity experiment and associated vibrations in the current work, these flow characterization techniques might lead to additional noise in the data. Hence, the simplest yet robust approach (quick closing valve method) was implemented using different pressure (DP) cell sensor. In this method, DP cell sensors were used to measure the accumulated hydrostatics pressure of the residual liquid column. The first step of any measurement technique is to validate the measurements obtained from this. The implemented liquid hold-up measurement technique was validated by comparing the DP cell measurement with the ratio of trapped residual liquid and the total volume of the test section during the quick closing of the valves in the single phase (liquid) experiment. The difference between these two methods was within 1%.

As described earlier in section 3.4, the tests were designed to see the existence in the pattern of the results. The liquid holdup results are presented in Figure 3.15. It decreases asymptotically with an increase in superficial gas velocity, whereas it increases with an increase in superficial liquid velocity. It is evident from figure 3.8 that the increment in the liquid holdup at a low superficial gas velocity corresponding to the increase in liquid velocity is significant. However, this pattern diminished with an increase in superficial gas velocity.

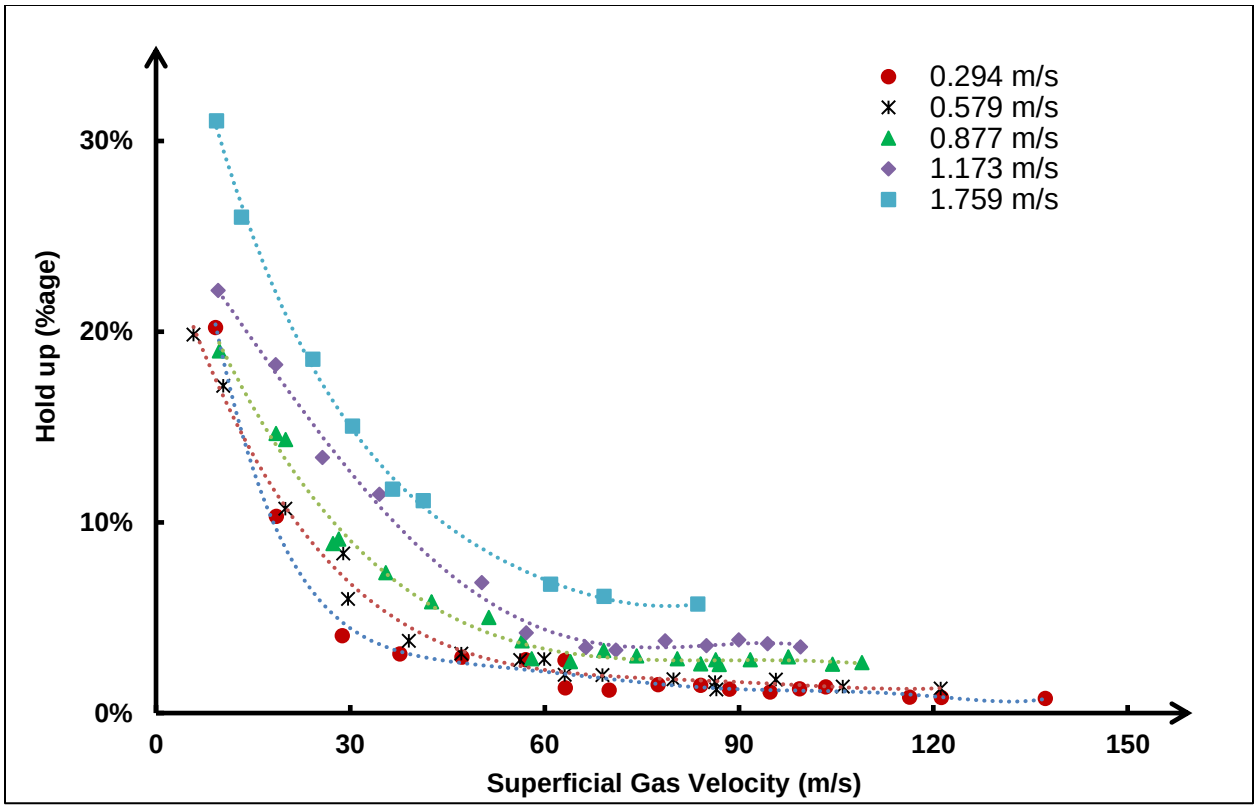

Figure 3.8 Liquid holdup measurements in the annulus

3.6.1.4 Pressure Gradient in Annulus

The pressure gradient is one of the critical aspects of the multiphase flow experimental study. The measurements were taken systemically to capture the pattern of influence for superficial liquid and gas velocity on it. Hence, the liquid flow rate was kept constant, and the gas velocity was varied in each set of experiments. The liquid flow rate implemented during the experiments included 77.5, 155.0, 227.1, 302.8, and 454.2 liters per minute (LPM). Due to mixing and fluid interaction, it is tough to maintain the exact liquid flow rate and consequently superficial liquid velocity. Table 3.5 gives the variation in superficial liquid velocity corresponding to each flow rate. This variation can be attributed as the cause for deviation in the smooth trend of the pressure gradient plots as evident in Figure 3.9. Each set of the experiments included variation in superficial gas velocity ranging from 9.18 m/s to 137.3 m/s.

Table 3.5 The liquid flow rate and superficial liquid velocity variation

Set	Liquid flow rate	Mean Superficial Liquid Velocity	Standard Deviation
	Liters/min	m/s	
1	77.5	0.294	0.008
2	155.0	0.579	0.008
3	227.1	0.877	0.008
4	302.8	1.173	0.002
5	454.2	1.759	0.008

During the experiment, the increasing trend of pressure gradient was recorded corresponding to fluid velocities. At the lower spectrum of change in superficial gas and liquid velocity, the pressure gradient increase was not significant; however, as the superficial gas velocity increased the increment in pressure gradient was substantial. Figure 3.9 shows that the difference in pressure gradient for the superficial gas velocity at 28 m/s is 1 KPa/m corresponding to the liquid velocity of 0.294 and 0.579 m/s while the difference becomes 5 KPa/m when compared at 121 m/s. In addition, the pressure gradient data is at the onset of asymptotic behavior at higher superficial gas velocity (>100 m/s). This behavior implies that the pressure gradient increases while the velocity becomes constant at very high superficial gas velocity. This increase in pressure gradient can be attributed to the increase in density of air while not affecting the gas flow rate. It is expected that if the upstream gas flow rate is increased further, the sonic condition might be established in the annulus section. For a given liquid superficial velocity, the pressure gradient increases with superficial gas velocity showing the dominance of friction pressure loss component in the total pressure drop. Finally, it can be concluded that the pressure gradient increases with respect to change in superficial gas and liquid velocity in the higher range.

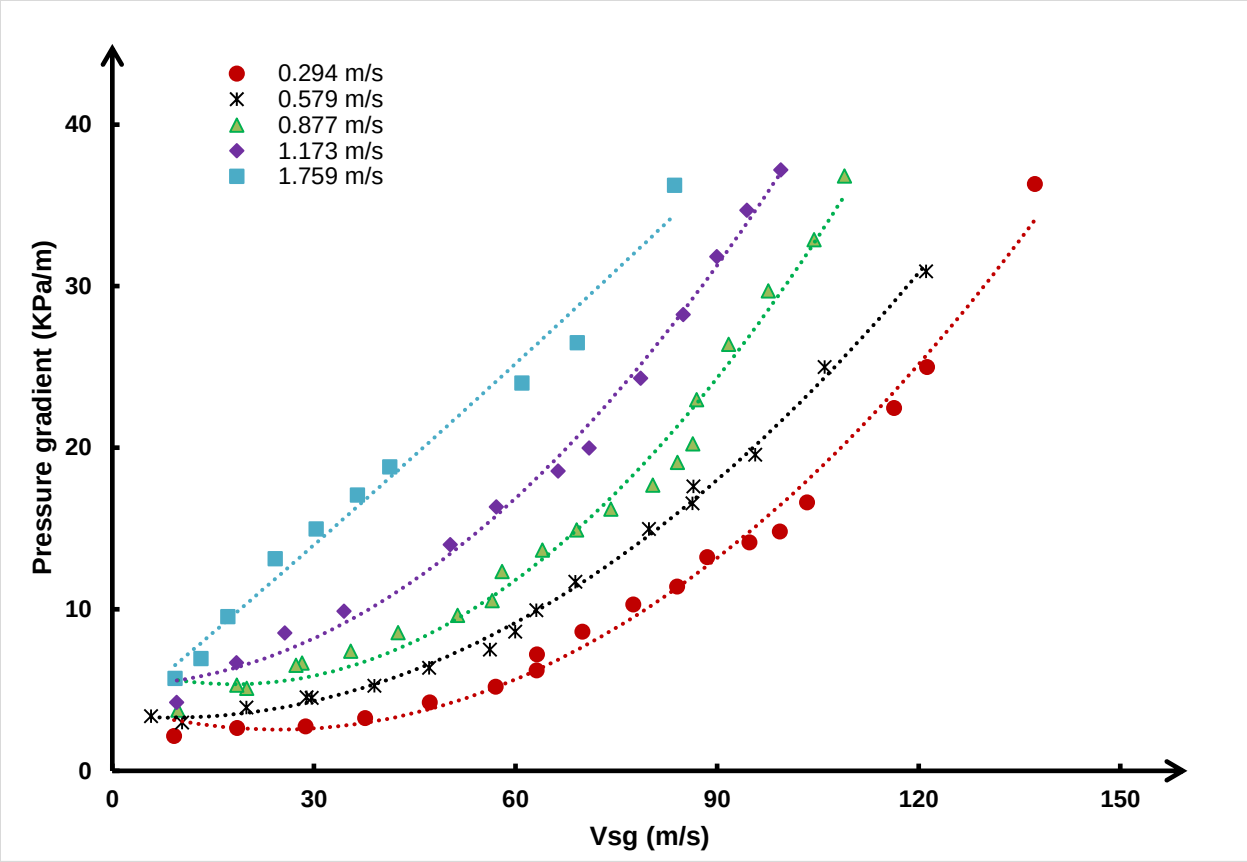

Figure 3.9 Pressure gradient measurements in the annulus

3.6.2 Multiphase flow in the pipe

3.6.2.1 Pressure measurement validation

It is essential to ensure the accuracy and validity of any data acquired during the experiments. In this study, single phase experiments were first carried out to calibrate and validate the measurements from the instruments used in the setup. The experiments included the circulation of water at ambient temperature with flow rates ranging from 40 to 100 gpm. The pressure drop measurements were obtained from the differential pressure transducers. The distance between the two pressure ports (DP_1 and DP_2) was 0.38 m. As a result, pressure drop measurements were very small and inaccurate. The distance between the pressure ports of L1 is 5 m, and the measurements (Figure 3.10) were significant. The results demonstrate an anticipated pressure drop behavior of

flow in pipe and annulus under turbulent flow conditions. To validate the accuracy of the measurements, measured pressure losses are compared with the ones calculated from Equation 3.7. The comparison shows a reasonable match with some discrepancies. Measurements are higher (15 to 30%) than prediction due to entrance effects, pipe roughness and other irregularities, which tend to increase pressure losses.

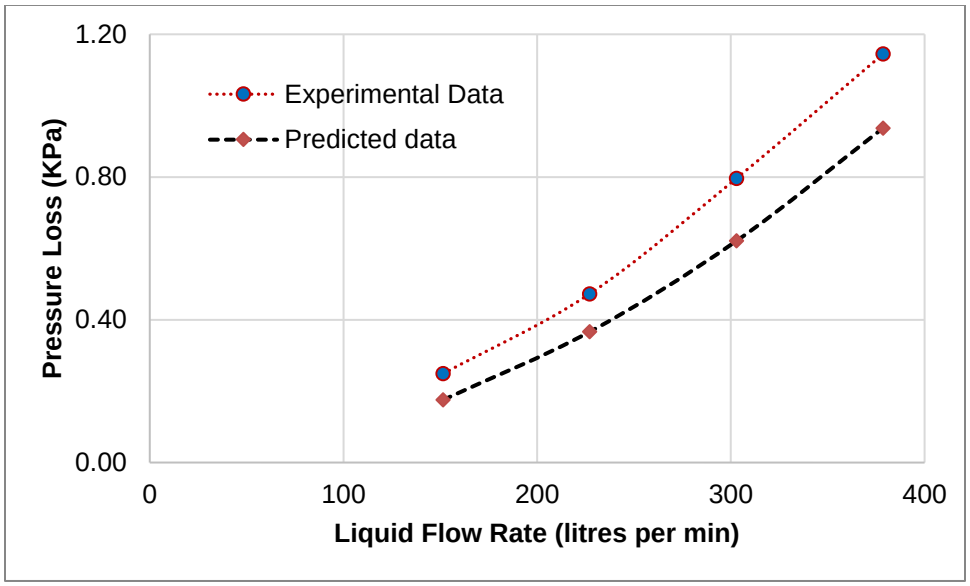

Figure 3.10 Measured and predicted pressure drop for single-phase flow in the pipe

Pressure loss (ΔP) in the vertical pipe can be deduced in terms of diameter (D), length (L), fluid density (ρ), and mean fluid velocity (V) as shown below:

$$\Delta P = f\frac{2L}{D}\rho V^2 \tag{3.7}$$

where f is the fanning friction factor. In this analysis, L is the distance between pressure transducer ports. The friction factor used in the calculation of pressure loss is expressed as (Chen, 1979):

$$\frac{1}{\sqrt{f_D}} = -2.0\ log\left[\frac{\varepsilon}{3.7065D} - log\left(\frac{1}{2.8257}\left(\frac{\varepsilon}{D}\right)^{1.1098} + \frac{5.8506}{R_e^{0.8981}}\right)\right] \tag{3.8}$$

where f_D is the Darcy friction factor, which is defined as fourfold of the Fanning friction factor. ε is the pipe roughness, and R_e is the Reynolds number. Table 3.6 depicts the comparison between the measured and predicted pressure losses.

Table 3.6 Measured and predicted pressure loss in pipe

Liquid Flowrate (GPM)	Superficial Liquid Velocity V_{sl} (m/s)	Experimental Pressure Gradient (Pa)	Predicted Pressure Gradient (Pa)	Error (%)
40	0.47	248.84	161.51	35.09
60	0.7	472.80	324.24	31.42
80	0.93	796.29	534.76	32.84
100	1.17	1144.66	802.74	29.87

3.6.2.2 Liquid Holdup Validation

Another important validation for flow in the pipe is based on liquid holdup that significantly affects the pressure drop. In this study, the liquid holdup data is validated by collecting the trapped water in the test section and comparing the resulting with the data collected from differential pressure transducer installed at the bottom of the test section as depicted in Figure 3.3. The volumetric liquid holdup based on the drained liquid from the test section can be expressed as:

$$H_L = \frac{V_L}{V_T} \tag{3.9}$$

where H_L is the liquid holdup, V_L is the liquid volume, V_T is the total volume of the test section. The liquid holdup based on the differential pressure transducer measurement can be calculated by the following equation:

$$H_L = \frac{\left({}^{P_{wf}}/_{\rho_l g}\right)_A}{(H_T A)} = \frac{\mathrm{P_{wf}}}{\mathrm{\rho_l g H_T}} \tag{3.10}$$

where P_{wf} is the bottom-hole pressure, A is the cross-section area of the test section, ρ_l represents liquid density, g is the gravitational acceleration, and H_T is the total height of the test section. The

comparison of the liquid holdup by the above mentioned methods are shown in Table 3.7. Results suggest that the difference between the two holdups are within 1% which can be attributed to the limitation of DP cell measurements.

Table 3.7 Comparison between the estimated and measured liquid holdup

Liquid Flowrate (GPM)	Gas Flowrate (lb/min)	Liquid Holdup (DP Cell) %	Liquid Holdup (from water collected) %	Error %
35	25	7	8.0	1.0
40	10	14	12.9	1.1

3.6.2.3 Flow Regimes

One of the important aspects of the multiphase flow in pipes is based on flow regimes. The flow regimes provide an idea about the movement of distinct phases. There are several parameters such as superficial velocity, diameter, and fluid properties which leads to different types of flow regimes. In the vertical pipe flow, the encountered flow regimes mainly include bubble, dispersed bubble, slug, churn, and annular. In the current experimental work, the main flow regimes encountered were slug, churn, and annular. As described earlier, it is difficult to distinguish between churn and slug flow regimes based on visual observations. Figures 3.18a and 3.18b show the slug/churn and annular flow regimes identified during the experiment. The slug/churn flow regime is mainly chaotic in nature, while the annular flow was streamlined.

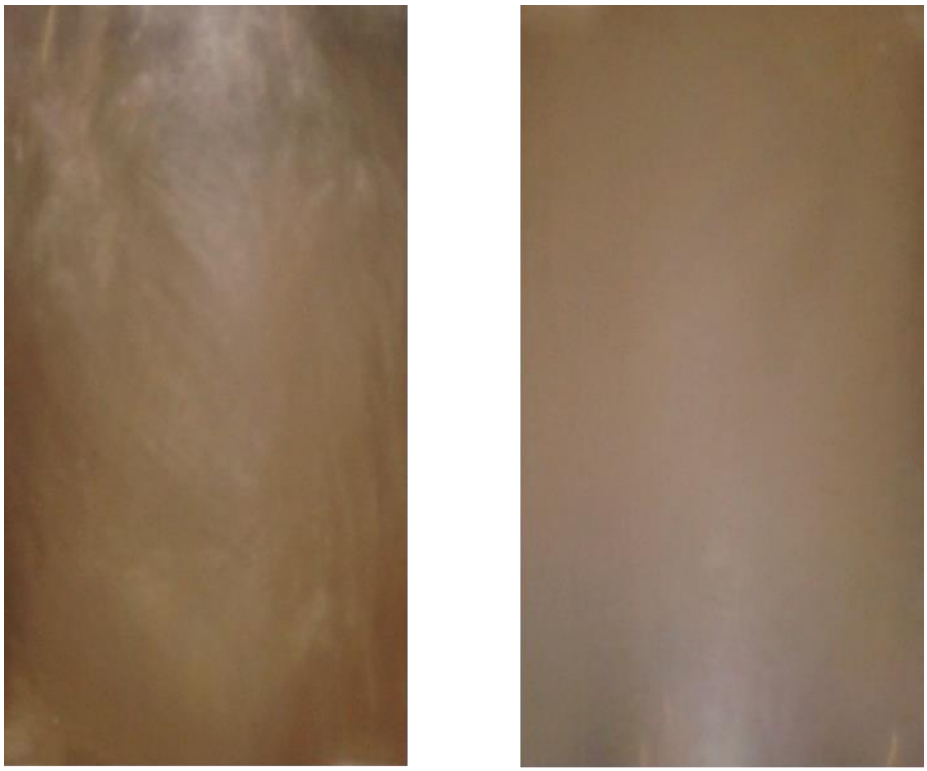

Figure 3.11 Visual images of flow regimes in the pipe (a) churn and (b) annulus

The oscillating nature of gas-liquid frothy mixture at a moderate superficial gas velocity in the viewport revealed the slug/churn flow pattern. In such flow pattern, there was no visual evidence for the gas core. However, as the superficial gas velocity is increased, the annular flow pattern is observed. The annular flow pattern included a gas core and liquid films on the wall. Furthermore, the increase in the superficial gas velocity destroys the liquid film on the wall, and the flow becomes mainly gas dominated. Apart from the flow regime characterization based on visual observation, the superficial gas and liquid velocity were superimposed on the flow pattern map as depicted in Figure 3.19. The flow pattern map is constructed based on the mechanistic model proposed by Tengesdal et al. (1999). The flow pattern map reveals that the slug/churn flow has close boundaries in the realm of higher superficial liquid velocity (> 0.3 m/s).

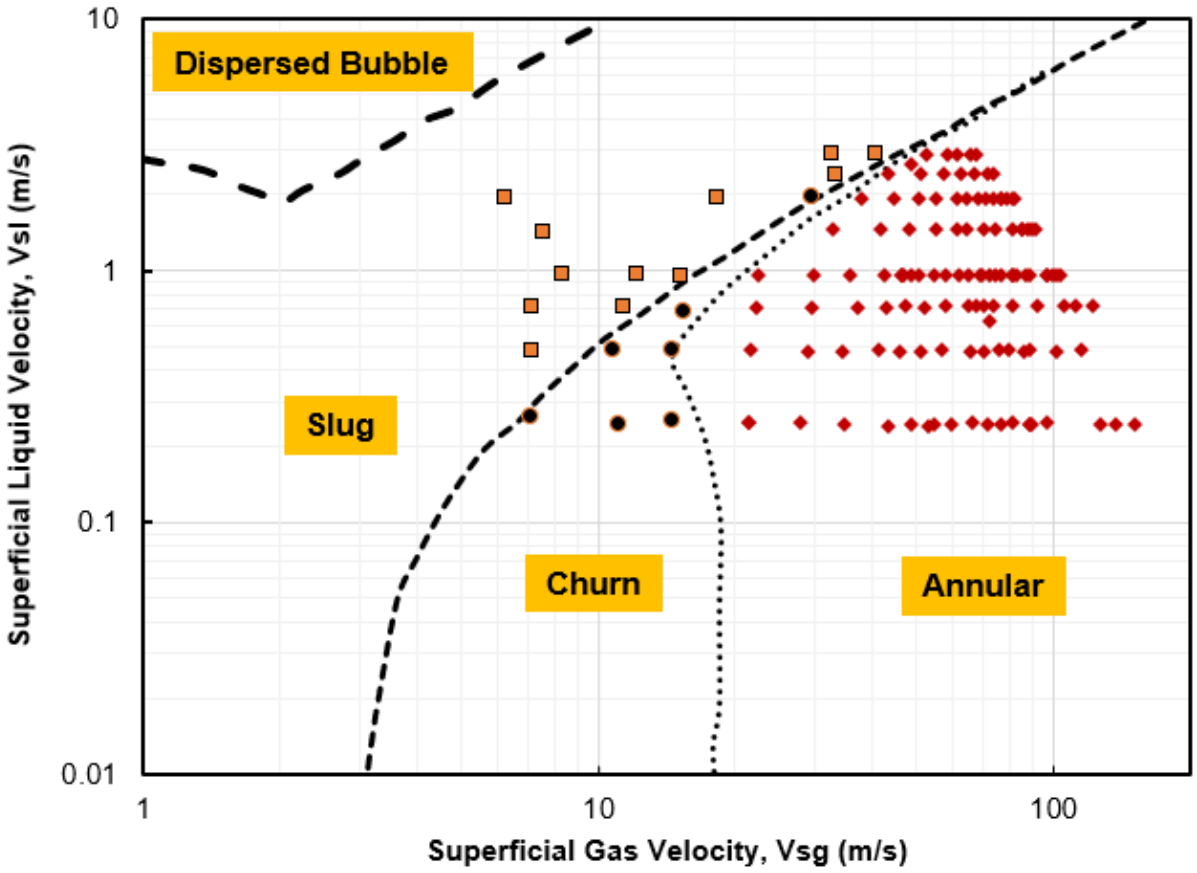

Figure 3.12 Flow regime map of two-phase pipe flows

3.6.2.4 Liquid Holdup

Closing valve technique was used to measure the liquid holdup in the pipe also as explained in section 3.6.1.3. Figure 3.20 depicts the liquid holdup corresponding to five liquid flow rates (76, 151, 227, 303, and 454 liters per minute). The liquid holdup decreases asymptotically with the increase in the superficial gas velocity. In addition, there is a slight increase in the liquid holdup with an increase in superficial liquid velocity. Similar trends have also been observed in several studies (Waltrich et al., 2015).

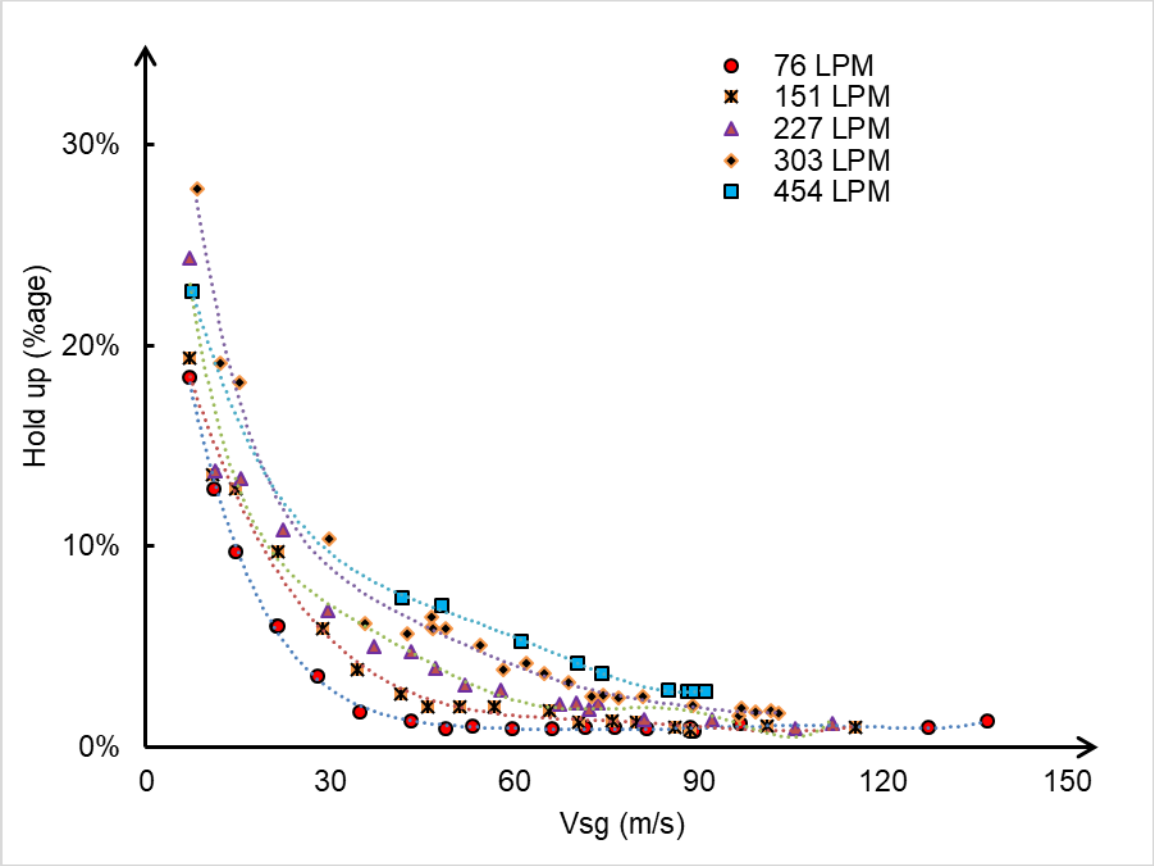

Figure 3.13 Liquid holdup measurements in pipe

3.6.2.5 Pressure Gradient

The pressure gradients are the main parameter to capture during the multiphase flow experiments. A systematic experimental program was designed in which for each set of experiments, the liquid flow rate was kept constant and the gas flow rate was varied. The idea behind adopting this strategy was to capture any trend with respect to change in the superficial gas and liquid velocities. The current experiments included a high gas flow rate. At the higher gas flow rate, the compressibility of gas cannot be ignored. Several temperature and pressure sensors were installed in the test section to capture its profile. There was a huge deviation in the pressure profile in the test section (An example is presented in Figure 3.14). Hence, the local density of air in the vicinity of the differential pressure sensor is implemented in gas velocity calculation. The local density was calculated using the ideal gas law based on local temperature and pressure.

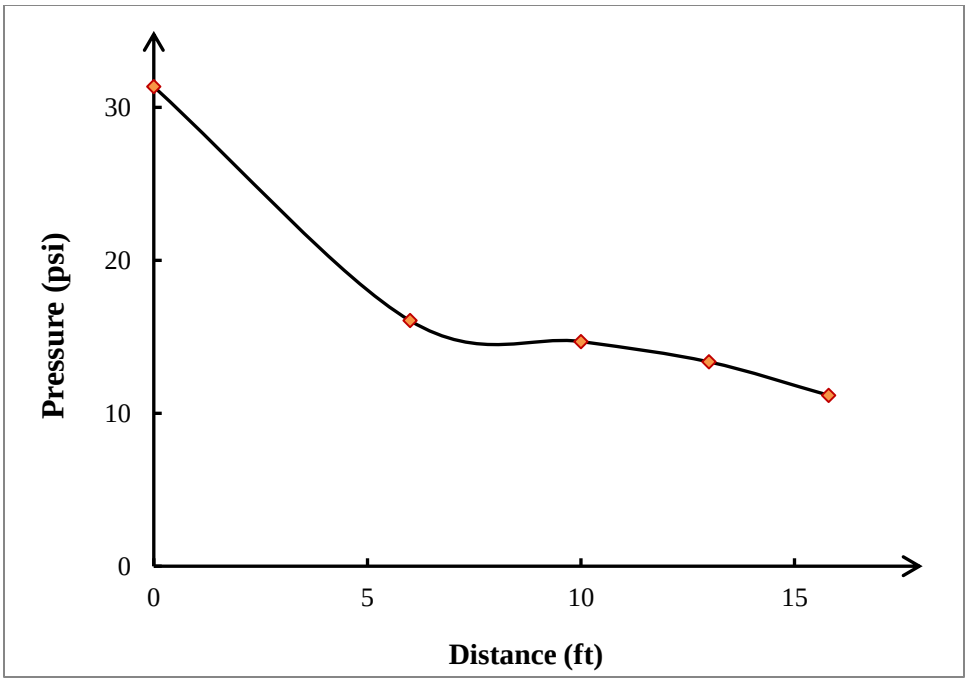

Figure 3.14 Pressure profile in whole pipe test section (Vsl: 0.24 m/s and Vsg: 127.4 m/s)

The pressure gradient results are depicted in Figure 3.15. It can be inferred that the pressure gradient increases with increase in the superficial gas and liquid velocity. This trend is opposite to the conventional trend of the pressure gradient measurement at low superficial gas and liquid velocity which is reported in previous studies (Waltrich et al., 2015; Ali, 2009). This change in trend can be attributed to different components in the pressure drop measurements. At low superficial gas velocities, the gravity component is the dominating factor in the pressure drop measurements while at the higher superficial gas velocities the friction component has a greater stake.

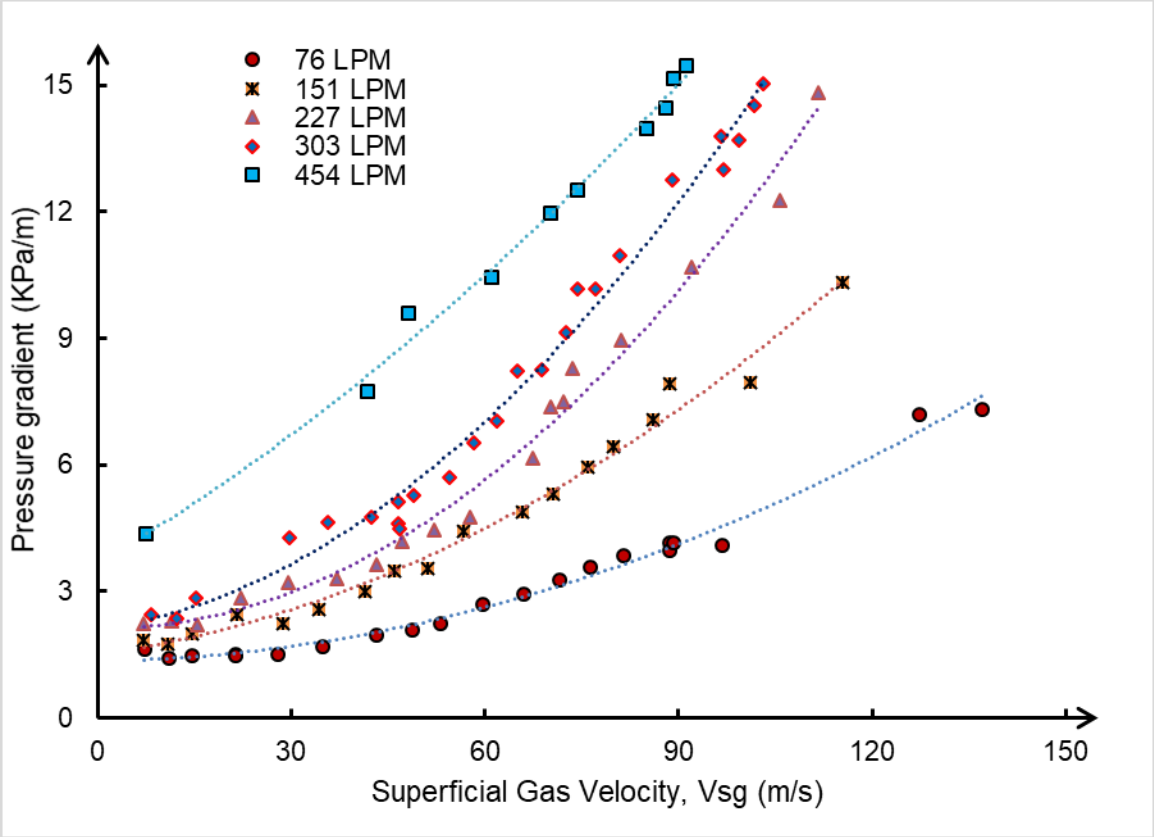

Figure 3.15 Pressure gradient measurements in pipe

3.6.2.6 High Mach Number Flows

The primary objective of this study is to conduct the experiments at high Mach number. There is limited study to depict the Mach numbers obtained in the current experimental conditions. However, Kieffer (1977) presented the plot for speed on sound in multiphase flow environment corresponding to the void fraction experiments. Hence, the superimposition of the current experiments can reveal the establishment of high Mach number flow during the test. Figure 3.16 presents the combined results from Kieffer (1977) and the current study. Some of the data points from the current experimental data is in between the speed of sound for 1 bar and 10 bars. This can be treated as validation of experimental data in subsonic to sonic conditions in the test setup. However, further validation is established based on the profile of the pressure measurement plot.

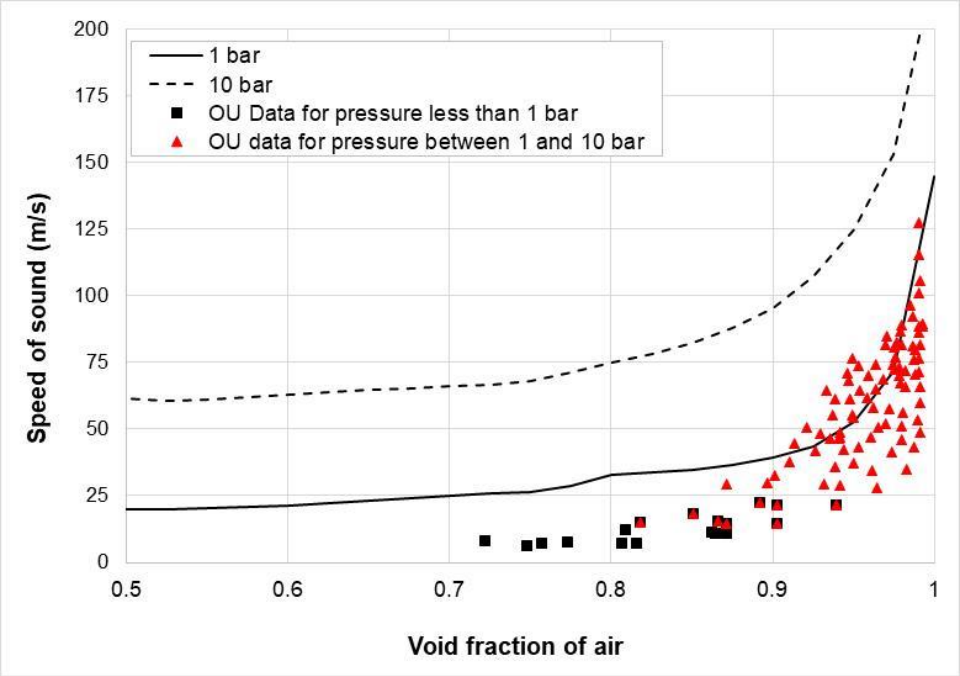

Figure 3.16 High velocity data superimposed on two-phase flow sonic speed (Kieffer, 1977)

Figure 3.17 shows the pressure drop profile of different liquid flow rates corresponding to the increase in the superficial gas velocity. It can be inferred that the pressure drops increases with increase in the superficial gas velocity in the initial stage of the change. However, the pressure drop measurement reaches a peak, and then it suddenly starts decreasing. This can be attributed to the established sonic boundary in the experiments as depicted in Figure 3.17.

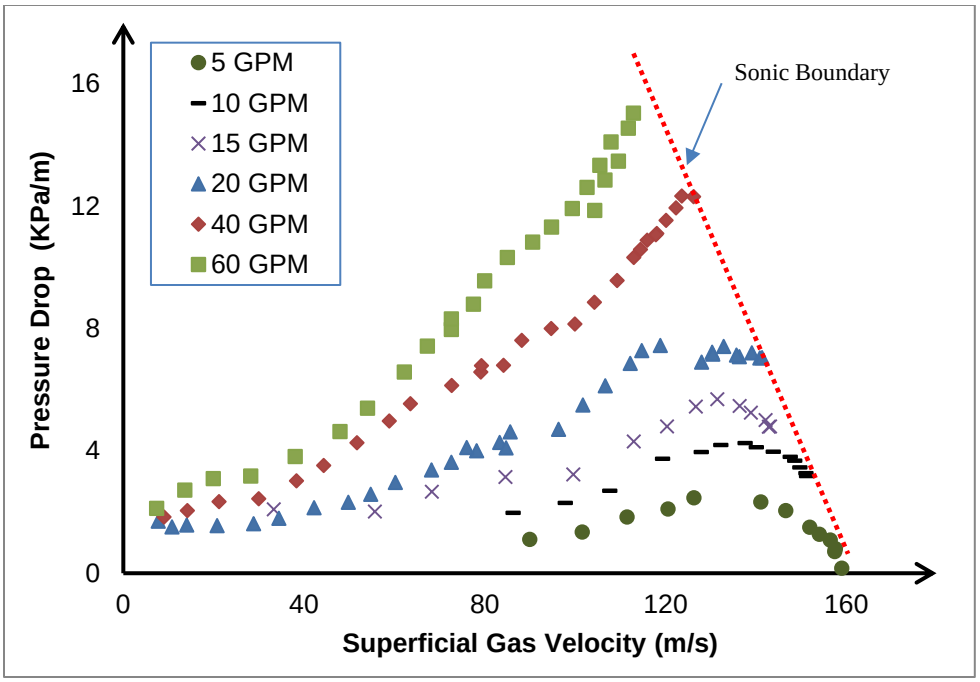

Figure 3.17 Pressure drop vs. superficial gas velocity in pipe at low liquid rates

Another validation for the establishment of the sonic condition is based on the choking phenomenon in the test section. The choking phenomenon in the fluid flow can be characterized based on in-situ decoupling of fluid velocity and upstream pressure in which the fluid velocity becomes independent of change in upstream pressure. Figure 3.18 represents the upstream pressure corresponding to an increase in the superficial gas velocity. It can be inferred from the figure that at low liquid flow rates (19, 38, and 76 LPM), the measured upstream pressure does not affect the superficial gas velocity. This decoupling of superficial gas velocity with upstream pressure can be attributed to the change in the density of the pressure.

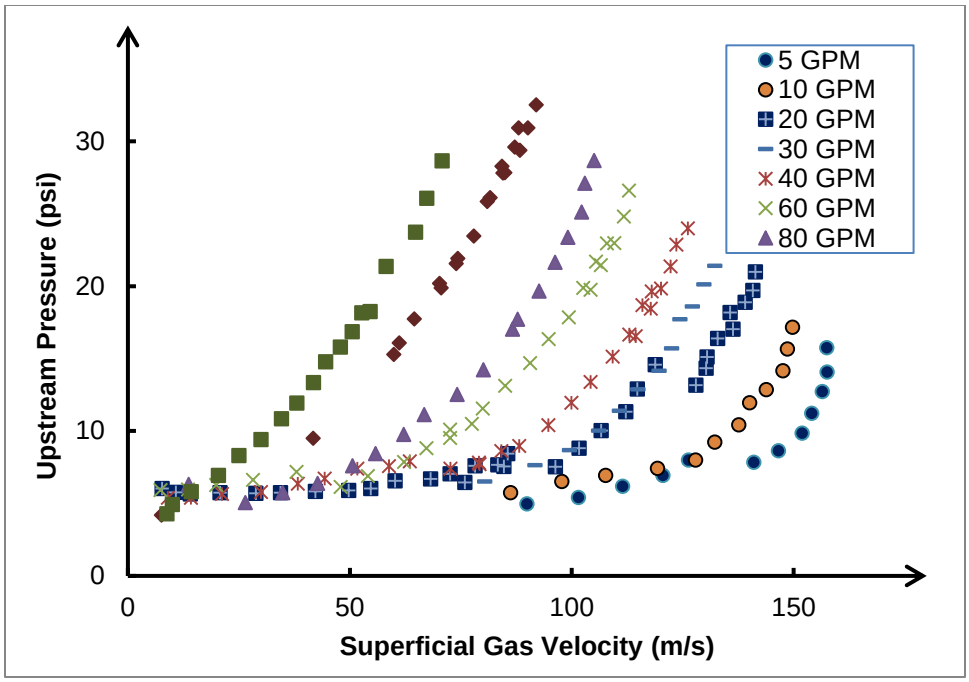

Figure 3.18 Upstream pressure versus superficial gas velocity

3.7 Chapter Summary

The main objective of the experimental investigation is to obtain the flow parameters which can be used to validate and verify the hydrodynamic models used in worst-case discharge (WCD) estimation. The test setup included pipe and annulus type of geometry as is the case encountered during the oil and gas operations. During the experiments, the main parameters captured were pressure drop, liquid holdup, and flow patterns data corresponding to high-velocity two-phase flow.

First, the experimental are validated using the available theoretical models and experimental data available in the public domain. The pressure gradient for two-phase flow in the annulus and pipe shows an increasing trend with respect to the superficial gas and liquid velocities. This observation is contrary to the low-velocity two-phase flow experiments mainly reported in past studies. This difference can be attributed to the friction dominated flow regime instead of gravity dominated

regime corresponding to low superficial gas velocities. In addition, the liquid holdup profile is consistent with past studies. Apart from the usual flow parameters, the sonic conditions were established for flow in the pipe. The evidence for the sonic conditions included the constant upstream pressure with an increase in gas flow rate. Other evidences are presented in detail in the above section. Furthermore, an extensive flow pattern map for annulus and pipe is developed. Different theoretical and experimental boundaries for the flow regime transitions were identified and presented.

Chapter 4: CFD Modeling

4.1 Overview

Computational fluid dynamics, though a computationally intensive and sophisticated area of research, but still one of the most commonly used methods for understanding and analyzing the flow characteristics in complex geometries. Advances in CFD motivate the research in this area and is the main motivation for this study. The scope of this study is only limited to the characterization of the flow in the annulus.

Past modeling works for vertical flow in the wellbore of oil and gas wells has mostly been focused on pipe flow. Studies on annular flow have been mainly focused on experimental work and analytical/mechanistic modeling. Also, past experiments were limited to the low-velocity range (less than 22 m/s) mainly due to experimental complexities (i.e., challenges in maintaining constant gas and liquid rates during experiments, controlling gas expansion, and preventing extreme water hammering effects occurring during gas and liquid rate manipulation). The use of low-velocity experiments and simplistic modeling efforts are good for building up the understanding and establish applicable models for low-speed flows. However, in this modern age of advanced control systems and the tremendous increase in computational powers, it is possible to perform high-velocity experiments and CFD modeling. The use of CFD provides a better understanding of two-phase flow characteristics. In the pursuit of exploring the distinctions of flow in the annulus, a comprehensive effort has been made in this study. We started with the theoretical background of CFD modeling and then simulated experimental conditions. The principal objective of this paper is to analyze and investigate the multiphase flow features in the annulus. The following steps were taken to accomplish the objective systematically:

- CFD modeling encompassed the simulation of multiphase flow in the annulus, and a comprehensive effort has been made to understand the flow dynamics using the numerical results.
- For the CFD simulation, a sensitivity analysis was performed to determine the effect of mesh size and grid structure on CFD results and minimize numerical errors. The detail of this analysis is presented in Section 4.2.3.
- The flow characteristics resolution presents a unique challenge for simulation which needs a different strategy to mimic the flow features such as pressure drop, flow pattern, and void fraction. Segregated inlet mechanism can imitate the real-time flow properties as discussed in Section 3.
- A computational approach using probability density function was implemented to study flow pattern and compare the flow regimes detected by visual observations and mechanistic models. The difference between high and low gas velocity flow structures is also investigated and presented in Section 4.2.4.
- The turbulence characteristics of two-phase flow in the annulus are strongly associated with the superficial gas and liquid velocities. Section 4.2.4 describes the details of turbulent characteristics.

4.2 Model for Flow in Annulus

The flow in the annulus is one of the highly discussed areas of multiphase flows considered in drilling operations. Most of the time, the drill pipe is present in the annulus while drilling. This makes the presence of flow in annulus a likely scenario during the worst-case discharge. Therefore, the understanding of flow characteristics of two-phase flow in the annulus is of paramount importance. Keeping this in mind, simulation work was conducted for fluid flow in the annulus.

The study encompassed the construction of the geometry, meshing of the flow domain, setting up the theoretical model, and solving the model in ANSYS Fluent. The geometry of the model is constructed using the geometry module of ANSYS, and standard meshing option was used to obtain the desired grid structures. A sensitivity analysis was carried out to optimize the number of elements required for the simulation. After obtaining the optimum grid distribution system, several modeling options, such as Volume of Fluid and Eulerian, were tried to replicate the experimental results. Ultimately the most suited theoretical models and parameters were chosen to simulate the flow behavior in the annulus.

4.2.1 Computational Domain

The geometry considered in the CFD study (Figure 3a) included a long vertical pipe of length more than 40 times the hydraulic diameter ($L > 40D_h$). The inner diameter of the outer pipe was 83 mm, and the outer diameter of the inner pipe was 35 mm. In the actual experimental condition, the test section had a length of 5.48 m. The shorter length was considered in the CFD analysis to reduce the computational effort. Past studies (Lien et al., 2004; Laufer, 1952; and Nikuradse, 1933) suggest that the flow is fully developed in the axial direction after the entrance length of 30 to 40 times the hydraulic diameter. Therefore, 2 m is considered to be sufficient to simulate the experimental condition. Moreover, at a specific cross-section, which was 0.5 m before the outlet, the time-series of area average void fraction was recorded in the simulation data. The specific cross-sectional plane was chosen to avoid the impacts of both the entrance and exit regions on the results and provide enough entrance length to establish a fully developed flow condition.

4.2.2 Numerical Schemes and Boundary Conditions

The current study includes ten simulation cases as reported in Table 4.1. In the experimental investigation, the liquid flow rate was kept constant, and the gas flow rate was varied. The motive behind this design of experiment was to capture the intricacies of the flow features with increasing gas velocity. To replicate similar experimental conditions and get further insight of flow dynamics, the volume of fluid (VOF) method of CFD was chosen to track the interface between the phases using ANSYS Fluent (Hirt and Nichols, 1981). The VOF model showed good numerical stability, better convergence, and reasonable accuracy when compared with experimental measurements. The continuum surface force model was adopted for surface tension modeling which enables accurate modeling without restrictions on the dynamic evolution of interfaces (Brackbill et al., 1991). Considering high superficial gas velocities, the air is chosen as the primary phase and water as the secondary phase. As the effect of temperature was neglected; hence, the energy equation was not considered in the simulation. The implicit body force was enacted in the model to satisfy the equilibrium condition between body force and pressure gradient terms of the momentum equation, which also handles the convergence issues in case of partial equilibrium.

Table 4.1 Liquid flow rate and superficial liquid velocity variation

Case	Superficial Gas velocity	Superficial Liquid velocity	Pressure Gradient	Liquid Holdup (H_l)
	m/s	m/s	Pa/m	
1	9.181	0.296	2164	0.202
2	18.55	0.302	2645	0.103
3	28.75	0.300	2761	0.040
4	37.64	0.295	3258	0.031
5	47.24	0.293	4241	0.029
6	10.39	0.576	2986	0.172
7	19.97	0.575	3916	0.107
8	28.92	0.575	4545	0.083
9	39.01	0.576	5276	0.038
10	47.15	0.579	6374	0.031

In the CFD analysis of two-phase flows, turbulence models are of critical importance. In this study, we used two turbulence modules available in ANSYS Fluent: (a) realizable k-ε and (b) Shear Stress Transport (SST) k-ω model. The k-ε turbulence model contains two transport equations, and it often has three types of formulations: (a) standard, (b) re-normalization group (RNG), and (c) realizable. These three formulations have similar forms in terms of transport equations. However, they differ from each other in terms of calculation methodology for turbulent viscosity, Prandtl numbers, and evolution terms in dissipation rate equation (Fluent 2016b). The realizable turbulence model for the k-ε model is the improved version of other turbulence models (Standard and Re-Normalization Group) for certain kind of flows such as complex shear flow, boundary layer separation. Similarly, there are also three formulations in k-ω turbulence model: (a) standard, (b) shear stress transport model (SST), and (c) Reynold stress model (RSM). The SST model has two hybrid equations developed by combining the advantages of k-ε and other k-ω models (Fluent, 2016b). The k-ε realizable and k-ω models have been used in a number of studies (Parsi et al., 2016; De Sampaio et al., 2008; Berthelsen and Ytrehus, 2005) for modeling two-phase pipe flows. However, Wilcox (1993) suggested that the k-ε models are ill-behaved and inconsistent with the turbulent boundary layer physical structures. Rui and Xing (2011) used the k-ω turbulence model to simulate the supersonic cross-flow with evaporating water droplets. The SST k-ω turbulence model produces a large turbulence level with strong acceleration; and hence, it is well-suited for high-velocity flow (Menter, 1994). In this study, simulations were performed using both models (realizable k-ε and SST k-ω models). The boundary layer characteristics were also compared for annular flow regime for the first set. It has been seen that the SST k-ω turbulence model is better suited at higher gas velocity for the annular flow geometry.

The annular flow geometry is symmetric with respect to X-X and Y-Y planes as depicted in Figure 4.1. Apart from that, experimental observation of asymmetric Taylor bubbles only applies in the slug flow regime which is not the scope of this study; hence, applying the symmetricity to reduce the computational effort doesn't affect the results. Therefore, only a quarter section of the annulus was considered for grid generation using standard mesh module of ANSYS to reduce the computational expenses. Results obtained from a full annulus and quarter section were found comparable and consistent with single phase flow measurements. To replicate more realistic conditions and achieve faster steady-state phase distribution, the inlet cross-section was divided into three inlet zones. The three inlets were assigned (Figure 4.1) with velocity-inlet boundary conditions (two of them in the vicinity of the peripheral boundary for water inlet, and one for a gas inlet in the core). Similar segregated inlet flow boundary conditions have also been successfully employed by pipe flow studies (Parsi et al., 2016; Lopez et al., 2016) in the past. This arrangement makes the simulation of the two-phase flow computationally faster and efficient.

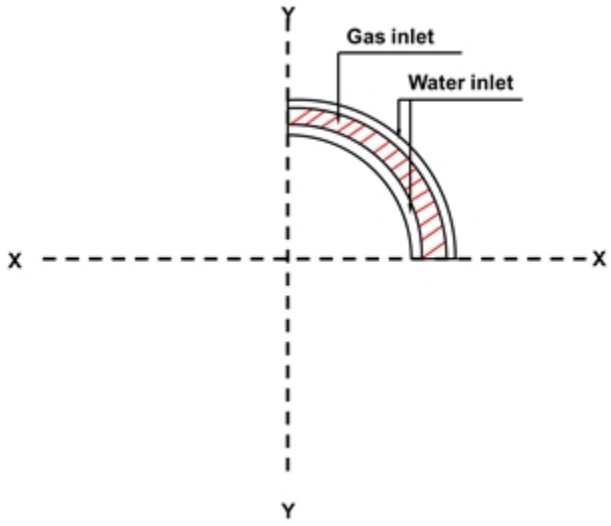

Figure 4.1 Inlet boundary condition for the CFD model (Not to scale)

The inlet velocity was calculated based on the area of the inlet zone. For instance, the velocity of the gas in the middle inlet zone was calculated using the following equation:

$$V_{sgin} = V_{sg} \frac{A_{total}}{A_g} \quad (4.1)$$

where V_{sgin} is the inlet gas velocity for the simulation model. V_{sg} is the experimental superficial gas velocity. A_g is a gas inlet area depicted in Figure 4.1. A_{total} is the total area of the inlet cross-section. It should be noted that the volume fraction of another phase for the particular inlet is considered to be zero for that particular inlet spatial domain. For instance, the velocity of the liquid phase is zero for the middle/core section (gas inlet) and vice-versa. The outer and inner walls were assigned as the stationary boundary with the no-slip condition. The pipe roughness height was considered to be 0.000015 m, while the roughness constant was taken as 0.5. The initial gauge pressure was assumed to 0 Pa with the flow in an axial direction. The turbulence was specified in terms of intensity and hydraulic diameter. The intensity was assumed to be 5%, while the hydraulic diameter was 47.6 mm in this case. In addition, both planes of symmetry were defined as symmetric boundary conditions in ANSYS Fluent. At the outlet, pressure boundary conditions were implemented. The outlet was open to atmosphere, and hence the pressure at the boundary was considered to be 0 Pa (gauge pressure).

A pressure-based solver was chosen from the options offered in the FLUENT package, where a finite volume methodology is used to discretize the governing equations. SIMPLE (Semi-Implicit Method for Pressure-Linked Equations) scheme was utilized for pressure-velocity coupling calculations. For the spatial discretization, different methods were used: (a) Least Square Cell-Based for gradient (b) Third order MUSCL (Monotone Upstream-Centered Schemes for Conservation Laws) for momentum, (c) QUICK (Quadratic Upstream Interpolation for Convective Kinematics) for volume fraction (d) second-order upwind for turbulence kinetic energy and turbulence dissipation rate. In addition, the first order implicit scheme was used for the transient formulation to reduce the computational efforts. It is important to note that the default

under-relaxation factors led to a divergence in the model during simulation. Hence, the under-relaxation factors were cut down to different values which are: (a) 0.3 for pressure; (b) 0.5 for body forces, momentum, and turbulent viscosity; (c) 0.6 for turbulence kinetic energy and turbulence dissipation rate; and (d) 1 for density.

4.2.3 Grid Distribution

The success of any CFD modeling study relies significantly on mesh characteristics. The closest geometry to the annulus is a circular pipe. Several studies are available in the literature regarding pipe flow. One of the main reasons for deviations in the flow characterization is the variation in mesh construction. Parsi et al. (2015) reported that the butterfly shape of mesh geometries is suitable for the two-phase flow simulation in pipes. Similar observations have been reported by other studies (Hernandez-Perez et al. 2011; Abdulkadir et al., 2015). However, grid sensitivity study has not been conducted for any modeling work in the annulus. In this investigation, before performing the main simulation study, the grid suitability was evaluated using the first experimental dataset. Three types of grids were generated as shown in Figure 4.2. The three types include (a) structured uniform, (b) structured non-uniform, and (c) unstructured.

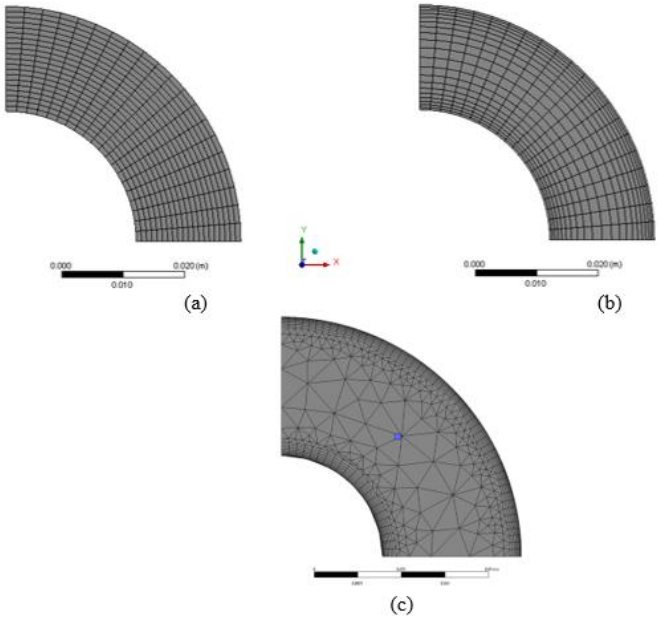

Figure 4.2 Grid distribution: (a) Uniform structured, (b) Non-uniform structured, and (c) Unstructured

The unstructured grid showed divergence; hence, such grid distribution system was discarded. A different number of grid elements were considered in the study as summarized in Table 4.2. Six sets of variations in grid sizes were considered to perform sensitivity analysis. Type 1 considers 600 elements (20 × 30) in the horizontal cross-section with 50 divisions in vertical direction. In this type of mesh, A and B are 20 and 30 divisions, respectively. A refer to divisions along the edges to the plane of symmetry and B stands for the number of divisions along the peripheral edge. Similarly, other types of meshes were also considered.

Table 4.2 Number of elements used in different grid structures

	Number of elements in cross-section (AXB)	Total number of elements	Grid Distribution System
Mesh 1	600 (20 × 30)	30000	Uniform
Mesh 2	900 (30 × 30)	45000	Uniform
Mesh 3	600 (20 × 30)	30000	Non-uniform
Mesh 4	900 (30 × 30)	45000	Non-uniform
Mesh 5	900 (30 × 30)	72000	Non-uniform
Mesh 6	1200 (40 × 30)	96000	Non-uniform

Different mesh types were tested for Case 1 (Vsg = 9.181m/s and Vsl = 0.296 m/s). Pressure drop measurements are summarized in Table 4.1. The discrepancies with respect to the pressure drop are shown in Figures 4.3 and 4.4. For the same number of grids, non-uniform grid distribution displayed a lower error than the uniform grids distribution (Figure 4.3). Therefore, non-uniform grid distribution was selected, and additional two simulations (Mesh 5 and 6) were performed to determine the optimal number of grids (Figure 4.4). For non-uniform grid distribution, discrepancies between measurements and simulation reduced with the number of mesh elements. The reduction stabilized as the number of grid element was increased. As a result, mesh structure Types 5 and 6 showed comparable errors (15%). Hence, to save the computational time, mesh Type 5 was used in all simulations except for the highest superficial gas velocity cases where mesh Type 6 was used.

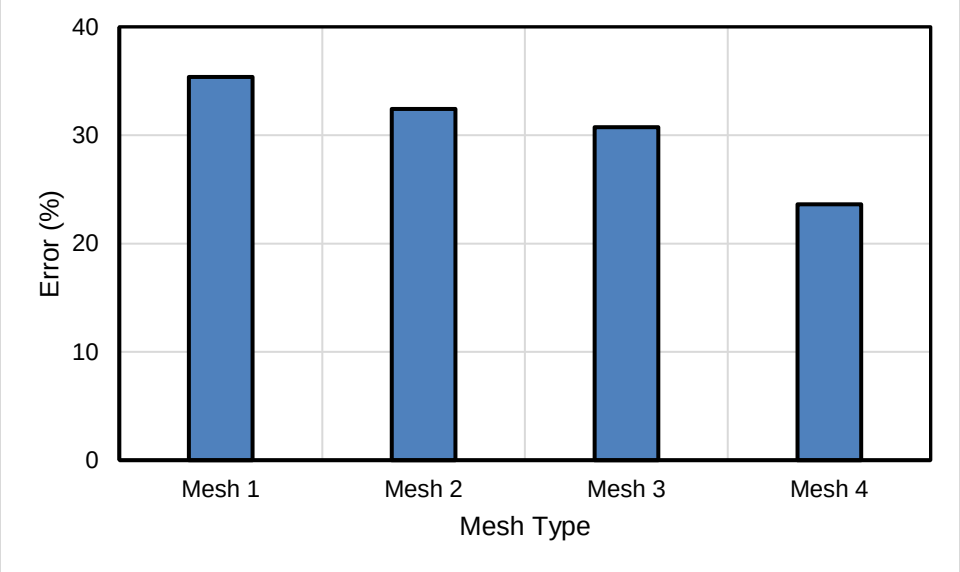

Figure 4.3 Mesh distribution vs. discrepancies between simulated and measured pressure drop for uniform and non-uniform structured grids

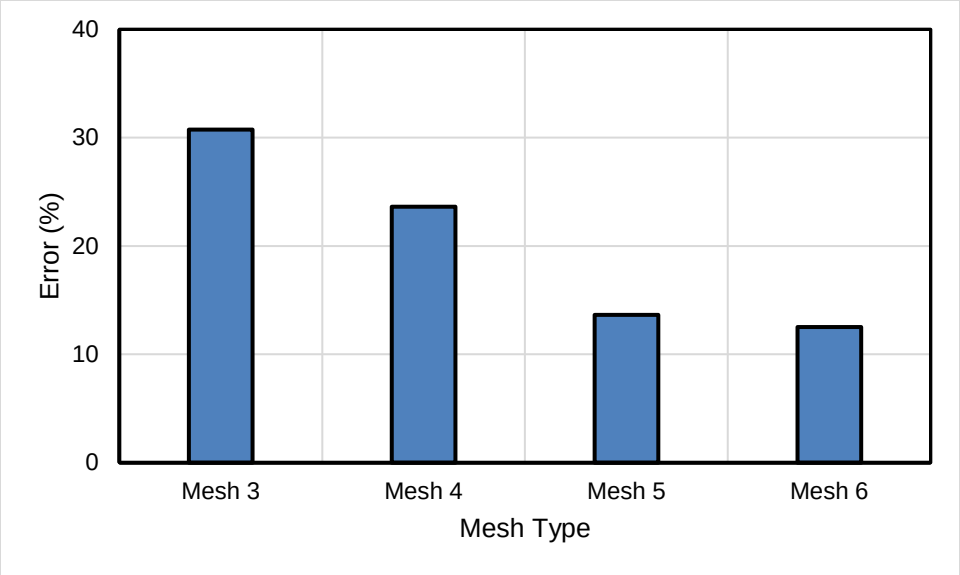

Figure 4.4 Mesh distribution vs. discrepancies between simulated and measured pressure drop for non-uniform structured grids

4.2.4 Results and Discussion

The standard initialization method was used to initialize inlet flow conditions. After the initialization, the whole flow domain was patched with the liquid phase. The time step was 0.001 s with 100 iterations allowed for each step to meet the convergence criteria. The standard convergence criterion of 0.001 was selected for residuals of continuity, velocity (u, v, w), kinetic energy (k) and dissipation rate (ε). Furthermore, several other parameters such as net mass flux, volumetric average pressure, void fraction, and turbulence kinetic energy were tracked with flow-time. The monitoring of these additional parameters was essential to ensure complete development of the flow in the relevant section. It was inferred that the volumetric average of pressure, water volume fraction, and turbulent kinetic energy stabilizes and attains approximately constant value in case of fully developed flow (shown in Figures 4.5, 4.6 and 4.7). The value of volumetric average pressure stabilizes to a constant value after 0.5 seconds of the simulation time which signifies the establishment of fully developed flow in the system for the second case. In addition,

the time-series value of void fraction was used in generating the probability density function for flow identification as described in Section 3.6.

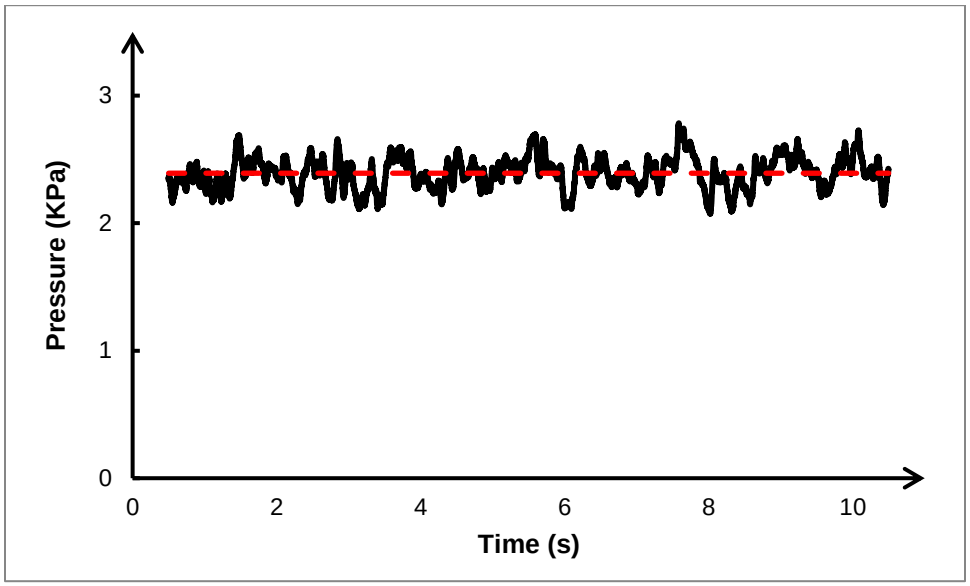

Figure 4.5 Simulated volumetric average pressure (at 1.5 m from the inlet) in the annulus with time

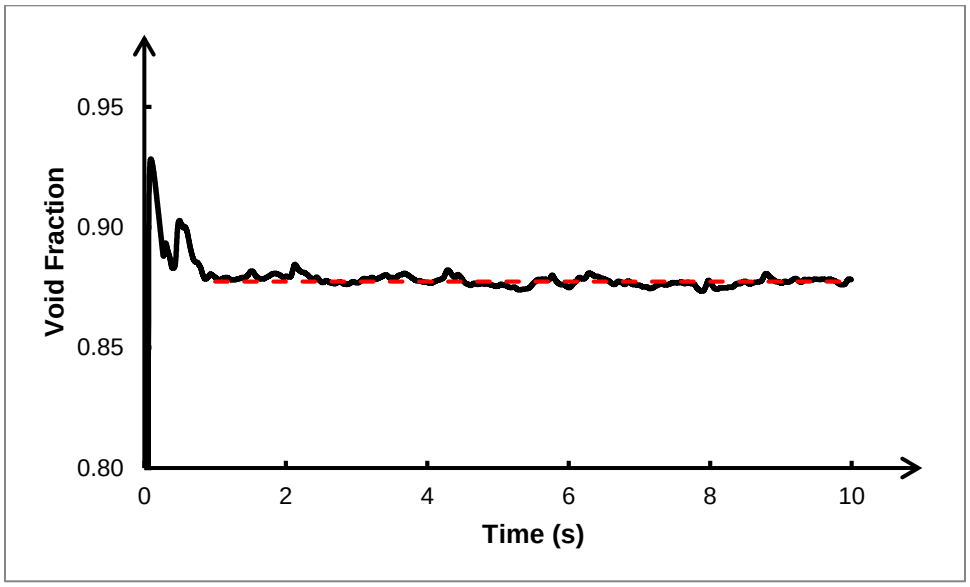

Figure 4.6 Simulated volumetric void fraction (at 1.5 m from the inlet) in the annulus with time

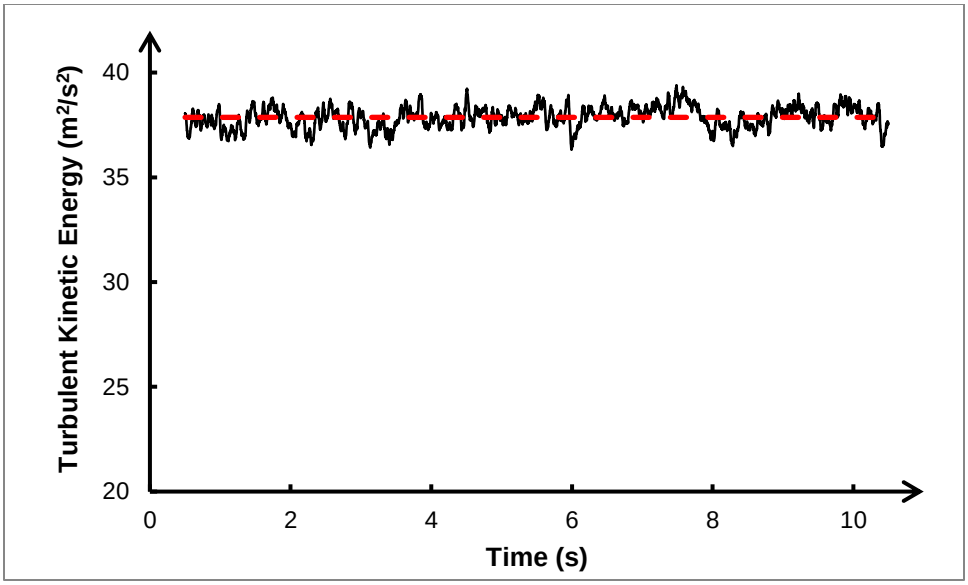

Figure 4.7 Simulated turbulent kinetic energy (at 1.5 m from the inlet) in the annulus with time

The CFD simulation results for all ten cases as described in experimental results are presented in Figures 4.8 and 4.9. It is worth mentioning that the CFD simulated pressure gradients are lower than the experimental data at comparatively lower superficial gas velocities (less than 19 m/s) and higher at velocities greater than 28.75 m/s. The pressure gradient predictions from stress transport (SST) k-ω model and realizable k-ε model were similar. It was also observed with increase in the slippage between both phases, the error in pressure drop calculation increases especially in case of higher superficial liquid velocity. Similar observations have been reported for the volume of fluid (VOF) modeling in other studies (Parsi et al., 2015; Asheim, 1986; Waltrich et al., 2015).

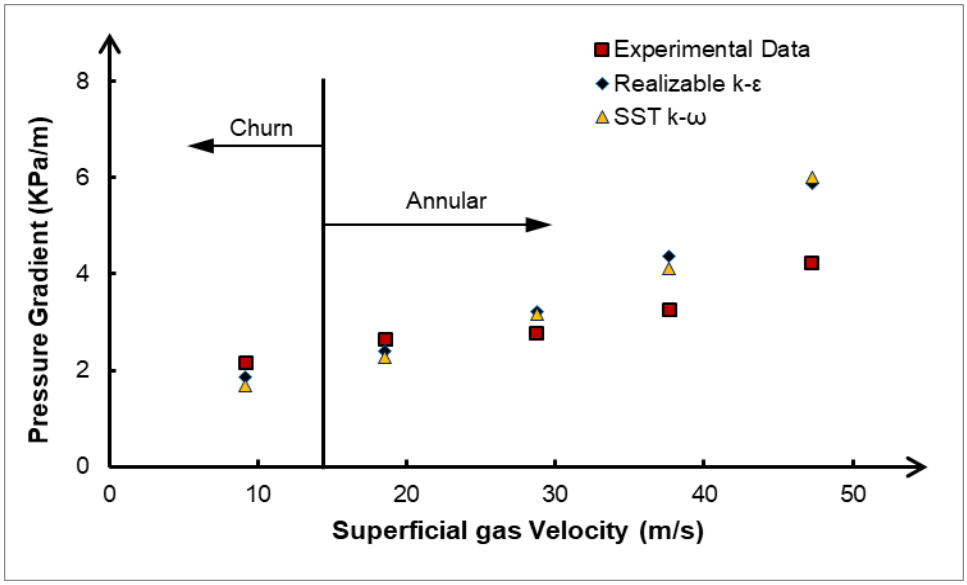

Figure 4.8 Measured and predicted pressure gradients for liquid flow rate of 77.5 LPM

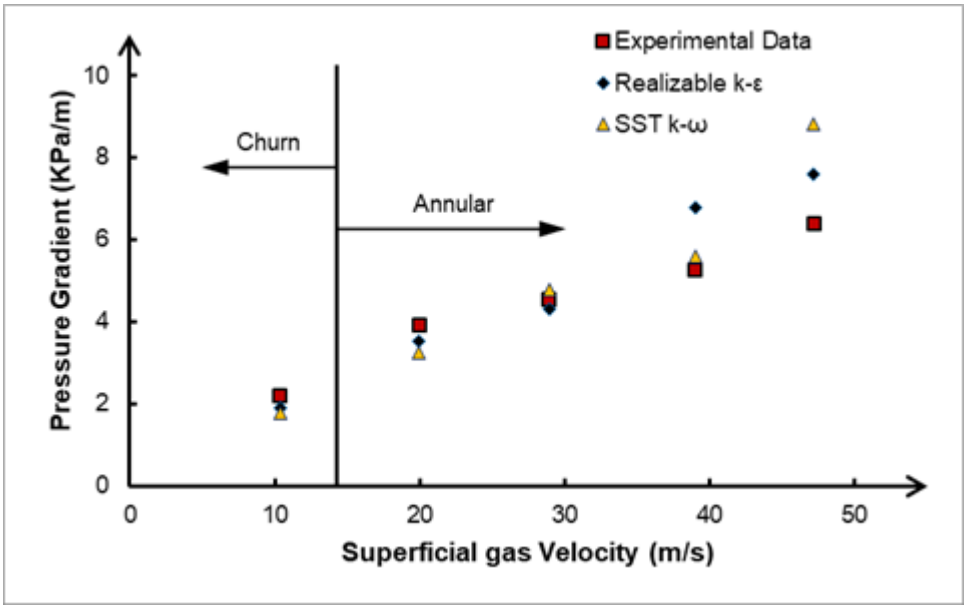

Figure 4.9 Measured and predicted pressure gradients at a liquid flow rate of 155 LPM

Apart from the pressure gradient, the void fraction is an important characteristic in multiphase flow simulation. The spatial distribution varies from one flow regime to other as shown in Figure 3.7. In this study, the flow regime area is based on high superficial gas velocity, where churn and annular flow regimes become dominant. The annular flow regime is characterized by the formation

of a thin film on the boundary walls and gas core in the middle part of the annulus. There are several methods to characterize flow regimes. One of the common visualization techniques is looking at the flow structure. As depicted in Figure 4.10, the zero-void fraction near the wall can be treated as a film.

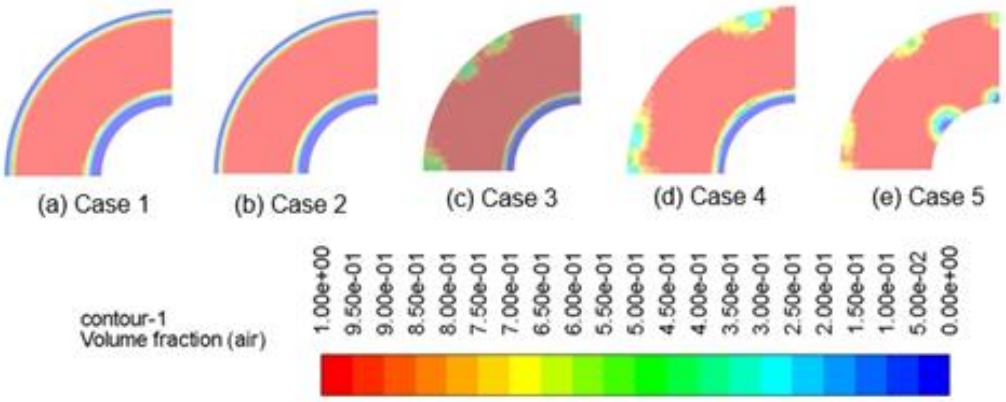

Figure 4.10 Void fraction distribution in the cross-sectional plane located at 1.5 m axial distances from the inlet point for the first five cases as mentioned in Table 4.1

To quantify the distribution of void, the area-weighted average of void fraction distribution was captured for the horizontal cross-sectional plane at an axial distance of 1.5 m from the inlet point. The profile of void fraction for the annular flow regime with the distance along the radial direction is depicted in Figure 4.11. The void fraction is negligible closer to the wall, while it is maximum in the core of the annulus corresponding to superficial gas velocity from Case 1, 2, and 3. However, with an increase in the gas velocity, the void fraction in the film region also increases. Similar observations have been made experimentally for a void fraction of pipe flow using wire mesh sensor (Parsi et al., 2015). Also, the videos captured during the experiment investigation showed a similar pattern.

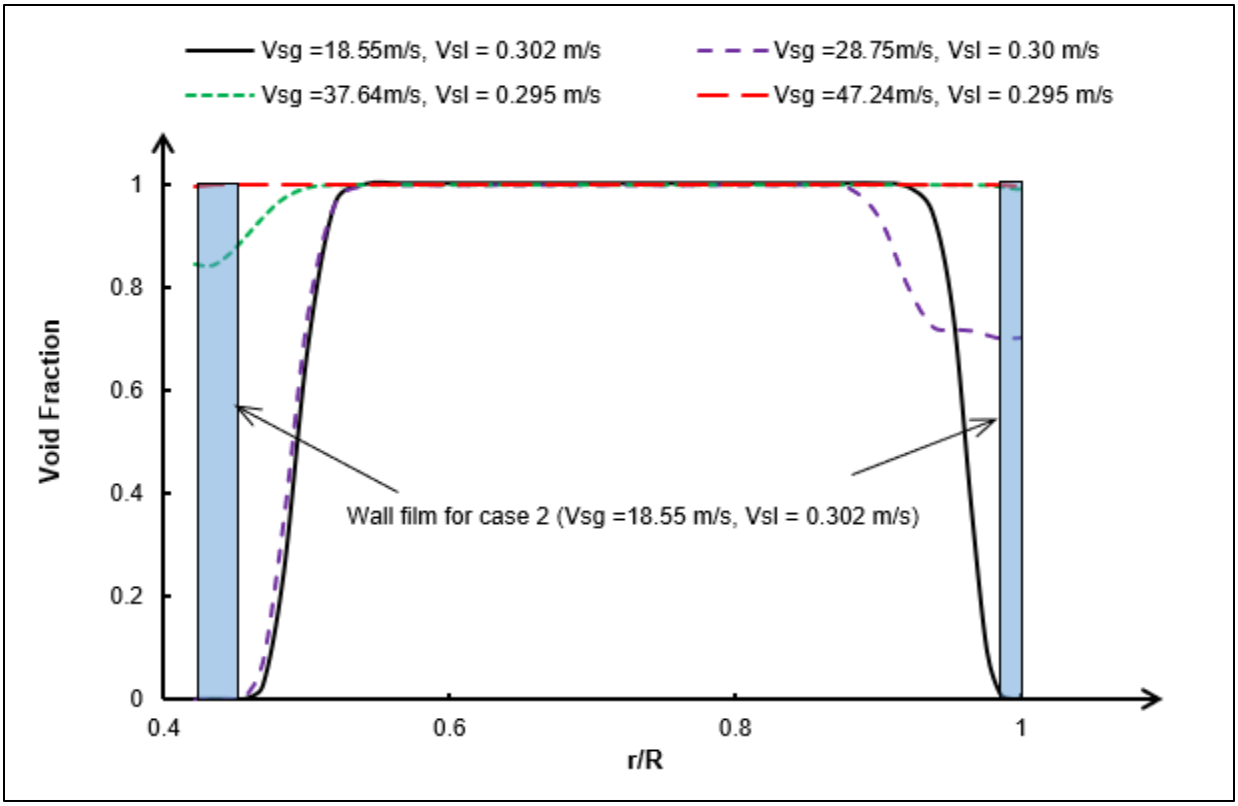

Figure 4.11 Void fraction distribution profile in the radial direction in the cross-sectional plane 1.5 m from the inlet

In the past, studies have heavily relied on the probability density function to characterize the flow regimes and calculate the void fraction in the spatial domains. In this study, the probability density functions were determined and compared. Hence, a cross-sectional plane was set at 1.5 m (axial distance) from the inlet point. The average void fraction data corresponding to this cross-sectional plane was recorded for 10 seconds of simulation time. To plot the probability density function (PDF), the initial 0.5 seconds of the data was neglected. This initial 0.5 second of the simulation corresponds to the time for the system to reach a fully developed flow condition. This decision was based on the average volume of void fraction, average turbulence kinetic energy, and average volumetric pressure of the system as depicted in Figures 4.5, 4.6, and 4.7.

PDFs can be generated by several methods. Two of them are histogram and kernel distribution method. Histogram creates a discrete PDFs, while the kernel distribution method produces a

smooth and continuous PDF. The kernel distribution is a nonparametric representation of PDF using a random variable which is defined by the smoothing function based on the shape of the curve for the PDF generation (Bowman and Azzalini 1997; Bendat and Peirsol 2011). The kernel smoothing function can be employed to estimate the probability density for the void fraction in the current cases. Experimental studies suggest that the single peak void fraction in the range of 0.8-1 is the characteristics of the annular flow pattern in the pipe while distributed single peak at void fraction close to 1 characterizes the churn flow (Matsui, 1986; Omebere-Iyari et al., 2008; Omebere-Iyari et al., 2007; Ali et al., 2014). The five simulated cases show similar trends. Case 1 belongs to churn regime as per the flow pattern map, and our visual observation (Figure 4.12a). The other cases were in the annular flow regime (Figure 4.12b).

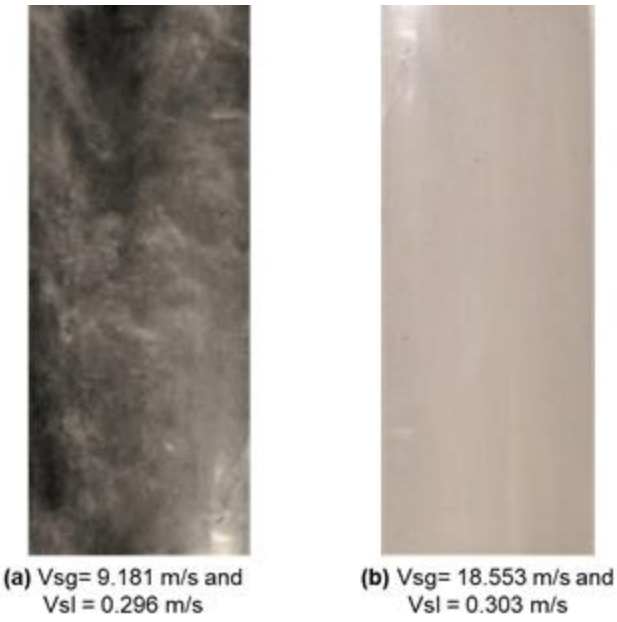

Figure 4.12 Photographic images (a) Case 1: Churn flow regime and (b) Case 2: Annular flow regime

The plots of PDFs based on simulation results distinctly show different patterns for the churn and annular case. The churn flow regime shows single distributed peaks with a void fraction of around 0.8 as depicted in Figure 4.13 (a). In the churn flow regime, the realizable k-ε model predicts a

higher value of void fraction than the shear stress transport (SST) *k-ω* model and closer to experimental data. It is also interesting to note that with an increase in the gas velocity, the peak starts to shift toward the maximum value of 1, which corresponds to the case of gas dominated flow. The four PDFs for the void fractions are depicted in Figures 4.13 (b), 4.13 (c), 4.13 (d), and 4.13 (e). The PDFs were plotted for both turbulence models: (a) Realizable *k-ε* and (b) shear stress transport (SST) *k-ω* model. The SST *k-ω* turbulence model shows (Figure 4.13 (b)) a higher void fraction than the realizable *k-ε* model and closer to the measured void fraction. The void fractions for this annular flow regime (Case 2) are 0.823 and 0.90 for realizable k-ε and SST k-ω models, respectively. The measured void fraction, in this case, is 0.891. Therefore, it can be concluded that the SST *k-ω* model provides a reasonably better phase distribution profile in the multiphase flow simulation of the annulus in the annular flow regime.

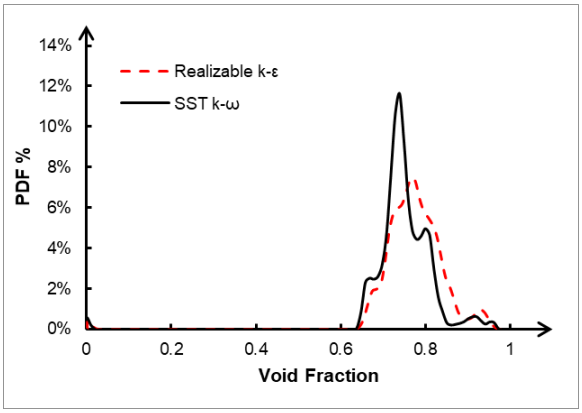

(a) Vsg = 9.181 m/s and Vsl = 0.296 m/s

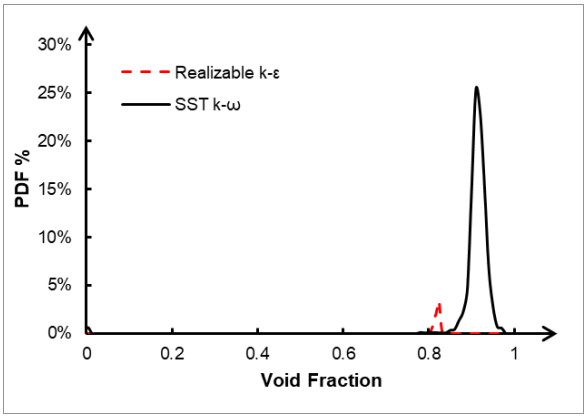

(b) Vsg = 18.553 m/s and Vsl = 0.303 m/s

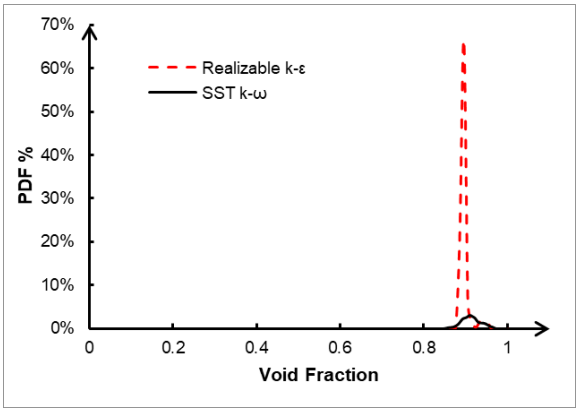

(c) Vsg = 27.25 m/s and Vsl = 0.3 m/s

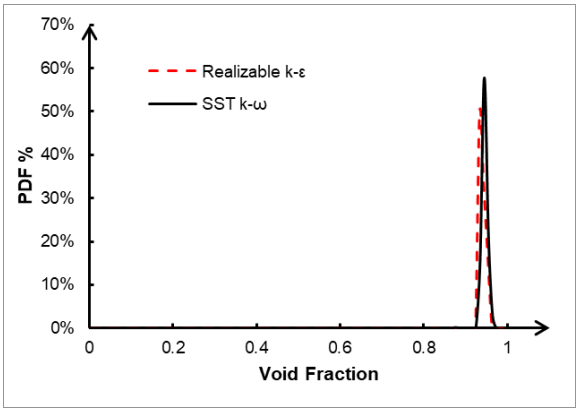

(d) Vsg = 37.64 m/s and Vsl = 0.295 m/s

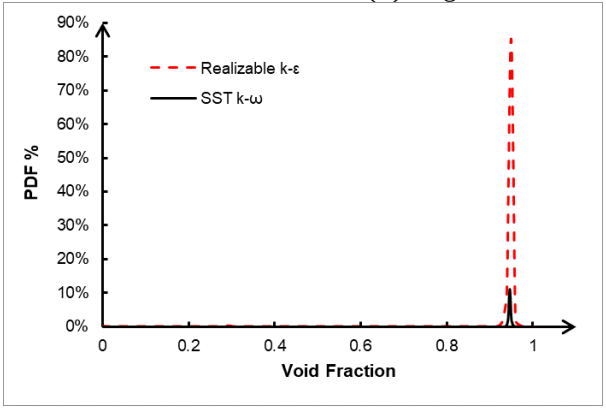

(e) Vsg = 47.24 m/s and Vsl = 0.293 m/s

Figure 4.13 Probability density function (PDF) percentage for void fraction corresponding to superficial gas and liquid velocity

The void fraction comparison for both sets of the simulated cases with the corresponding data from the experimental study is presented in Table 4.3 and Figures 4.14 and 4.15. It can be observed

from simulation results that at high superficial liquid velocity (0.58 m/s), the VOF method underpredicts the void fraction.

Table 4.3 Comparison of simulation and experimental results for void fraction

V_{sg} (m/s)	V_{sl} (m/s)	Void Fraction (Experiment)	Void Fraction (Simulation)	Void Fraction (Simulation)
			Realizable k-ε	SST k-ω
9.181	0.296	0.798	0.766	0.739
18.55	0.302	0.897	0.823	0.905
28.75	0.300	0.959	0.905	0.911
37.64	0.295	0.967	0.933	0.944
47.24	0.293	0.971	0.936	0.947
10.39	0.576	0.828	0.653	0.646
19.969	0.575	0.893	0.733	0.741
28.918	0.575	0.917	0.786	0.794
39.010	0.576	0.962	0.828	0.873
47.152	0.579	0.969	0.871	0.912

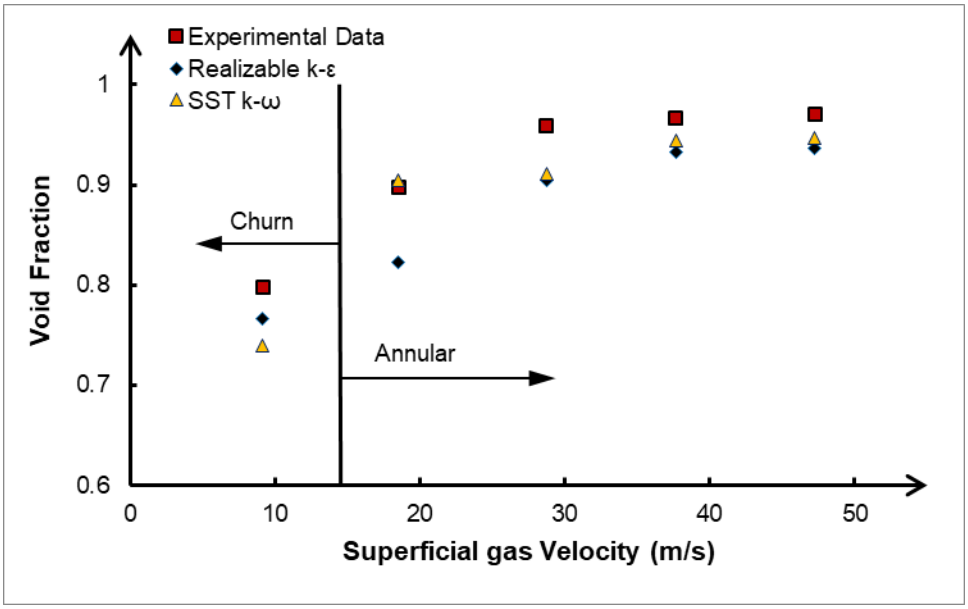

Figure 4.14 Measured and predicted void fractions at liquid flow rate of 77.5 LPM

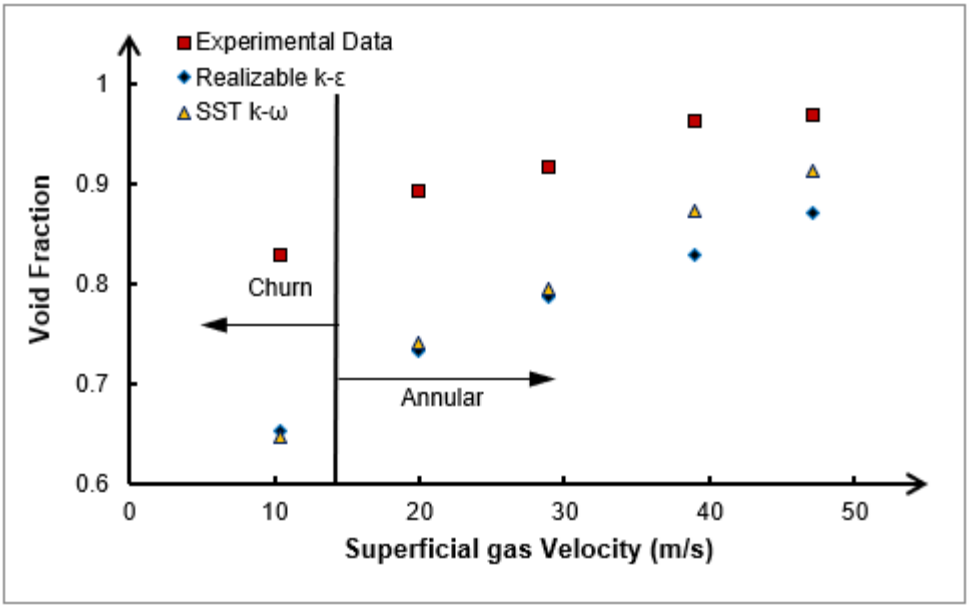

Figure 4.15 Measured and predicted void fractions at liquid flow rate of 155 LPM

Turbulence parameters such as turbulent kinetic energy and dissipation rate are other important characteristics of the multiphase flows. The turbulence parameters are dependent on the interfacial roughness which increases the flow resistance. Figure 4.16 shows the turbulence kinetic energy profile for the simulated cases. Berthelsen and Ytrehus (2005) pointed out that the interfacial roughness causes a deviation in the symmetric profile of the parameter, which is more pronounced with an increase in gas velocity. In addition to the roughness, wall shear stress variation between inner and outer walls results in non-symmetric profiles of these parameters. Similar observations can be seen in the current results. Near the vicinity of walls, the turbulent kinetic energy decreases while the dissipation rate increases as we approach the walls from the core. Also, as depicted in the void fraction plot (Figure 4.11), the gas phase erodes the liquid film with an increase in the gas flow rate. Hence, it becomes evident that the turbulence kinetic energy near the wall increases with the superficial gas velocity. A similar case exists for the turbulence dissipation rate as shown in Figure 4.17. The turbulent dissipation rate shows a distinct characteristic in the liquid wall film region. It decreases in the vicinity of the wall corresponding to the liquid film thickness as shown

in Figure 4.17. However, it is worth noting that this reduction is less than 0.5 m^2/s^3, while the maximum turbulent dissipation rate is 99.14 m^2/s^3 in this case.

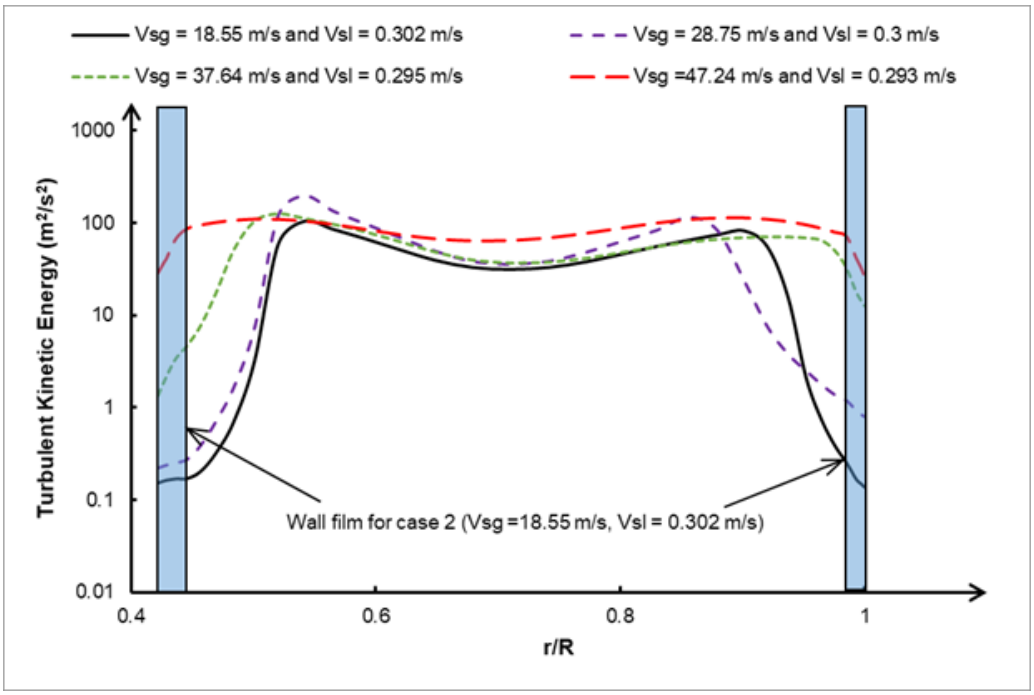

Figure 4.16 Turbulence kinetic energy profiles in the radial direction for different superficial gas velocities

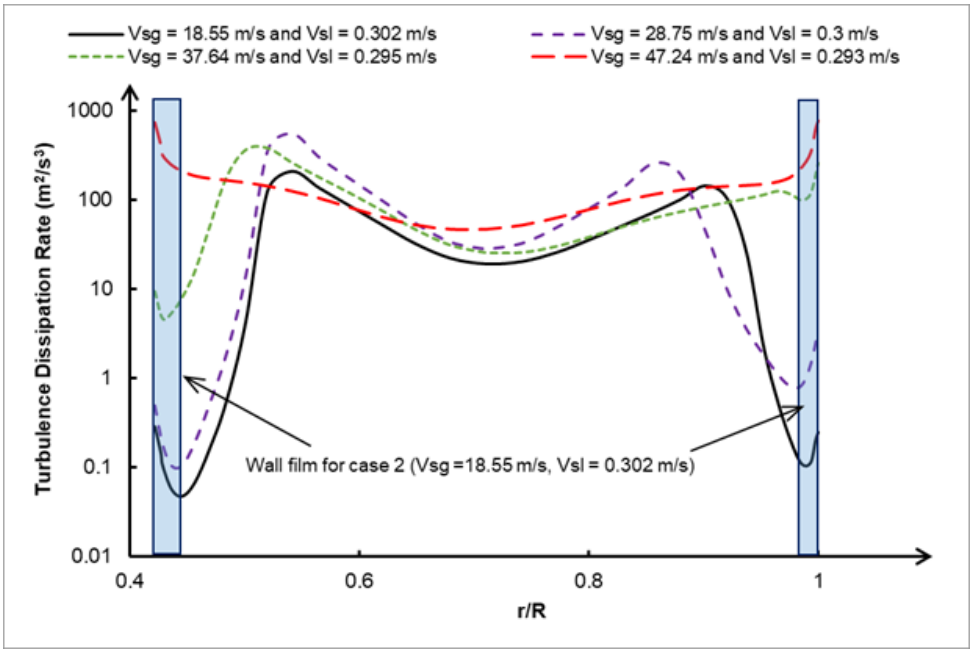

Figure 4.17 Turbulence dissipation rate profiles in the radial direction for different superficial gas velocities

4.2.5 Multiphase Model for Compressible Flow in Annulus

It is important to characterize the flow properties with the consideration of realistic field parameters. The experimental study indicates the notable change in the pressure profile in the test setup. Eventually, the effect of compressibility should be investigated. Hence, a CFD model was developed for the current laboratory set-up using the Eulerian hybrid model. The geometry was constructed using the quarter cross-section of the annulus as described earlier to minimize the computational cost. The model included the multi-VOF, dispersed phase, and implicit scheme. To characterize the turbulent, k-ω model was used in combination with SST. Also, the dispersed phase was considered for turbulent modeling. The energy equation was invoked to include the compressibility and temperature effect in the system. The fluid considered for two phases were air and water. The real gas Peng-Robinson model with Sutherland model for viscosity was used. Pressure boundary condition was used for inlet and outlet. At the inlet, the range of pressure (14.7-100 psi) was considered, while at the outlet zero total operating pressure was used. The walls (tubing and casing wall) were assigned as stationary with no-slip conditions.

Furthermore, the heat influx from the wall was neglected, since the current lab test section is insulated. The symmetry boundary condition was considered for both XY and YZ planes to reduce the computational time. The inlet condition was used as the reference value for calculation. The pressure-velocity coupling was included by using Coupled scheme in Fluent. For spatial discretization, different schemes were used: (a) Green-Gauss node-based method for gradient, (b) third-order MUSCL (Monotone Upstream-Centered Schemes for Conservation Laws) for momentum (c) QUICK (Quadratic Upstream Interpolation for Convective Kinematics) for volume fraction (d) second-order upwind for density, turbulent kinetic energy, specific dissipation rate, and energy. In addition, bounded second order implicit scheme was included for transient

formulation. To control the solution convergence, explicit relaxation factors, 0.3 for momentum and 0.5 for pressure was used. In order to avoid convergence in the flow simulation, different under-relaxation factors were used: (a) 0.5 for density, body forces, volume fraction, turbulent viscosity, and energy (b) 0.6 for turbulent kinetic energy and specific dissipation rate. Several report definitions were specified to monitor the convergence of the simulation. Some of the prominent monitoring parameters were residuals, mass flux, and volumetric average pressure profile with time steps. The calculation was initialized using the inlet conditions. The convergence criteria for residuals were included as 0.001. Variable and fixed stepping was chosen based on the convergence pattern of the simulation. The simulation was run till the significant convergence was observed in terms of constant pressure profile, residual and mass flux on the order of 10^{-3}.

As shown in the pressure profile depicted in Figure 4.18, the pressure reduces sharply at the entrance within 0.5 m from the inlet with a significantly high gradient. The exit pressure is atmospheric. Note: Figure 4.18 - 4.21 depicts the simulation results from a reference point, which is at a distance of 19.05 mm in X and Y direction from the origin shown in Figure 4.1.

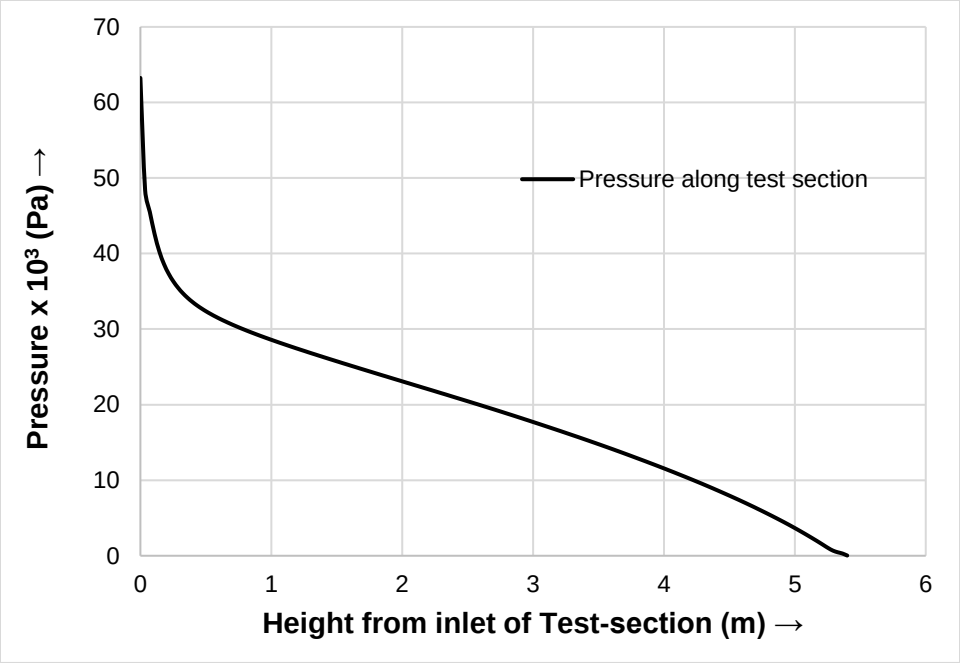

Figure 4.18 Pressure profile along the axial direction of 83mm × 35mm annulus at 15 psi as inlet pressure condition (The pressure decreases as we move upward from the inlet point)

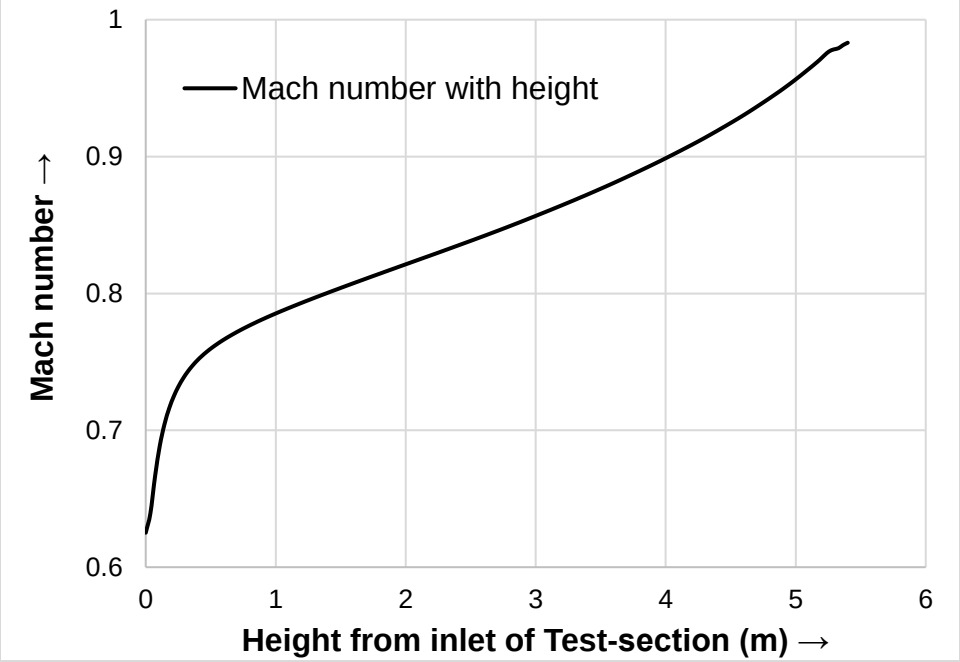

Figure 4.19 Mach number variation in the axial direction for 15 psi inlet pressure condition in 83mm × 35mm annulus (Mach number increases with height from the inlet point)

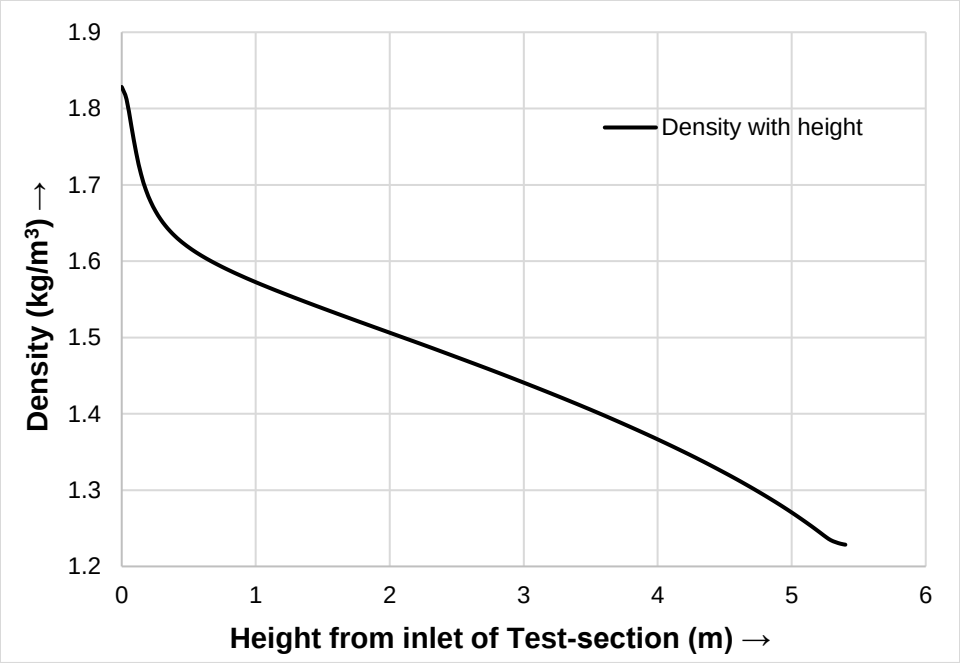

Figure 4.20 Variation of air density in the axial direction of 83mm × 35mm annulus for 15 psi inlet condition (The density of air decreases with the height from the inlet of the test section)

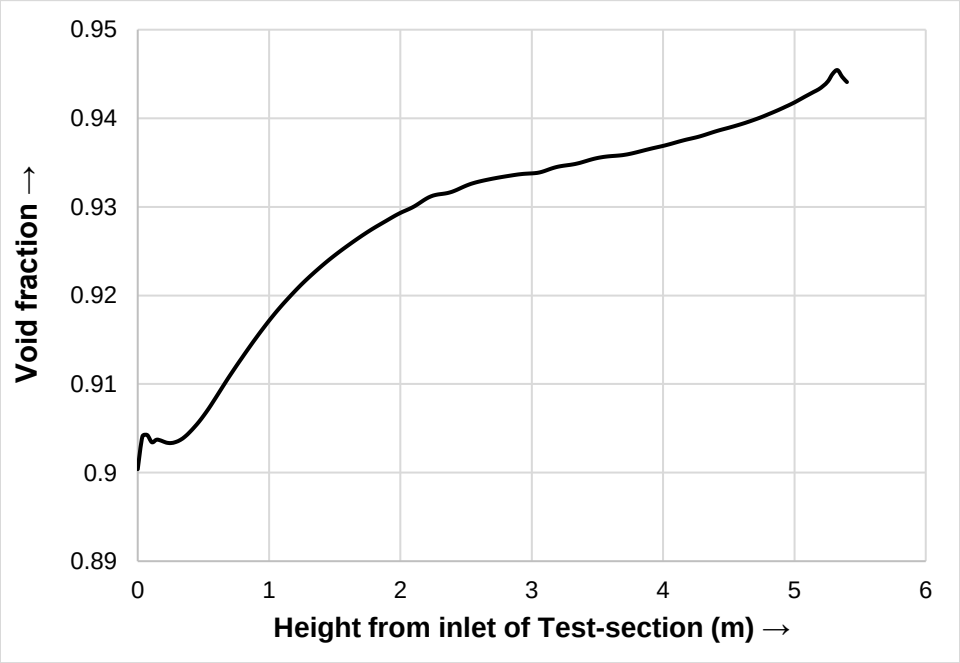

Figure 4.21 Void fraction distribution along the length of 83mm × 35mm annulus (The void fraction increases with the height)

The Mach number profile (Figure 4.20) suggest that the maximum Mach number for 14.7 psi operating pressure is 0.95 is close to the exit. However, it should be kept in mind that ANSYS

Fluent calculates the Mach number as the ratio of the velocity of gas and speed of sound in air. The ANSYS result is adjusted based on the speed of the sound corresponding to air and water volume fraction and the pressure in the flow domain as shown in Figure 4.22.

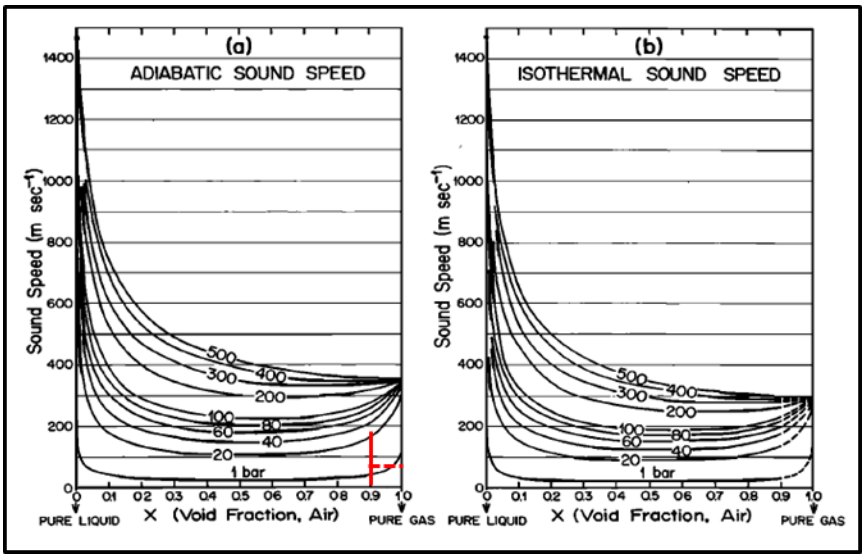

Figure 4.22 Variation of (a) adiabatic and (b) isothermal speed of sound in air-water mixture with gas void fraction and pressure (Kieffer, 1977)

Apart from the 14.7 psi case, two more cases of high velocity are simulated. The cases include the variation of inlet pressure 50 psi and 100 psi with 0.1 as the volume fraction of water. The air is introduced at this operating pressure with velocity having 0.7 Mach number. The comparative results of the pressure gradient are presented in Figure 4.23. The result suggests that there will be two inflection point in the system. One is near the inlet, and other is close to the outlet. This significant increase in pressure drop also reflects in Mach number and consequently high velocity near the outlet. Similar pressure profile is also reported for the multiphase flow in the nozzle by Henry (1968). The different pressure gradients can provide a useful criterion to develop the WCD tool.

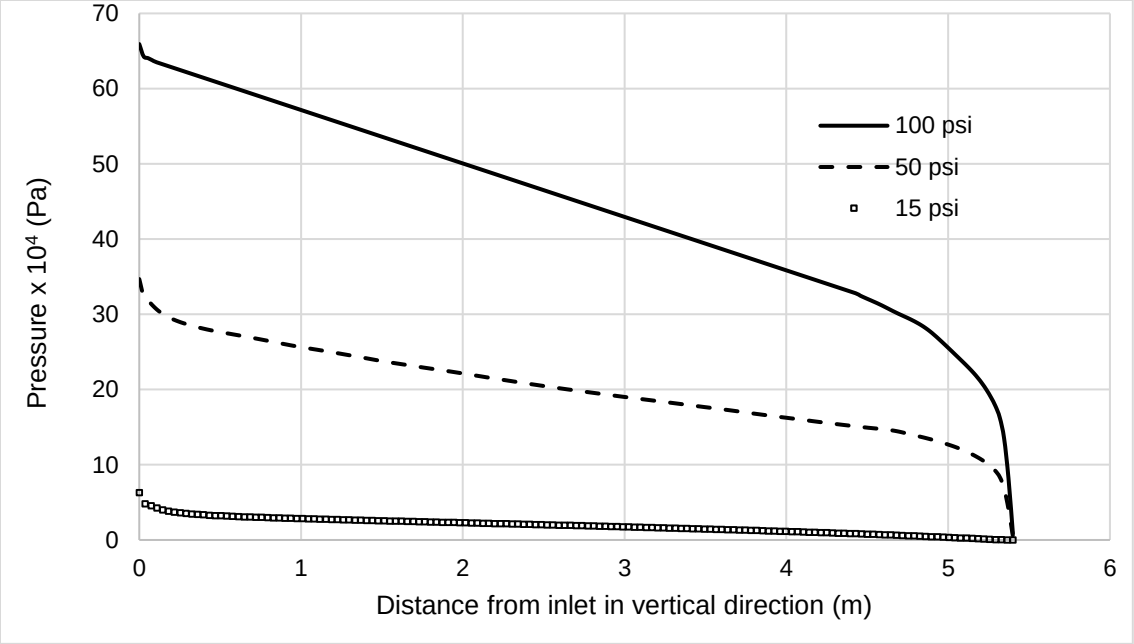

Figure 4.23 Pressure profile for different operating pressure (83mm × 35mm annulus)

Figure 4.24 represents the pressure profile for 50 psi pressure gradient, and it has three pressure gradients. The pressure gradient at the outlet is highest and approximately twice as that of mid-section. This can also be attributed to high Mach number condition at the exit. The value of pressure gradient at inlet lies in between the values corresponding to the mid-section and top-section.

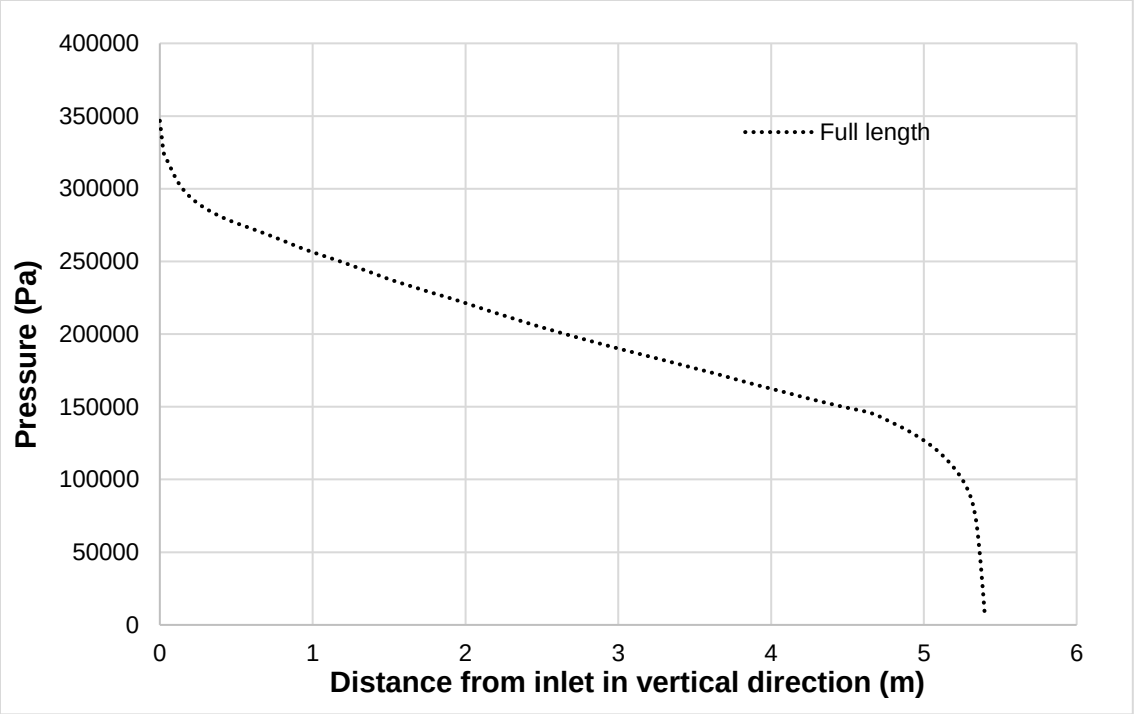

Figure 4.24 Pressure profile for 50 psi operations with different pressure gradients for various parts of test section in 83mm × 35mm annulus (highest pressure gradient at the outlet and lowest in the middle part)

The maximum velocity for air corresponding to 50 psi and 100 psi operation pressure was found out to be 120.788 m/s and 170 m/s. As per Kieffer (1977), experimental data (shown in Figure 4.22), the velocity of sound in case of 50 psi (3.44 bar) and 100 psi (6.89 bar) for 0.1 as liquid fraction will be 58 m/s and 154 m/s. This will correspond to the Mach number 2.08 and 1.1 respectively.

4.3 Chapter Summary

Worst-case discharge (WCD) is generally linked with high-velocity flow conditions. The high-velocity multiphase flow is difficult to characterize with conventional multiphase flow modeling. Past studies have not used computational fluid dynamics (CFD) study for flow modeling in the annulus. In this study, CFD is used to model and characterize two-phase fluid flow in the annulus using ANSYS Fluent. It is worth noting that the CFD modeling requires significant computational effort. Hence, an effort has been made to optimize the modeling work without compromising the

accuracy of results significantly. In pursuit of this, several approaches are outlined and used, such as mesh sensitivity analysis, optimization of simulated annulus section length, using a quarter sectioned annulus instead of the full cross-section.

Different models used during the investigation are validated and verified using the current experimental data. The volume of fluid (VOF) approach in combination with turbulence models (SST k-ω and realizable k-ε) are used to characterize the annular and churn flow in the annulus. The flow regimes are distinguished using the probability density function (PDF) on the dynamic evolution of void fractions. The void fraction PDFs for annular flow regime shows a single peak at the higher end of void fraction. On the other hand, the churn flow regime is depicted by a distributed peak with a lower void fraction compared to the annular flow regime. The pressure gradients and void fraction compared with the experimental data show reasonable agreement. In addition, high Mach number (Ma > 0.3) flows were simulated considering the effects of temperature and compressibility on the flow characteristics.

Chapter 5: WCD Computational Tool

5.1 Overview

In the wake of deep-water horizon incident, there were several open questions that came into the picture. One such question was based on the estimation of worst-case discharge (WCD). This study includes a brief description of the WCD model. The WCD model is based on the nodal analysis. The model comprised of four submodels: (a) reservoir model, (b) production model, (c) PVT models, and (d) hydrodynamic models. The scope of this study is an overview of the reservoir models, production models, and PVT models. Different hydrodynamic models have been tested for multiphase flow in pipe and annulus, and the details are provided in later sections. Furthermore, a modified model for annular flow in annulus was also developed and presented in this chapter.

5.2 Nodal Analysis

Nodal analysis is based on the inflow performance relationship (IPR) and vertical lift performance (VLP) curve which is constructed using the bottom hole pressure and the surface production rate. VLP takes into the concept of well deliverability under the specific operating conditions. IPR is based on reservoir properties. Gilbert (1954) proposed the matching of inflow and outflow performance of the well which was further termed as nodal analysis by Brown and Lea (1985). The nuance of the nodal analysis fits well with WCD estimation where the reservoir properties and well parameters govern the flow rate of the fluid in case of loss of well control incidents.

In the case of WCD, the fluid comes out of the reservoir at certain in-situ conditions such as reservoir pressure and temperature and travels through the wellbore to establish the overall equilibrium. In order to represent the system accurately, it requires the accuracy of the models for IPR and VLP. It should be noted that the scope of this study is limited to the evaluation of

hydrodynamics models and consequently the effect on the vertical lift performance relationship. The firm black line in figure 5.1 depicts the typical VLP curve. The red dot represents the operating condition for which this VLP plot is generated.

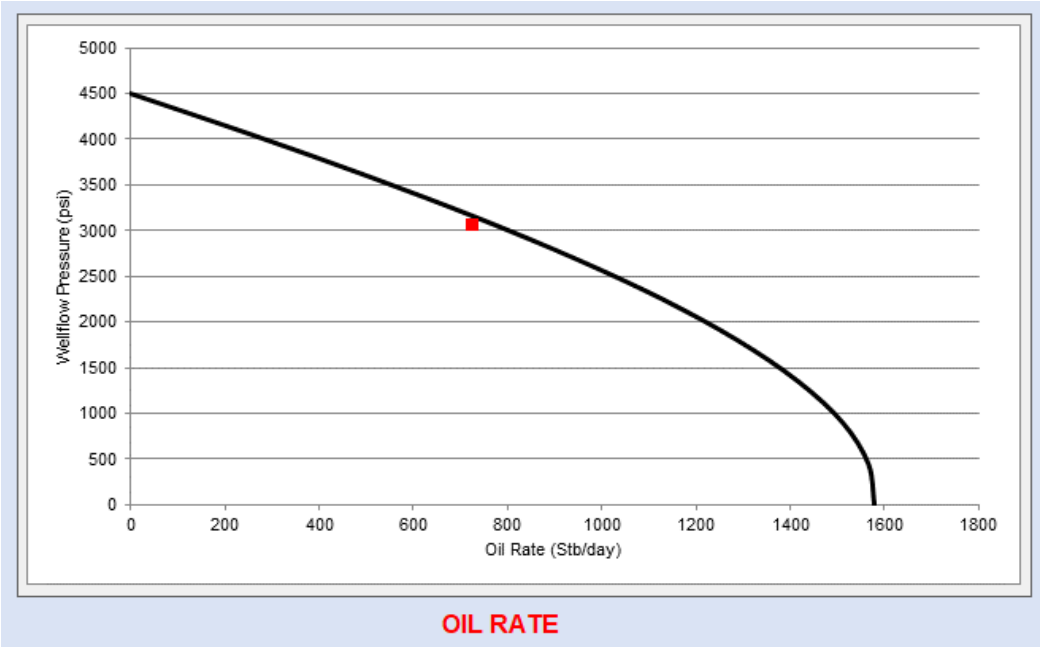

Figure 5.1 Vertical lift performance curve (Wellbore pressure vs. oil rate)

The flow chart for the WCD estimation is presented in Figure 5.2. For WCD estimation, the wellbore is divided into small segments, referred to as nodes. In this process, i =1 refers to the bottom-most node (i refers to grid numbering scheme). The different reservoir parameters are taken as input for the program at this node (i = 1), and bottom hole pressure is assumed. The detailed equations for reservoir parameter estimation (such as permeability, formation volume factor, solubility) are attached in the appendix. Based on these parameters, the flow rate of gas and liquid phases are calculated. The liquid and gas flow rates are subsequently converted to the superficial gas and liquid velocities. The superficial gas and liquid velocities and the fraction of different phases are used to estimate the pressure gradient in that grid. The pressure of the next grid is calculated. Based on the local pressure and temperature, the fluid properties of that grid

location are calculated. The superficial gas and liquid velocities are calculated for that grid, and the loop continues until it reaches the wellhead. At this location, the pressure is also tested to release for the free gas from the fluid. In case of existence of free gas, the fraction of different phases is recalculated before moving further upwards. After obtaining the pressure at the surface, the wellhead pressure is matched with the calculated pressure and the loop will continue till it matches. In addition to this, another sub-loop is also introduced to check the sonic conditions are established in the wellbore. The sonic conditions are determined using the newly developed correlation for sonic velocity (details are provided in section 5.5). The sonic velocity is matched with the superficial gas velocity. If the superficial gas velocity is greater than the sonic velocity, the sonic condition takes the preference as the governing criteria. In case of the sonic condition in the wellbore, the given wellhead (exit) pressure is incremented in small steps, and the superficial gas velocity of the wellbore is matched with sonic velocity. If the superficial velocity is greater than the sonic velocity at any depth of the wellbore, the wellhead pressure is increased, and the loop is continued until the sufficient match is observed.

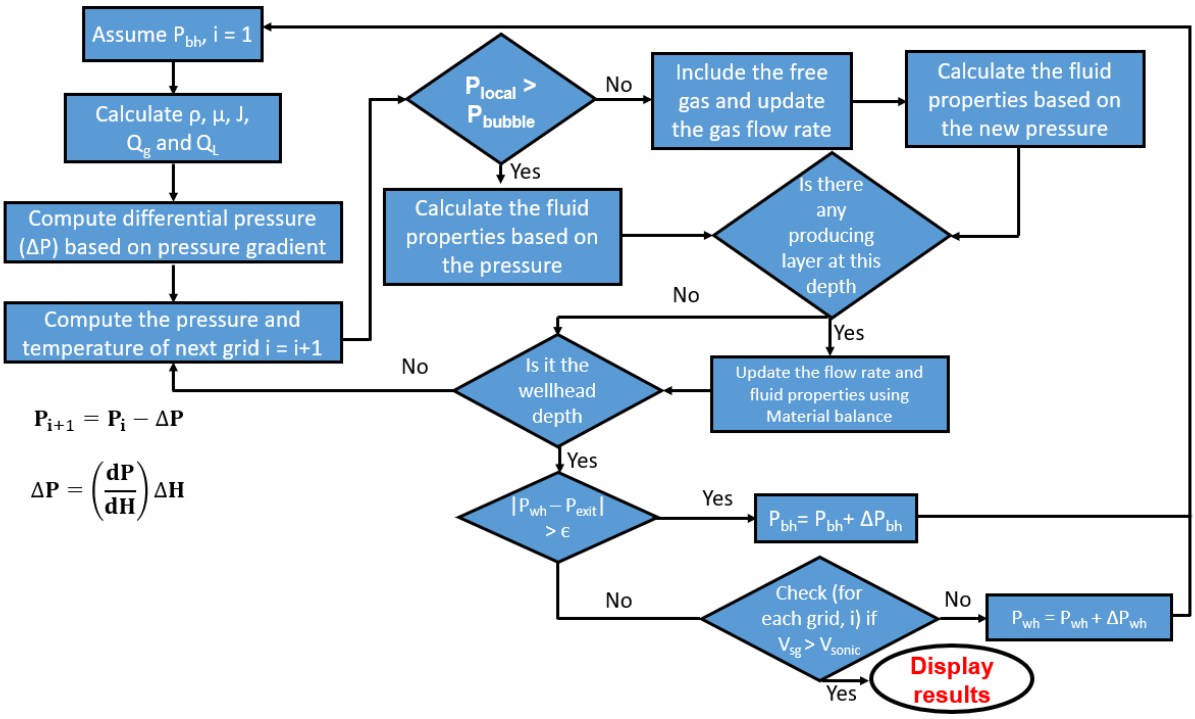

Figure 5.2 Flow chart for WCD estimation

The required input data for WCD calculation is shown in Table 2.1. The input data is categorized into three parts based on the tool components. Reservoir data is mainly based on formation and fluid properties. The wellbore parameters include the depth, size, and casing/liner properties. In addition, the surface parameters comprise the wellhead pressure and surface temperature. The surface temperature is used in obtaining the temperature profile of the well.

Table 5.1 Input data for WCD calculation

Reservoir Parameters	Wellbore Parameters
Number of producing layers	Measured well depth
Reservoir type for each layer	Kickoff point
Formation type for each layer	Deviation angle from Vertical
Reservoir pressure	Casing inner diameter
Reservoir temperature for each layer	Open hole diameter
Reservoir permeability for each layer	Cased hole diameter
API gravity for each layer	Length of the open hole section
Gas specific gravity for each layer	Hole diameter behind liner casing
Drainage radius	Liner inner diameter
Bubble point pressure	Casing roughness
Gas saturation for each layer	Open hole roughness
Water saturation for each layer	Liner roughness
Irreducible water saturation	Casing shoe depth
Critical gas saturation	Wellhead pressure
Critical oil saturation	Surface temperature
Skin factor for each layer	
Condensate yield	
Salt content	
Initial water saturation	

5.3 Hydrodynamic model for flow in pipe

Hydrodynamic models are used in the nodal analysis to construct the VLP curves. The accuracy of the hydrodynamic models is reflective in the accurate representation of the wellbore pressure profile. In the development of the WCD tool, an extensive comparison of the existing models was carried out, and the suitable models were identified to obtain the pressure gradient for the range of superficial gas and liquid velocity. A modified flow map is constructed based on the evaluated models for pressure gradient calculation as depicted in Figure 5.3 (the details of models are beyond the scope of this study).

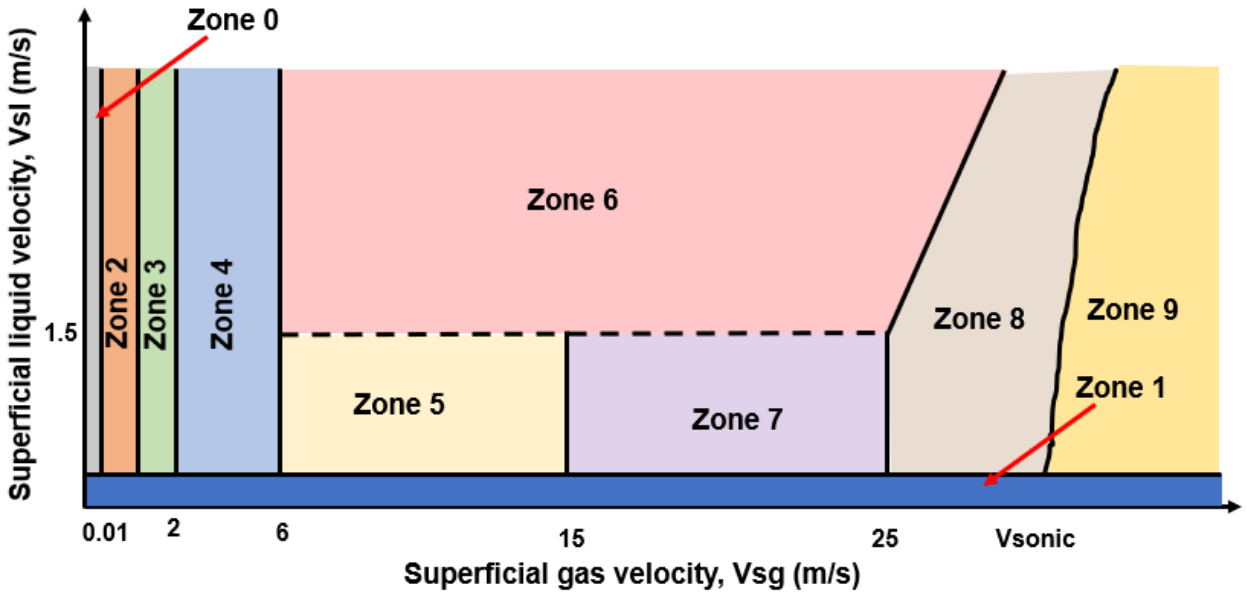

Figure 5.3 Flow pattern description

Zone 0 and 1 represents the single-phase flow. Zone 0 is gas dominated flow while Zone 1 is liquid dominated flow. Zone 2 represents the bubbly flow region where the gas velocity is less than critical gas velocity. Zone 3 represents the low-velocity slug region where gas velocity is greater than critical gas velocity and less than 2 m/s. Zone 4 represents the hybrid slug flow velocity regime while Zone 5 represents the slug flow velocity regime. Zone 6 represents high slug velocity region, while zone 7 represents a hybrid annular region. Zone 8 represents the annular flow region. Once the flow rate exceeds the sonic velocity, the flow assumes the zone 9 characteristics.

The single-phase flow (Zone 0 and 1) is modeled based on the frictional pressure loss calculation from the moody chart. The bubbly flow regime (Zone 2) and low-velocity slug flow regime are modeled using the Hasan and Kabir model (1988). The pressure drops for the high-velocity slug flow regime and the annular flow regimes are calculated using the models suggested by Ansari et al. (1994). One of the main limitations of the program was to establish a smooth transition between the different flow regimes. Hence, two hybrid models were constructed for the transition from low-

velocity slug flow regime to high-velocity slug flow regime and high-velocity slug flow regime to annular flow regime. The hybrid model was constructed using the weighted average of the pressure gradient corresponding to velocities in the regimes involves. Pressure gradient obtained from the hybrid model for low and high velocities slug is given by:

$$\left(\frac{dp}{dL}\right)_{Hyb} = \left(\frac{V_{sg\_T} - V_{sg\_Lower}}{V_{sg\_Upper} - V_{sg\_Lower}}\right)\left(\frac{dp}{dL}\right)_{LS} + \left(\frac{V_{sg\_Upper} - V_{sg\_T}}{V_{sg\_Upper} - V_{sg\_Lower}}\right)\left(\frac{dp}{dL}\right)_{HS} \quad (5.1)$$

where V_{sg_Lower}= 2 m/s and V_{sg_Upper} = 6 m/s

For annular – high-velocity slug hybrid model, the total pressure gradient is calculated as:

$$\left(\frac{dp}{dL}\right)_{Hyb} = \left(\frac{V_{sg\_T} - V_{sg\_Lower}}{V_{sg\_Upper} - V_{sg\_Lower}}\right)\left(\frac{dp}{dL}\right)_{HS} + \left(\frac{V_{sg\_Upper} - V_{sg\_T}}{V_{sg\_Upper} - V_{sg\_Lower}}\right)\left(\frac{dp}{dL}\right)_{Ann} \quad (5.2)$$

where V_{sg_Lower}= 15 m/s and V_{sg_Upper} = 25 m/s. $\left(\frac{dp}{dL}\right)_{Hyb}$ is the total pressure gradient calculated from the hybrid model, $\left(\frac{dp}{dL}\right)_{LS}$, $\left(\frac{dp}{dL}\right)_{HS}$, $\left(\frac{dp}{dL}\right)_{Ann}$ are the total pressure gradient calculated from the low-velocity slug, High-velocity slug, and annular flow model, respectively. V_{sg_Lower} and V_{sg_Upper} are the lower and upper superficial gas velocities boundary for each hybrid model. V_{sg_T} is the superficial gas velocity.

These models were tested for the available experimental data. The details of this validation are not in the scope of this work. However, the comparative analysis suggested that the maximum mean percentage error for different zones were within 25 %.

5.4 Hydrodynamic models for flow in the annulus

In addition to the mechanistic models for flow in a pipe, the mechanistic models for flow in the annulus are also studies. The primary goal of conducting experiments is to develop and validate the models which can be used in field operations for flow characterization. Several models have been developed over time to characterize the pressure drop in the wellbore. In this study, a broader

range of data including the Caetano (1986) and current experimental work has been used to test the past models. It is worthy to note that the pressure gradients for past models have never been tested for higher superficial gas velocities (>22 m/s). In this section, the past models have been tested for different flow regimes except for the dispersed bubble and churn flow regime. In addition, a modified mechanistic model is also presented for annular flow regime.

5.4.1 Bubble Flow Model

The modeling work for bubble flow regime has evolved significantly over time. Three models have been tested for 13 data points provided for bubble flow regime in Caetano (1986) experimental study. These three models are (a) Caetano et al. (1992b), (b) Lage and Time (2000) and (c) Hasan and Kabir (1988). Caetano et al. (1992b) used the concept of slippage and solitary bubble rise velocity presented by Harmathy (1960). Lage and Time (2000) used the slip velocity definition from Papadimitriou and Shoham (1991) in pressure gradient calculation. Hasan and Kabir (1988) implemented the drift flux approach for pressure gradient characterization. Out of these three models, the pressure gradient prediction by Caetano (1992b) has greater accuracy with respect to absolute average error as shown in Table 5.2. This can be attributed to the model for the bubble rise velocity in an infinite medium.

Table 5.2 Bubble flow Models and the percentage average and absolute average error

Models	E_{avg}	E_{aavg}
Caetano (1992b)	7.67	6.08
Lage and Time (2000)	5.73	10.7
Hasan and Kabir (1988)	8.24	12.49

The Eavg is the average percentage error and can be calculated using the following equation:

$$E_{avg} = \frac{100}{n}\sum_{i=1}^{n} E_i \quad (5.3)$$

where n is the total number of data points, and E_i is an error in the pressure gradient and can be calculated by equation 5.4.

$$E_i = \frac{P_{g,cal} - P_{g,meas}}{P_{g,meas}} \quad (5.4)$$

where $P_{g,calc}$ is calculated pressure gradient and $P_{g,meas}$ is the measured pressure gradient. E_{aavg} is the percentage absolute average error which can be given by:

$$E_{avg} = \frac{100}{n}\sum_{i=1}^{n} |E_i| \quad (5.5)$$

5.4.2 Dispersed Bubble Flow Model

The dispersed bubble flow has been implemented using the homogenous mixture velocity concept by most of the researchers. Hence, the dispersed bubble model is not tested in this study.

5.4.3 Slug Flow Model

The slug flow is the most commonly observed flow regime in large diameter pipes/annulus (Zabaras et al., 2013; Waltrich et al., 2015). There are several models available for prediction of pressure gradients in the slug flow regime. In this study, the 14 data points with pressure gradients presented by Caetano (1986) were considered for comparison. Two models: (a) Caetano et al. (1992b) and (b) Hasan and Kabir (1988) for slug flow were tested. Caetano et al. (1992b) model is based on the hydrodynamic modeling while the Hasan and Kabir (1988) model is based on the drift flux approach. It is worthy to note that the friction factor calculation in Hasan and Kabir (1988) model was conducted based on the model suggested by Caetano (1986) in this study. The results suggest that Hasan and Kabir (1988) model works better than Caetano et al. (1992b). The absolute average error for the dataset is around 5% for Hasan and Kabir and 10% for Caetano et

al. (1992b) model. However, the higher error in Caetano et al. (1992b) can be attributed to the assumption of symmetric Taylor bubbles in the slug flow regime.

Table 5.3 Slug flow Models and the percentage average and absolute average error

Models	E_{avg}	E_{aavg}
Caetano et al. (1992b)	6.37	10.23
Hasan and Kabir (1988)	3.05	5.4

5.4.4 Annular Flow Model

Several studies have been conducted over the years to characterize the annular flow pattern. The annular flow models are based on the hypothesis that there are two separate zones in the spatial domain of the flow. It consists of the gas core with entrained liquid and two thin films on the walls of outer and inner pipe as depicted in Figure 5.4. The annular flow develops at higher gas velocity and relatively lower liquid flow rate. The mechanistic models for annular flow in pipes have undergone significant development over the years. However, the models for flow in the annulus are limited and had not been tested for a broader range of the data. In pursuit of establishing confidence in the mechanistic model for annular flow regime, a modified model based on work from Lage and Time (2000) has been presented. The original model does not incorporate the effect of entrainment of droplets in the gas core. When the previous model was subjected to the current experimental data, it showed a considerable deviation in the average error. The model shows a good agreement at a gas density in the range corresponding to atmospheric temperature and pressure (1.225-1.5 kg/m^3). The current study confirms that the incorporation of liquid entrainment, as well as the geometrical parameter for the friction factor, improves the accuracy of results in the modified model.

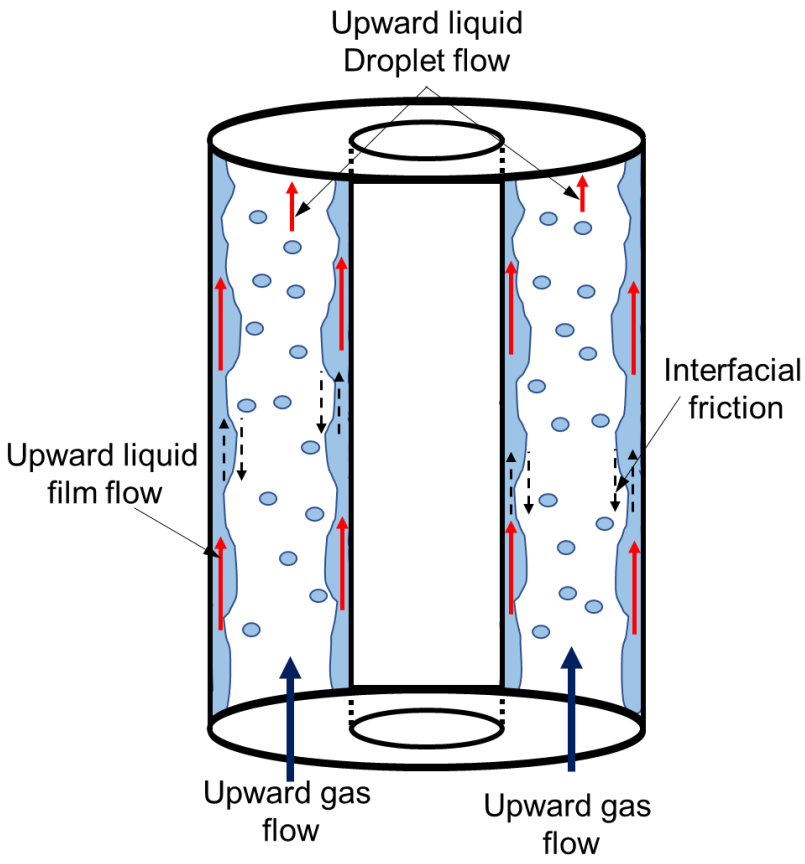

Figure 5.4 Annular flow geometry

This model is based on the momentum balance in a differential length segment corresponding to the gas core and the annulus. Considering the same liquid film thickness on the inner and the outer wall. The area of the gas core is given by:

$$A_c = \frac{\pi}{4}[(D_c - 2\delta)^2 - (D_t + 2\delta)^2] \tag{5.6}$$

where A_c is the cross-sectional area of the gas core, D_c is the inner diameter of the outer pipe (casing), D_t is the outer diameter of the inner pipe (tubing), and δ is the film thickness on both walls. The gas void fraction (α) can be presented by the following formula:

$$\alpha = 1 - \frac{A_c}{A_t}(\alpha_{entrainment}) - \frac{A_t - A_c}{A_t} \tag{5.7}$$

where, $\alpha_{entrainment}$ is the liquid entrained inside the annulus, and A_t is the total cross-sectional area of the annulus which is given by:

$$A_t = \frac{\pi}{4}(D_c - D_t)^2 \tag{5.8}$$

The entrainment fraction of liquid ($\alpha_{entrainment}$) inside the gas core can be given by the correlation developed by the Wallis (1969) and is as follows:

$$\alpha_{entrainment} = 1 - e^{\left[-0.125\left(10^4 V_{sg}\frac{\mu_g}{\sigma}\left(\frac{\rho_g}{\rho_l}\right)^{0.5} - 1.5\right)\right]} \tag{5.9}$$

where V_{sg} is the superficial gas velocity, μ_g is the gas viscosity, σ is surface tension, ρ_g is the density of the gas, and ρ_l is the density of the liquid.

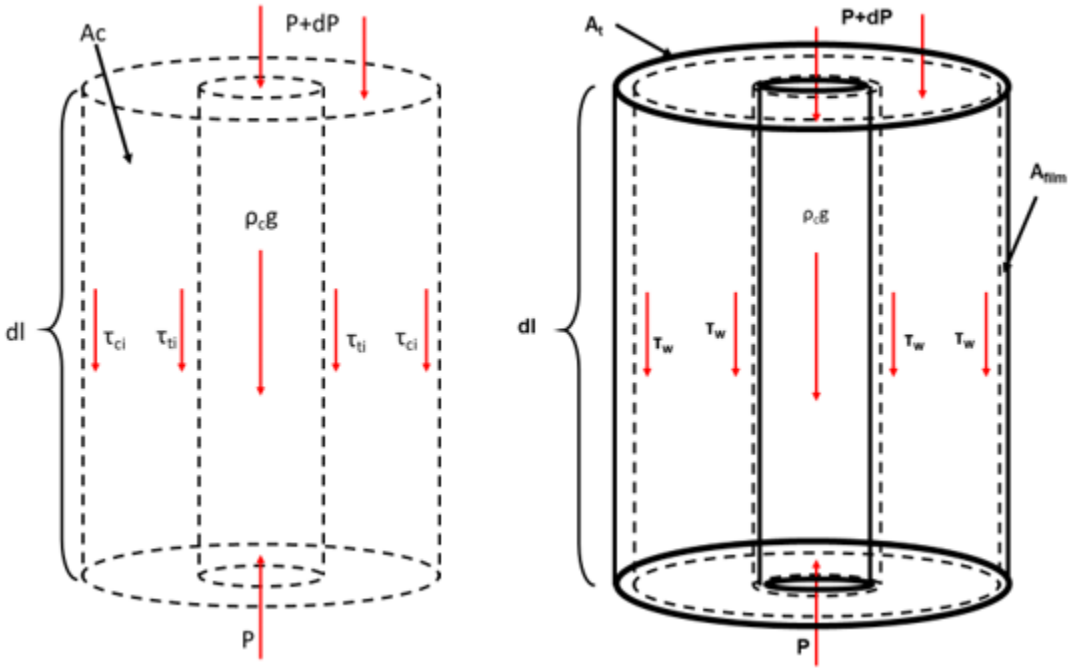

Figure 5.5 Momentum balance for an annulus segment for annular flow regimes on (a) the gas core and (b) total cross-sectional area

Now applying the momentum balance equation on the differential element dz of the gas core as shown in Figure 5.5, the following relation can be obtained:

$$\left(\frac{dP}{dl}\right)_1 + \rho_g g + \frac{S_{ti}\tau_{ti} + S_{ci}\tau_{ci}}{A_c} = 0 \tag{5.10}$$

where S_{ti} and S_{ci} are perimeters associated with gas-liquid interfaces at casing and tubing films and are given by:

$$S_{ti} = \pi(D_t + 2 * \delta) \tag{5.11}$$

$$S_{ci} = \pi(D_c - 2 * \delta) \tag{5.12}$$

Also, τ_{ti} is the interfacial shear stresses at the tubing wall, and τ_{ci} is the interfacial shear stress at the casing wall. The interfacial shear stresses at both walls can be given by the following formula as proposed by Harmathy (1960).

$$\tau_{ti} = 0.0025\left(1 + 300\frac{\delta}{D_t}\right)\rho_g {V_{sg}}^2 \tag{5.13}$$

$$\tau_{ci} = 0.0025\left(1 + 300\frac{\delta}{D_c}\right)\rho_g {V_{sg}}^2 \tag{5.14}$$

Now applying the momentum balance on the outer control volumes for differential segment dl is given as follows:

$$\left(\frac{dP}{dl}\right)_2 + \left[\alpha\rho_g + (1-\alpha)\rho_l\right]g + \frac{2f}{D_h}\rho_l\overline{V_m}^2 = 0 \tag{5.15}$$

where f is the friction factor corresponding to mean velocity $\overline{V_m}$ and can be estimated using the frictional factor as discussed in section 3.6.1.1. In this case, the Reynolds number, R_e can be calculated as follows:

$$R_e = \frac{\rho_l\overline{V_m}D_h}{a\mu_l} \tag{5.16}$$

where μ_l is the viscosity of the liquid phase. Now, the mean velocity is given as follows:

$$\overline{V_m} = {V_{sl}}/{F(\alpha)} \tag{5.17}$$

where F(α) can be calculated from equation 24 as suggested by Kledessis and Dukler (1989).

$$F(\alpha) = \frac{9.152}{(D_c^2 - D_t^2)}\left[\frac{7}{\left(0.5(2r_m - KD_c)\right)^{1/7}}\left\{\frac{D_t\delta^{8/7}}{16} + \frac{\delta^{15/7}}{15}\right\} + \frac{7}{\left(0.5(D_c - 2r_m)\right)^{1/7}}\left\{\frac{D_c\delta^{8/7}}{16} + \frac{\delta^{15/7}}{15}\right\}\right] \tag{5.18}$$

where r_m is the point of zero stress corresponding to maximum velocity profile and is given by:

$$r_m = \frac{D_c}{2}\sqrt{\frac{1-K}{2\ln\left(\frac{1}{K}\right)}} \tag{5.19}$$

Now, the equations can be solved iteratively by the initial assumption of the film thickness and calculating the pressure gradients from equations 5.10-5.15. The flow chart for the solution is provided in Figure 5.6.

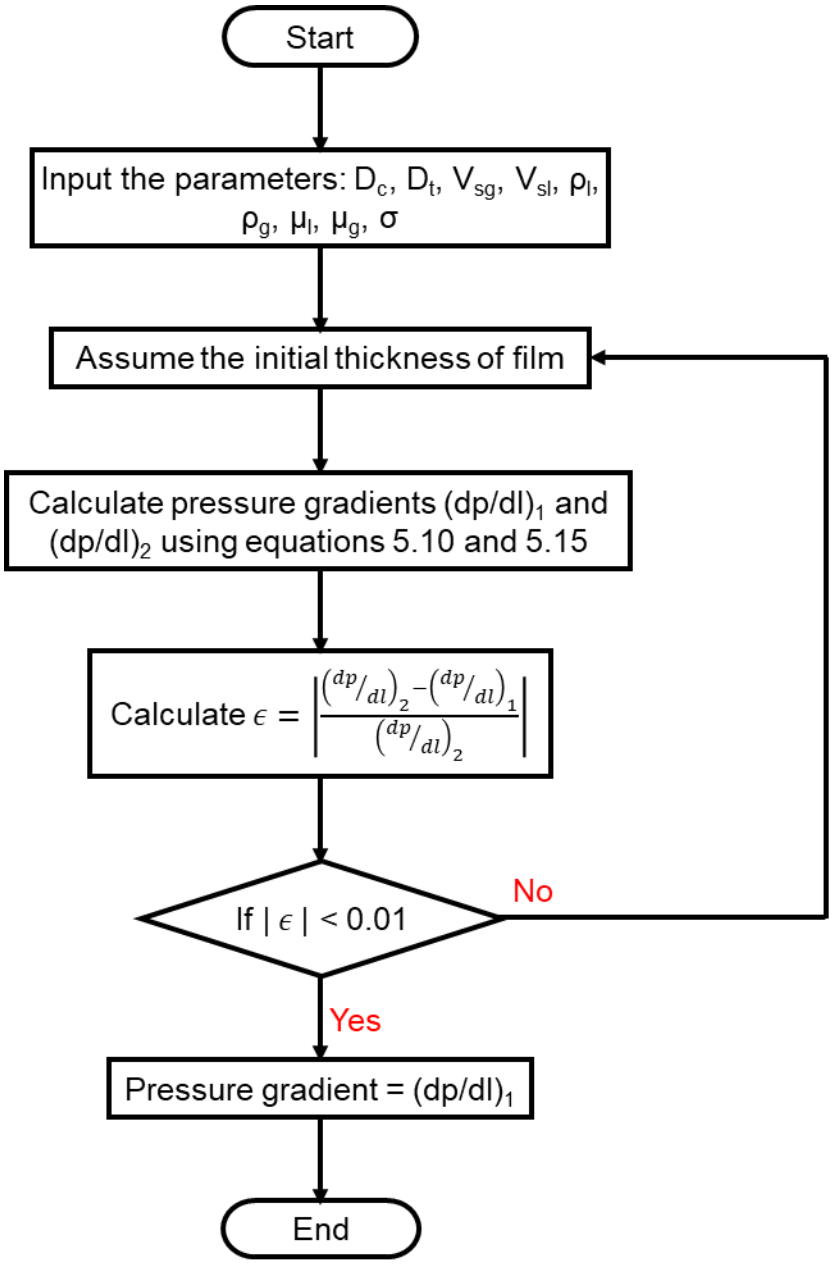

Figure 5.6 Flow chart for pressure gradient calculation of annular flow pattern in the annulus

5.4.4.1 Model Validation

The proposed model is validated using the current laboratory experimental data. Figures 5.7a, 5.7b, and 5.7c show the comparison of the predicted and measured pressure drop with respect to the superficial gas velocity corresponding to the liquid flow rate of 77.5, 155, and 227.1 liters per minute (LPM). In the calculation of the superficial liquid velocity, the pressure and temperature were incorporated. The liquid density is assumed to be 995 kg/m^3. The surface tension was assumed as 0.072 N/m. The viscosity of air and water were assumed to be 0.0000181 and 0.00062 Pa-s, respectively. The average superficial liquid velocity corresponding to 77.5, 155.0, and 227.1 LPM flow rate was 0.294 m/s, 0.579 m/s, and 0.877 m/s. The pressure gradient calculated from the modified model showed the increasing trend similar to the experimental results. The average absolute error using this model was less than 15%. The modeling results were compared with the past models developed by Lage and Time (2000). It has also been noticed that with an increase in superficial liquid velocity, the error percentage increases which can be attributed to the presence of churn characteristics of the flow. The results also suggest that without incorporation of the entrainment and geometrical effect in the friction pressure calculation leads to the absolute error of 30%.

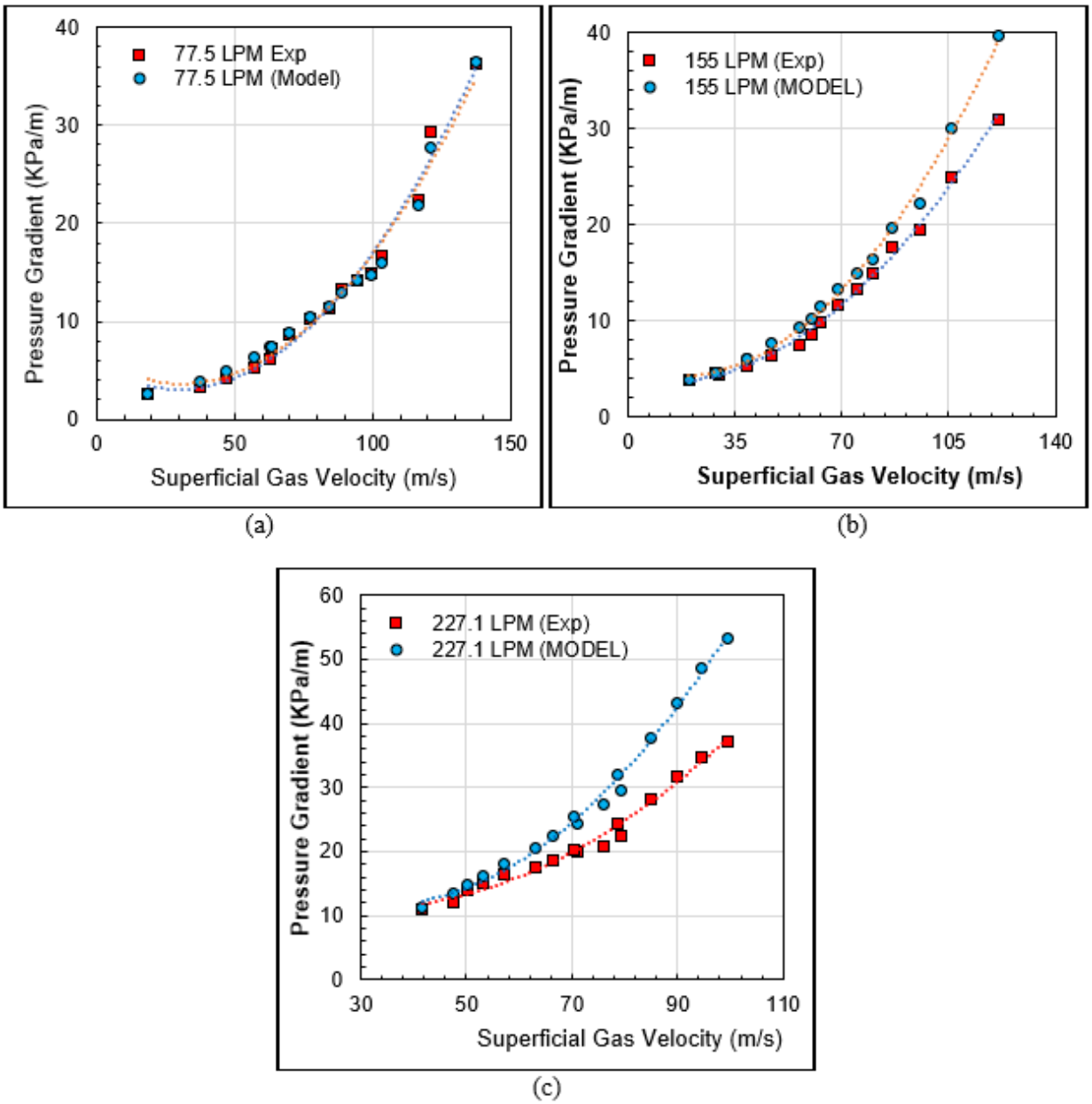

Figure 5.7 Comparison of measured and predicted pressure gradient for annular flow at three different liquid flow rates (a) 77.5 LPM, (b) 155 LPM, and (c) 227.1 LPM

Figure 5.8 shows the comparison of the predicted and measured pressure gradients for annular flow regime data. The average error in the predicted values are 12.5%, and the absolute average error is 14.5 %. With the high range of superficial gas velocity (20-137 m/s) included in this study, it can be considered a good agreement.

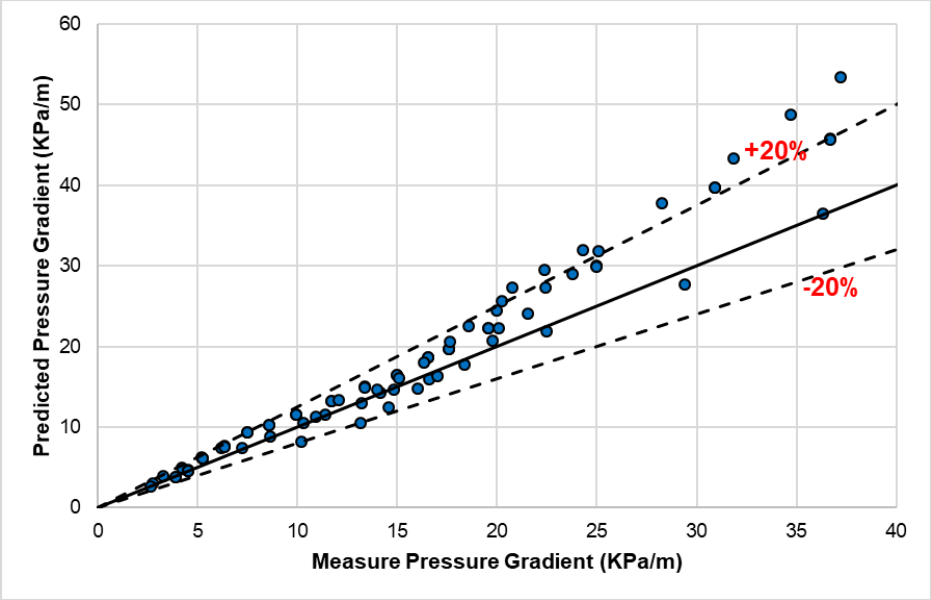

Figure 5.8 Comparison of measured and predicted pressure gradient for annular flow regime

5.5 Sonic Condition Determination Model

Sonic condition is one of the most important parameters for the construction of the WCD tool. The sonic conditions are mainly depicted in terms of speed of sound. It is a well-established fact that the speed of sound depends on the properties of the medium of fluid flow. Hence, to construct a robust model for WCD estimation, a new correlation was developed for sonic velocity calculation using the past experimental work. The new correlation combines the two existing models from Kieffer (1977) and Wilson and Roy (2008) which were validated by the static two-phase mixture experiments. The new model predicts the sonic velocity based on the volumetric gas fraction and upstream pressure. The calculated sonic velocity acts as the criterion for a sonic boundary. The fluid velocity for each grid is compared with the calculated sonic velocity for that grid. Whenever the sonic velocity matches the fluid velocity in that grid, the sonic condition establishes in the wellbore section. After that, the flow decouples from the previous grid, and the flow is limited by the sonic condition, where the well flow pressure is calculated using the sonic velocity.

Below is the model for prediction of the velocity of sound in two-phase flow. It is divided into two cases.

$$V_{sound} = \begin{cases} (a_1 P^{b_1})x^2 - (a_2 P^2 + b_2 P + c_2)x + a_3 P^{b_3} + 20 \quad for\ P \geq 100\ bar \\ (a_{11} P^{b_{11}})x^2 - (a_{21} P^2 + b_{21} P + c_{21})x + a_{31} P^{b_{31}} + 20 \quad for\ P < 100\ bar \end{cases} \tag{5.20}$$

where P is the pressure in bar, V_{sound} is the velocity of sound in m/s, a_1 = 80.44, a_2 = - 0.0607, a_3 = 30.52, b_1 = 0.6337, b_2 = 23.23, b_3 = 0.672, c_2 = 74.42, a_{11} = 1800, a_{21} = -0.0002878, a_{31} = 220.4, b_{11} = -0.01989, b_{21} = 0.8032, b_{31} = 0.2486, c_{21} = 1884, and x is volumetric fraction of gas given by the following formula:

$$x = \frac{V_{sg}}{V_{sg}+V_{sl}} \tag{5.21}$$

where V_{sg} is the superficial gas velocity, and V_{sl} is the superficial liquid velocity.

Furthermore, the new correlation was validated using the current two-phase flow experimental data. The comparative analysis of new correlation and experimental data shows reasonable agreement. Figure 5.9 shows the comparison of the experimental result and predicted value of sonic velocity using the developed model.

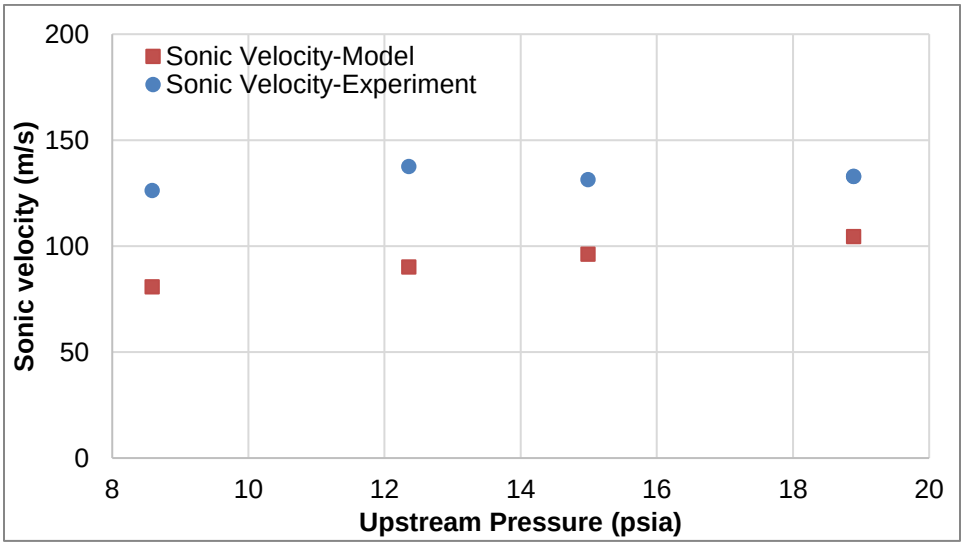

Figure 5.9 Comparison of sonic velocity from model and OU experimental data with respect to upstream pressure

5.6 Validation of WCD Tool

It is necessary to validate the WCD computational tool before implementing in operation. In order to validate the WCD tool, different cases were simulated using the commercial software package Prosper. Prosper software works on the concept of nodal analysis specifically designed for production operations. It includes simulation of inflow performance relationship (IPR) and vertical lift performance (VLP) curves. IPR curves are generated using the Darcy reservoir model for infinite radius. VLP curves are constructed using different correlation-based models such as Hagedorn Brown (HB), Beggs and Brill (BB), Mukherjee Brill (MB), Fancher Brown (FB), Duns and Ros (DR), Petroleum Experts (PE), and Petroleum Experts 2 (PE 2). In addition, the bubble point pressure can be obtained using Glasø method (Glasø, 1980). The viscosity was calculated using Beggs et al. method. The results from the commercial package were compared with the results obtained from the WCD tool. The parameters for the first case study simulated using different correlations in Prosper software are presented in Table 5.4 as shown below.

Table 5.4 Parameters used in Prosper software

Parameters	Value	Unit
Oil Gravity	28	^{o}API
Gas specific gravity	0.6	
Bubble point pressure	1404	psi
Reservoir pressure	7500	psi
Gas oil ratio	235	scf/STB

The operational flow rates were obtained using different correlations. The operating liquid flow rate and bottom hole pressure are not significantly different using different correlations. Therefore, a comparison can be made between the flow rates obtained from different correlations and the WCD rate calculated from the newly developed tool. Four cases were simulated for the comparative analysis. The input parameters for these four cases are presented in Table 5.5.

Table 5.5 Input parameters for simulated case studies

Case	Oil Gravity	Gas specific gravity	Bubble Point Pressure	Reservoir Pressure	GOR
	°API		(psi)	(psi)	scf/STB
1	28	0.6	1403.6	7500	235
2	35	0.8	2000	3000	650
3	45	0.8	2165	3000	865
4	55	0.82	2560	3000	1376

The four case studies were simulated using the correlations, and the results are shown in Figure 5.7.

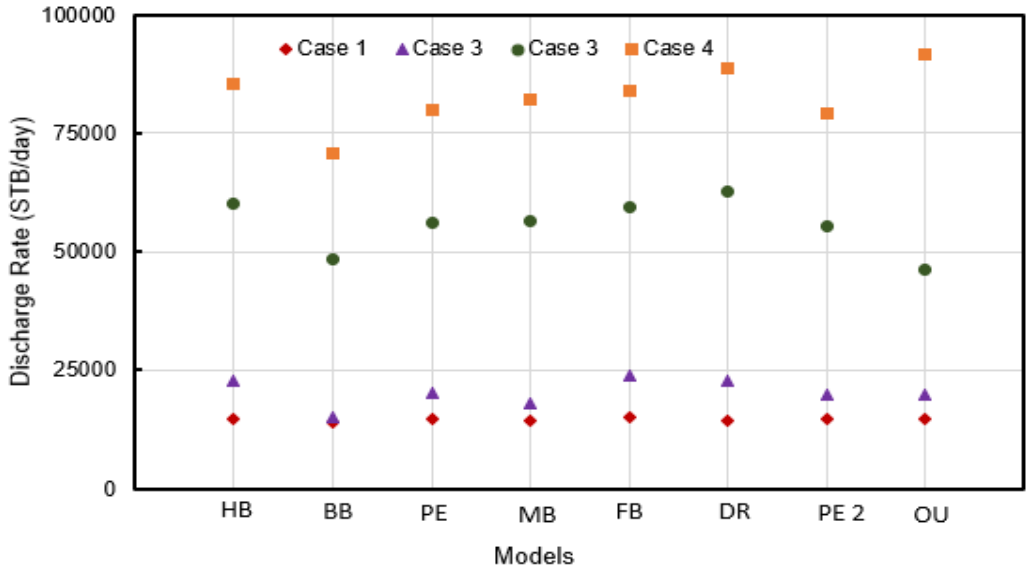

Figure 5.10 Discharge rate corresponding to different correlations and WCD tool

Note: HB: Hagedorn Brown, BB: Beggs and Brill, PE: Petroleum Experts, MB: Mukherjee and Brill, FB: Francis Brown, DR: Duns and Ros, PE 2: Petroleum Experts 2, and OU: New WCD tool.

The results suggest that the maximum difference between the most conservative results (of all correlations) and the WCD tool is 19.1%. The difference can be attributed to the model used in the current study. With this validation, several cases were simulated by varying the different input parameters in the WCD tool. The input parameters for sensitivity analysis included reservoir permeability, bottom depth, pay zone height, reservoir pressure, and skin factor. The results of the

sensitivity analysis suggest that the WCD rate increases with an increase in permeability and pay zone height and reaches a steady state after the specific increment. The steady state can be attributed to the balancing effect of reservoir properties and the pressure loss in the wellbore. In addition, as the pay zone bottom depth and skin factor increases, the discharge rate decreases.

5.7 Chapter Summary

The lack of a comprehensive tool for estimation of worst-case discharge is the main motive behind this dissertation work. One of the main limitations is the difficulty of integrating the reservoir conditions with wellbore conditions. In this work, an integrated reservoir and hydrodynamic tools have been developed to calculate the WCD during the loss of well control incidents. The accuracy of WCD prediction is strongly related to the accuracy of the hydrodynamic models. Hence, different mechanistic and empirical models for pressure gradient calculations are tested considering various flow patterns. It is worth mentioning that these models were developed for low superficial gas velocity conditions and had never been tested for high flow rates. Thus, experimental data from the current study is used to validate the incorporated models.

It should be noted that the current tool does not incorporate the flow in the annulus scenario. However, various mechanistic models are tested for different flow regimes. The current models do not show consistent results for annular flow regime; hence, a modified mechanistic model is proposed which incorporates the liquid entrainment in the gas core. The results show a good agreement with experimental measurements for high velocity conditions. Furthermore, a sonic correlation is developed based on the existing experimental data available in the literature. The new correlation shows a good agreement with the laboratory data.

The WCD computational tool is verified with the existing industry software (Prosper) using a base case scenario. The maximum difference between the software result and the current prediction is within 20%. In addition, various in-situ parameters such as reservoir permeability, bottom depth, pay zone height, reservoir pressure, and skin factor were used for sensitivity analysis of the tool. The results showed the expected trend for discharge rate with the change in the parametric values.

Chapter 6: Summary, Conclusions, and Recommendations

6.1 Summary

A comprehensive review of existing work is conducted to facilitate the understanding of the multiphase flow relevant to fluid dynamics in well control incidents. The fluid dynamics in well control incidents are related to the worst-case discharge (WCD) rate. Hence, an effort has been made to understand the challenges in experimental and theoretical work in the context. The review suggests that the effect of velocities, geometry, and fluid properties, setting up of governing equations, and an approach for solving these equations play a significant role in tackling the fluid dynamics problem in the loss of well control incidents. Different approaches such as empirical, analytical and mechanistic models are reviewed while addressing this multiphase problem.

In addition, computational fluid dynamics study has been performed using ANSYS Fluent to characterize the multiphase flow in the annulus. Mesh sensitivity analysis in the quarter sectioned annulus has been used to optimize mesh sizes required for simulation. Furthermore, different multiphase models (VOF and Eulerian Hybrid) and turbulence models (realizable k-ε and SST k-ω) were used to conduct the simulation for experimental data. The VOF models showed considerable agreement with the experimental data. Furthermore, high Mach number (Ma > 0.3) flows were simulated considering the effects of compressibility on the flow characteristics.

An extensive experimental investigation has been conducted for pipe and annulus. The pressure gradient, liquid holdup, and flow patterns are the main parameters under investigation varying superficial gas and liquid velocities. Most of the past experimental studies have considered the lower range of the velocities. However, in this study, a higher range of velocities are considered during this investigation.

This study also presents a holistic integrated tool for worst-case discharge estimation. Various models for simulation of multiphase flow in pipe and annulus were validated using the experimental data. An in-depth study of mechanistic models for flow in the annulus was conducted. Sonic conditions for multiphase flow were also investigated during this study.

6.2 Conclusions

The following conclusions can be drawn from this study:

1. This study is focused on pressure gradient and liquid holdup characterization for multiphase flow in annulus and pipe geometry. Previous studies have only reported that the pressure gradient first decreases and then increases with respect to an increase in superficial gas velocity. None of the experimental measurements have captured the pressure gradient phenomenon at extremely high superficial gas velocity. In this study, a unique trend of the pressure gradient is observed where the pressure gradient increases to the maximum and then sharply decreases at extremely high superficial gas velocity.
2. A holistic computational tool for worst-case discharge was developed which integrates the multilayered reservoir flow with the hydrodynamic models for fluid flow in the pipe. The computational tool was validated with the commercially available software Prosper. In addition, a sensitivity analysis was conducted on different parameters such as permeability, pay zone height and depth, skin factor. The worst-case discharge rate increases with an increase in permeability and reaches a plateau after a certain increase.
3. Various mechanistic models were studied and tested for different flow regimes in the annulus. The best-suited models were identified for different flow regimes. Past models showed good agreement for bubble, slug, and dispersed bubble flow regime. However, a modified mechanistic model has been developed to characterize the pressure drop for the

annular flow regime in the vertical annulus. As contrary to the assumptions in the past works, the model showed a significant effect of entrainment of liquid droplets in the gas core. The modified model incorporates the effect of entrainment of liquid droplets in the gas core and shows a good agreement.

4. A new sonic velocity correlation based on upstream pressure and the void fraction was developed to determine the sonic condition during the multiphase flow. The experiments were conducted to determine the sonic velocity in the multiphase flow. The new correlation showed good agreement with the experimental result.
5. Experiments were conducted to capture the data for pressure regime and liquid holdup in the vertical annulus and pipe at the high superficial gas velocity (5-150 m/s). The pressure gradient data was used for verification of the hydrodynamic models used in the WCD computational tool. Apart from the pressure gradient, flow regimes were identified using photographic images. There were mainly two types of flow regimes observed at such high gas velocity: (a) Churn and (b) Annular. The churn flow showed a chaotic flow structure and oscillatory nature, while in the case of the annular flow regime, the flow is streamlined. At the higher superficial gas velocities (>100 m/s), the liquid films on the wall are destroyed by the gas core, and flow becomes gas dominated with entrained liquid droplets. The pressure gradient data exhibited an increasing trend with an increase in superficial gas velocity and liquid velocity. It also tends to shape in the asymptotic form at very high superficial gas velocity. The liquid holdup decreases with an increase in superficial gas velocity while shows an increasing trend with increasing liquid velocity. The liquid holdup decreases asymptotically at higher gas velocity.

6. CFD simulation studies on two-phase flow characteristics in a concentric annulus were conducted. Ten experimental data were simulated varying superficial gas and liquid velocities. Two turbulence models realizable k-ε and shear stress transport (SST) k-ω models, coupled with the volume of fluid (VOF) model were used to predict the pressure drop and void fraction in the flow domain. It can be inferred that the realizable k-ε model performs better at low superficial gas velocities (less than 19 m/s) in predicting void fraction, while the SST k-ω model showed better accuracy at high velocities (greater than 28 m/s).
7. Also, the probability density functions (PDFs) were generated to identify the flow regimes. The churn flow regime showed distributed single peak in PDF at the higher end of void fraction. The annular flow regime showed a single peak in PDFs and displayed similar characteristics as previously reported for pipe flow. Hence, it is worthy to note that the PDFs of void fractions from CFD simulations can be used to identify the annular and churn flow regimes, which is otherwise difficult to quantify by looking at void fraction distribution in the annulus at the end of the simulation. Moreover, at high superficial gas velocities (more than 47 m/s), the flow becomes gas dominated. The gas phase interpenetrates and erodes the liquid film of the wall, and consequently, the film gets destroyed with an increase in superficial gas velocity.

6.3 Recommendations

Following recommendations have been suggested for the future work in this area of research.

1. High-velocity multiphase flow experiments for higher diameter pipe and annulus size is highly desirable to validate the hydrodynamic models further. Sonic conditions were not captured

during the experiment for the annulus geometry. Hence, the experiments with further increment in superficial gas velocities in the annulus will improve the current modeling effort.

2. The temperature profile in the wellbore is considered using the thermal gradient of the near-wellbore region. A heat transfer model will improve the accuracy of the model.
3. The scope of this study is limited to wellbore flow modeling; however, more sophisticated models for reservoir flow characterization can be implemented. The reservoir models used in this study are based on steady-state assumptions. Hence a transient model will also improve the accuracy of the computational tool.
4. A probabilistic model for reservoir data can also be implemented to capture the uncertainty in the reservoir conditions during well control incidents.

Nomenclature

A_c	Area of the gas core
A_g	Gas inlet area
AN	Annular
A_t	Cross-sectional area of the annulus
A_{total}	Total area of the inlet cross-section
BB	Bubble
CFD	Computational fluid dynamics
CH	Churn
DAQ	Data acquisition
DB	Dispersed bubble
D_e	Effective diameter (m)
D_c	Inner diameter of the outer pipe of the annulus/casing
D_h	Hydraulic diameter
D_T	Outer diameter of the inner pipe of the annulus/tubing
E_{avg}	Percentage average error
E_{aavg}	Percentage absolute average error
E_i	Error in pressure gradient for i^{th} data
f	Fanning friction factor
$\vec{F}$	External body forces
Fe	Entrained liquid fraction in the gas core
f_1, f_2, and f_μ	Wall damping function
$\vec{g}$	Acceleration due to gravity

H_l	Liquid holdup
I	Unit tensor
ID	Inner diameter
K	Casing-tubing diameter ratio
L	Length of the test section (m)
LPM	Liters per minute
$\dot{m}_{ij}$	Mass transfer from phase i to j
$\dot{m}_{ji}$	Mass transfer from phase j to i
OD	Outer diameter
p	Static pressure
PDF/pdf	Probability density function
$P_{g,calc}$	Calculated pressure gradient
$P_{g,meas}$	Measured pressure gradient
$\left(\frac{dp}{dl}\right)_1$	Pressure gradient for gas core
$\left(\frac{dp}{dl}\right)_2$	Overall pressure gradient
Re	Reynolds number
r_m	Point of zero shear stress
RNG	Re-normalized group
S	Slip ratio
S_{CW}	Wetted liquid perimeter on the casing wall
S_{ci}	Wetted liquid perimeters on casing (outer pipe) wall film-gas core interface
SL	Slug
$S_{\alpha i}$	Source term

SST	Shear stress transport
S_{ti}	Wetted liquid perimeters on tubing (inner pipe) wall film-gas core interface
S_{TW}	Wetted liquid perimeter on the tubing wall
U_i', U_j'	Reynold stresses
V	Velocity (m/s)
VFD	Variable frequency drives
V_m	Mixture velocity (m/s)
$\overline{V_m}$	Mean velocity (m/s)
VOF	Volume of fluid
V_{sgin}	Simulation inlet gas velocity
V_{sg}	Superficial gas velocity
V_{sl}	Superficial liquid velocity

Greek Symbols

$\bar{\bar{\tau}}$	Stress tensor
μ	Molecular viscosity
μ_T	Turbulent viscosity
ρ_i	Density of i^{th} phase
α_i	Volume fraction of i^{th} phase
σ	Surface tension
ρ	Density (kg/m^3)
ε	Roughness height (m)
ρ_l	Liquid density (kg/m^3)
ρ_g	Gas density (kg/m^3)

α	Gas void fraction
$\alpha_{entrainment}$	Entrainment fraction of liquid in the gas core
α_l	Liquid fraction
α_g	Gas fraction
δ	Dimensionless film thickness
μ_g	Viscosity of the gas
μ_l	Viscosity of the liquid
τ_{ci}	Shear stresses at casing (outer pipe) wall film-gas core interface
τ_{ti}	Shear stresses at tubing (inner pipe) wall film-gas core interface

References

1. Abdulkadir, M., Hernandez-Perez, V., Lo, S., Lowndes, I.S. and Azzopardi, B.J., 2015. Comparison of experimental and Computational Fluid Dynamics (CFD) studies of slug flow in a vertical riser. Experimental Thermal and Fluid Science, 68, pp.468-483.

2. Aggour, M. A., & Al-Yousef, H. Y. 1996. Vertical Multiphase Flow Correlations for High Production Rates and Large Tubulars. (1996, February 1). Society of Petroleum Engineers. doi:10.2118/28465-PA.

3. Ali, S. F. 2009. Two Phase Flow in Large Diameter Vertical Riser. PhD Dissertation. Cranfield University, School of Engineering Department of Process and Systems Engineering.

4. Ali, S.F. and Yeung, H., 2014. Two-phase flow patterns in large diameter vertical pipes. Asia-Pacific Journal of Chemical Engineering, 9(1), pp.105-116.

5. Ansari, A. M., Sylvester, N. D., Sarica, C., Shoham, O., & Brill, J. P. (1994, May 1). A Comprehensive Mechanistic Model for Upward Two-Phase Flow in Wellbores. Society of Petroleum Engineers. doi:10.2118/20630-PA.

6. Araújo, J.D.P., Miranda, J.M. and Campos, J.B.L.M., 2013. Flow of two consecutive Taylor bubbles through a vertical column of stagnant liquid—A CFD study about the influence of the leading bubble on the hydrodynamics of the trailing one. Chemical Engineering Science, 97, pp.16-33.

7. Asheim, H. (1986, May 1). MONA, An Accurate Two-Phase Well Flow Model Based on Phase Slippage. Society of Petroleum Engineers. doi:10.2118/12989-PA.

8. Awad, M. M., & Muzychka, Y. S. 2010. Two-phase Flow Modeling in Microchannels and Minichannels. Heat Transfer Engineering, 31(13), pp.1023-1033.

9. Aziz, K., Govier, G. W., & Fogarasi., M. (1972, July 1). Pressure Drop in Wells Producing Oil and Gas. Petroleum Society of Canada. doi:10.2118/72-03-04.

10. Barati, R. and Liang, J.T., 2014. A review of fracturing fluid systems used for hydraulic fracturing of oil and gas wells. Journal of Applied Polymer Science, 131(16).

11. Barnea, D. and Shemer, L. 1986. Rise Velocity of Large Bubbles in Stagnant Liquid in Non-circular Ducts. International journal of multiphase flow, 12(6), pp.1025-1027.

12. Baxendell, P. B., & Thomas, R. (1961, October 1). The Calculation of Pressure Gradients in High-Rate Flowing Wells. Society of Petroleum Engineers. doi:10.2118/2-PA

13. Beggs, D. H., & Brill, J. P. (1973, May 1). A Study of Two-Phase Flow in Inclined Pipes. Society of Petroleum Engineers. doi:10.2118/4007-PA

14. Bendat, J.S. and Piersol, A.G., 2011. Random data: analysis and measurement procedures (Vol. 729). John Wiley & Sons.

15. Berthelsen, P.A. and Ytrehus, T., 2005. Calculations of stratified wavy two-phase flow in pipes. International Journal of Multiphase Flow, 31(5), pp.571-592.

16. Bhagwat, S.M. and Ghajar, A.J., 2014. A flow pattern independent drift flux model based void fraction correlation for a wide range of gas–liquid two phase flow. International Journal of Multiphase Flow, 59, pp.186-205.

17. Bijleveld, A. F., Koper, M., & Saponja, J. (1998, January 1). Development and Application of an Underbalanced Drilling Simulator. Society of Petroleum Engineers. doi:10.2118/39303-MS.

18. Blake, K. W., Bourgeois, D. J., Howard, D. C., & Schoennagel, C. J. (October, 1988). Investigation of September 1984 Blowout and Fire Lease OCS-G 5893, Green Canyon Block 69 Gulf of Mexico, Off the Louisiana Coast, OCS Report 86-0101, U. S. Department of the Interior/ Mineral Management Service.

19. Bowman, S. (2012, September 1). Altering an Existing Well Design to Meet New BOEMRE Worst-Case Discharge Criteria. Society of Petroleum Engineers. doi:10.2118/161929-PA

20. Bowman, A.W. and Azzalini, A., 1997. Applied smoothing techniques for data analysis: the kernel approach with S-Plus illustrations (Vol. 18). OUP Oxford.

21. Brackbill, J.U., Kothe, D.B. and Zemach, C., 1992. A continuum method for modeling surface tension. Journal of computational physics, 100(2), pp.335-354.

22. Brown, R.A.S., Sullivan, G.A., & Govier, G.W., 1960. The Upward Vertical Flow of Air-water Mixtures: III. Effect of Gas Phase Density on Flow Pattern, Holdup and Pressure Drop. The Canadian Journal of Chemical Engineering, 38(2), pp.62-66.

23. Brown, K. E., & Lea, J. F. (1985, October 1). Nodal Systems Analysis of Oil and Gas Wells. Society of Petroleum Engineers. doi:10.2118/14714-PA

24. Caetano, E. F. 1985. Upward vertical two-phase flow through an annulus. Ph.D. dissertation, The University of Tulsa, Tulsa, Oklahoma.

25. Caetano, E. F., Shoham, O. O., & Brill, J. P. 1992a. Upward Vertical Two-Phase Flow Through an Annulus—Part I: Single-Phase Friction Factor, Taylor Bubble Rise Velocity, and Flow Pattern Prediction. ASME. J. Energy Resour. Technol. 1992; 114(1):1-13. doi:10.1115/1.2905917.

26. Caetano, E. F., Shoham, O. O., & Brill, J. P. 1992b. Upward Vertical Two-Phase Flow through an Annulus—Part II: Modeling Bubble, Slug, and Annular Flow. ASME. J. Energy Resour. Technol. 1992; 114(1):14-30. doi:10.1115/1.2905916.

27. Chen, P. 2004. Modeling the Fluid Dynamics of Bubble Column Flows. PhD Dissertation,

Department of Chemical Engineering, Washington University. http://citeseerx.ist.psu.edu/viewdoc/download?doi=10.1.1.469.8152&rep=rep1&type=pdf

28. Cheng, H., Hills, J.H. and Azzorpardi, B.J., 1998. A study of the bubble-to-slug transition in vertical gas-liquid flow in columns of different diameter. International Journal of Multiphase Flow, 24(3), pp.431-452.

29. CSB Report, 2016. Explosion and Fire at the Macondo Well. Investigation Report Overview, Volume 3, U.S. Chemical Safety and Hazard Investigation Board. Report No. 2010-10-I-OS

30. Da Riva, E. and Del Col, D., 2009. Numerical simulation of churn flow in a vertical pipe. Chemical Engineering Science, 64(17), pp.3753-3765.

31. Damir, G. 2012. Multiphase flow in large diameter pipes. M.S. Thesis, University of Nottingham. London, United Kingdom.

32. Dai, Y., Dakshinammorthy, D. and Agrawal, M., 2013, May. CFD Modeling of Bubbly, Slug and Annular Flow Regimes in Vertical Pipelines. In Offshore Technology Conference. Offshore Technology Conference.

33. Darcy, H. (1857). Recherches Experimentales Relatives Au Mouvement De L'eau Dans Les Tuyaux (Engl. Transl.: "Experimental Research Relating to the Movement of Water in Pipes"). Mallet−Bachelier: Paris, 2.

34. Das, G., Das, P.K., Purohit, N.K. and Mitra, A.K. 1999a. Flow Pattern Transition During Gas Liquid Upflow through Vertical Concentric Annuli—Part I: Experimental Investigations. Journal of fluids engineering, 121(4), pp.895-901.

35. Das, G., Das, P.K., Purohit, N.K. and Mitra, A.K. 1999b. Flow Pattern Transition during Gas Liquid Upflow through Vertical Concentric Annuli—Part II: Mechanistic Models. Journal of fluids engineering, 121(4), pp.902-907.

36. De Sampaio, P.A., Faccini, J.L. and Su, J., 2008. Modelling of stratified gas–liquid two-phase flow in horizontal circular pipes. International Journal of Heat and Mass Transfer, 51(11-12), pp.2752-2761.

37. Dukler, A.E., Wicks, M., & Cleveland, R.G. (1964). Frictional Pressure Drop in Two-Phase Flow: A. A Comparison of Existing Correlations for Pressure Loss and Holdup. AIChE Journal, 10(1): p. 38-43.

38. Dukler, A.E. and Taitel, Y., 1986. Flow pattern transitions in gas-liquid systems: measurement and modeling. Multiphase Science and Technology, 2(1-4).

39. Duns, H., & Ros, N. C. J. (1963, January 1). Vertical flow of gas and liquid mixtures in wells. World Petroleum Congress.

40. Eaton, B. A., Knowles, C. R., & Silberbrg, I. H. (1967, June 1). The Prediction of Flow Patterns, Liquid Holdup and Pressure Losses Occurring During Continuous Two-Phase Flow

in Horizontal Pipelines. Society of Petroleum Engineers. doi:10.2118/1525-PA

41. Eddington, R.B., Technical Report 32-1096: Investigation of Supersonic Shock Phenomena in a Two-Phase (Liquid-Gas) Tunnel. 1967, NASA-Jet Propulsion Laboratory.

42. Fetkovich, M. J. (1973, January 1). The Isochronal Testing of Oil Wells. Society of Petroleum Engineers. doi:10.2118/4529-MS.

43. Fernandes, R.C., Semiat, R. and Dukler, A.E. 1983. Hydrodynamic Model for Gas-Liquid Slug Flow in Vertical Tubes. AIChE Journal, 29(6), pp.981-989.

44. Fluent, A.N.S.Y.S., 2016a. Theory Guide 17.2. Ansys Inc. USA.

45. Fluent User Guide (Version 16.2). 2016b. ANSYS Fluent. Retrieved from http://www.ansys.com/Products/Fluids/ANSYS-Fluent (Accessed on November 16, 2018)

46. Furukawa, T. and Sekoguchi, K. 1986. Phase Distribution for Air-Water Two-Phase Flow in Annuli. Bulletin of JSME, 29(255), pp.3007-3014.

47. Gilbert, W. E. (1954, January 1). Flowing and Gas-lift Well Performance. American Petroleum Institute.

48. Glaso, O., (1980) "Generalized Pressure-Volume-Temperature Correlations" Journal of Petroleum Technology, pp. 785–795.

49. Gomez, L. E., Shoham, O., Schmidt, Z., Chokshi, R. N., & Northug, T. (2000, September 1). Unified Mechanistic Model for Steady-State Two-Phase Flow: Horizontal to Vertical Upward Flow. Society of Petroleum Engineers. doi:10.2118/65705-PA.

50. Griffith, P. & Wallis, G. B. (1961). Two-Phase Slug Flow. Journal of Heat Transfer, 1961. 83(3): p. 307-318.

51. Guo B., Lyons W.C. & Ghalambor A. (2007). Petroleum production engineering: A computer-assisted approach. Elsevier Science & Technology Books.

52. Hagedorn, A. R., & Brown, K. E. (1965, April 1). Experimental Study of Pressure Gradients Occurring During Continuous Two-Phase Flow in Small-Diameter Vertical Conduits. Society of Petroleum Engineers. doi:10.2118/940-PA.

53. Harmathy, T. Z. 1960. Velocity of Large Drops and Bubbles in Media of Infinite or Restricted Extent. AIChE Journal, 6(2), pp.281-288.

54. Harvel, G.D., Hori, K., Kawanishi, K. and Chang, J. S. 1999. Cross-sectional Void Fraction Distribution Measurements in a Vertical Annulus Two-phase Flow by High Speed X-ray Computed Tomography and Real-time Neutron Radiography Techniques. Flow Measurement and Instrumentation, 10(4), pp.259-266.

55. Hasan, A. R., & Kabir, C. S. (1988, May 1). A Study of Multiphase Flow Behavior in Vertical

Wells. Society of Petroleum Engineers. doi:10.2118/15138-PA

56. Hasan, A.R. & Kabir, C.S. (1992). Two-phase Flow in Vertical and Inclined Annuli. International Journal of Multiphase Flow, 18(2), pp.279-293

57. Hasan, A. R., Kabir, C. S., & Wang, X. (1998, June 1). Wellbore Two-Phase Flow and Heat Transfer during Transient Testing. Society of Petroleum Engineers. doi:10.2118/38946-PA

58. Henry R.E. 1968. A Study of One- and Two-component, Two-phase Critical Flows at Low Qualities, AEG Research and Development Report (ANL-7430).

59. Hernandez-Perez, V., Abdulkadir, M. and Azzopardi, B.J., 2011. Grid generation issues in the CFD modelling of two-phase flow in a pipe. The Journal of Computational Multiphase Flows, 3(1), pp.13-26.

60. Hewitt, G.F., & Roberts, D.N. A. (1969). Studies of Two-Phase Flow Patterns by Simultaneous X-Ray and Flash Photography. United Kingdom Atomic Energy, G. Research, E. Atomic Energy Research, and D. Chemical Energy. Harwell, England; [London]: Chemical Engineering Division, Atomic Energy Research Establishment; Available from H.M. Stationery Office.

61. Hewitt, G., Hall Taylor, N., 1970. Annular Two-Phase Flow. Pergamon Press, UK.

62. Hewitt, G.F. 1985. Experimental and modelling studies of annular flow in the region between flow reversal and the pressure drop minimum. Physico-Chemical Hydrodynamics, 6, pp.43-50.

63. Hibiki, T. and Ishii, M. 2002. Distribution Parameter and Drift Velocity of Drift-Flux Model in Bubbly Flow. International Journal of Heat and Mass Transfer, 45(4), pp.707-721.

64. Hibiki, T., & Ishii, M. (2003). One-dimensional drift-flux model and constitutive equations for relative motion between phases in various two-phase flow regimes. International Journal of Heat and Mass Transfer, 46(25), pp.4935-4948.

65. Hirt, C.W. and Nichols, B.D., 1981. Volume of fluid (VOF) method for the dynamics of free boundaries. Journal of computational physics, 39(1), pp.201-225.

66. Hopper, A. R. (2015). National Notice to Lessees and Operators of Federal Oil and Gas Leases and Holders of Rights-of-Use and Easements on the Outer Continental Shelf (OCS). US DOI, BOEM, NTL No. 2015-N01, 2015, January 14.

67. Hsu, Y.-Y., 1972. Review of critical Flow Rate, Propagation of Pressure Pulse, and Sonic Velocity in Two-Phase Media: NASA-Lewis Research Center.

68. Hulsurkar, P., Awoleke, O. O., and Ahmadi, M. (2018, March 1). Experimental Study of the Multiphase Flow of Sand, Viscous Oil, and Gas in a Horizontal Pipe. Society of Petroleum Engineers. doi:10.2118/187212-PA

69. Ibarra, R., Mohan, R. S., & Shoham, O. (2017, August 1). Investigation of Critical Sand-Deposition Velocity in Horizontal Gas/Liquid Stratified Flow. Society of Petroleum Engineers. doi:10.2118/168209-PA

70. Ishii, M., & Hibiki, T., 2010. Thermo-fluid dynamics of two-phase flow. Springer Science & Business Media.

71. Jones Jr, O.C. and Zuber, N. 1975. The Interrelation between Void Fraction Fluctuations and Flow Patterns in Two-phase Flow. International Journal of Multiphase Flow, 2(3), pp.273-306.

72. Julia, J. E., Ozar, B, Jeong, J., Hibiki, T., and Ishii, M. 2011. Flow Regime Development Analysis in Adiabatic Upward Two-phase Flow in a Vertical Annulus. International Journal of Heat and Fluid Flow 32 pp 164–175.

73. Julia, J. E. and Hibiki, T. 2011. Flow Regime Transition Criteria for Two-Phase Flow in a Vertical Annulus. International Journal of Heat and Fluid Flow, 32(5), pp.993-1004.

74. Kabir, C.S., & Hasan A.R. (1990). Performance of a Two-phase Gas/Liquid Flow Model in Vertical Wells, In Journal of Petroleum Science and Engineering, Volume 4, Issue 3, 1990, Pages 273-289, ISSN 0920-4105, https://doi.org/10.1016/0920-4105(90)90016-V.

75. Kawanishi, K., Hirao, Y. and Tsuge, A., 1990. An experimental study on drift flux parameters for two-phase flow in vertical round tubes. Nuclear engineering and design, 120(2-3), pp.447-458.

76. Kelessidis, V. C. and Dukler, A. E. 1989, Modelling Flow Pattern Transitions for Upward Gas-Liquid Flow in Vertical Concentric and Eccentric Annuli, International Journal of Multiphase Flow, 15: 173-191.

77. Kelessidis, V. C. and Dukler, A. E. 1990. Motion of Large Gas Bubbles Through Liquids in Vertical Concentric and Eccentric Annuli. International Journal of Multiphase Flow, 16(3), pp.375-390.

78. Kiran, R. and Salehi, S., 2018, June. Mathematical modeling and analysis of riser gas unloading problem. In ASME 2018 37th International Conference on Ocean, Offshore and Arctic Engineering (pp. V008T11A063-V008T11A063). American Society of Mechanical Engineers.

79. Kieffer, S.W. 1977. Sound speed in liquid-gas mixtures: Water-air and water-steam. Journal of Geophysical Research, 82(20), pp.2895-2904.

80. Krehl, P.E.T.E.R. 2000. History of shock waves. Handbook of Shock Waves (Edited by G. Ben-Dor, O. Igra, and T. Elperin), 1, pp.1-142.

81. Lam, C.K.G. and Bremhorst, K., 1981. A modified form of the k-ε model for predicting wall turbulence. Journal of fluids engineering, 103(3), pp.456-460.

82. Lage, A. C. V. M., & Time, R. W. (2000, January 1). Mechanistic Model for Upward Two-Phase Flow in Annuli. Society of Petroleum Engineers. doi:10.2118/63127-MS

83. Laufer, J., 1954. The structure of turbulence in fully developed pipe flow. NACA Report 1174.

84. LedaFlow Software 2016; Available from: http://www.kongsberg.com/en/kogt/products%20and%20services/flow%20assurance/ledaflo w%20software/

85. Lien, K., Monty, J.P., Chong, M.S. and Ooi, A., 2004, December. The entrance length for fully developed turbulent channel flow. In 15th Australian fluid mechanics conference (Vol. 15, pp. 356-363)

86. Liu, T.J., 1998, June. The role of bubble size on liquid phase turbulent structure in two-phase bubbly flow. In Proc. Third International Congress on Multiphase Flow ICMF (Vol. 98, pp. 8-12).

87. Liu, H., Vandu, C.O., & Krishna, R. (2005). Hydrodynamics of Taylor Flow in Vertical Capillaries: Flow Regimes, Bubble Rise Velocity, Liquid Slug Length, and Pressure Drop. Industrial & Engineering Chemistry Research, 44(14): p. 4884-4897.

88. Liu, R., A.R. Hasan, and S. 2014. Mannan, Flow Rate and Total Discharge Estimations in Gas-Well Blowouts, Society of Petroleum Engineers.

89. Lockhart, R.W. and Martinelli, R.C., 1949. Proposed Correlation of Data for Isothermal Two-phase, Two-component Flow in Pipes. Chem. Eng. Prog, 45(1), pp.39-48.

90. López, J., Pineda, H., Bello, D. and Ratkovich, N., 2016. Study of liquid–gas two-phase flow in horizontal pipes using high speed filming and computational fluid dynamics. Experimental Thermal and Fluid Science, 76, pp.126-134.

91. Lucas, D., Krepper, E. and Prasser, H.M., 2005. Development of co-current air–water flow in a vertical pipe. International Journal of Multiphase Flow, 31(12), pp.1304-1328.

92. Lun, I., Calay, R.K. and Holdo, A.E., 1996. Modelling two-phase flows using CFD. Applied Energy, 53(3), pp.299-314.

93. Matsui, G., 1986. Automatic identification of flow regimes in vertical two-phase flow using differential pressure fluctuations. Nuclear Engineering and Design, 95, pp.221-231.

94. Martinelli, R.T. & Nelson, D.B. (1948). Prediction of Pressure Drop During Forced Circulation Boiling of Water. Trans. ASME, 70(6), pp.695-702.

95. Mcquillan, K.W., & Whalley, P. B. (1985). Flow Patterns in Vertical Two-Phase Flow. International Journal of Multiphase Flow, 11(2): p. 161-175.

96. Menter, F.R., 1994. Two-equation eddy-viscosity turbulence models for engineering

applications. AIAA Journal, 32(8), pp.1598-1605.

97. Mishima, K. and Ishii, M., 1984. Flow Regime Transition Criteria for Upward Two-phase Flow in Vertical Tubes. International Journal of Heat and Mass Transfer, 27(5), pp.723-737.

98. Moyer, M. C., Lewis, S. B., Cotton, M. T., & Peroyea, M. (2012, January 1). Challenges Associated With Drilling a Deepwater, Subsalt Exploration Well in the Gulf of Mexico: Hadrian Prospect. Society of Petroleum Engineers. doi:10.2118/154928-MS

99. Mukherjee, H. & Brill, J.P. (1985). Pressure drop correlations for inclined two-phase flow. Journal of energy resources technology, 107(4), pp.549-554. doi:10.1115/1.3231233.

100. Muzychka, Y.S. and Awad, M.M., 2010. Asymptotic Generalizations of the Lockhart–Martinelli Method for Two Phase Flows. Journal of Fluids Engineering, 132(3), p.031302.

101. Nikuradse, J., 1933. Gesetzmäßigkeiten der turbulenten Strömung in glatten Rohren (Nachtrag). Forschung im Ingenieurwesen, 4(1), pp.44-44.

102. Nguyen, D.L., Winter, E.R.F. & Greiner, M. (1981). Sonic Velocity in Two-phase Systems. International Journal of Multiphase Flow, 7(3), pp.311-320.

103. Ohnuki, A. & Akimoto, H., 1996, An experimental study on developing air-water two-phase flow along a large vertical pipe: effect of air injection method. Int. J. Multiphase Flow, Vol. 22, No. 6, 1996, pp. 1143-1154.

104. Ohnuki, A. & Akimoto, H., 2000, Experimental study on transition of flow pattern and phase distribution in upward air-water two-phase flow along a large vertical pipe. Int. J. Multiphase Flow, Vol. 26, 2000, pp. 367-386.

105. OLGA Dynamic Multiphase Flow Simulator. 2016; Available from: https://www.software.slb.com/products/olga

106. Omebere-Iyari, N.K., Azzopardi, B.J. and Ladam, Y., 2007. Two-phase flow patterns in large diameter vertical pipes at high pressures. AIChE journal, 53(10), pp.2493-2504.

107. Omebere-Iyari, N.K., Azzopardi, B.J., Lucas, D., Beyer, M. and Prasser, H.M., 2008. The characteristics of gas/liquid flow in large risers at high pressures. International journal of multiphase flow, 34(5), pp.461-476.

108. Orkiszewski, J. (1967, June 1). Predicting Two-Phase Pressure Drops in Vertical Pipe. Society of Petroleum Engineers. doi:10.2118/1546-PA.

109. Oudeman, P., Baaijens, M. N., & Avest, D. (1993, January 1). Modelling Blowout Control by Means of Downhole Kill Fluid Injection. Society of Petroleum Engineers. doi:10.2118/26732-MS

110. Oudeman, P., Kerem, M., 2006. Transient Behavior of Annular Pressure Buildup in HP/HT Wells. SPE Drill. Complet. 21 (4), 234-241. http://dx.doi.org/10.2118/88735-PA.

111. Oudeman, P. (2010, September 1). Validation of Blowout-Rate Calculations for Subsea Wells. Society of Petroleum Engineers. doi:10.2118/115019-PA

112. Ozar, B., Jeong, J. J., Dixita, A., Juliá, J. E., Hibiki, T., & Ishii, M. 2008. Flow Structure of Gas-Liquid Two-phase Flow in an Annulus. Chemical Engineering Science 63 (2008) pp 3998-4011

113. Pai, S.I. 2013. Two-phase Flows (Vol. 3). Springer-Verlag.

114. Papadimitriou, D. A. and Shoham, O. 1991, January. A Mechanistic Model for Predicting Annulus Bottomhole Pressures in Pumping Wells. In SPE Production Operations Symposium. Society of Petroleum Engineers.

115. Parvareh, A., Rahimi, M., Alizadehdakhel, A. and Alsairafi, A.A., 2010. CFD and ERT investigations on two-phase flow regimes in vertical and horizontal tubes. International communications in heat and mass transfer, 37(3), pp.304-311.

116. Parsi, M., Vieira, R.E., Torres, C.F., Kesana, N.R., McLaury, B.S., Shirazi, S.A., Schleicher, E. and Hampel, U., 2015. Experimental investigation of interfacial structures within churn flow using a dual wire-mesh sensor. International Journal of Multiphase Flow, 73, pp.155-170.

117. Parsi, M., Agrawal, M., Srinivasan, V., Vieira, R.E., Torres, C.F., McLaury, B.S., Shirazi, S.A., Schleicher, E. and Hampel, U., 2016. Assessment of a hybrid CFD model for simulation of complex vertical upward gas–liquid churn flow. Chemical Engineering Research and Design, 105, pp.71-84.

118. Per Holland. (2017). Loss of Well Control Occurrence and Size Estimators, Phase I and II. BSEE Report no. ES201471/2.

119. Poettman, F. H., & Carpenter, P. G. (1952, January 1). The Multiphase Flow of Gas, Oil, and Water through Vertical Flow Strings with Application to the Design of Gas-lift Installations. American Petroleum Institute.

120. Replogle, D.R., Bp: Regional Oil Spill Response Plan - Gulf of Mexico: Appendix H-Worst Case Discharge. 2009.

121. Rouhani, S.Z. and Axelsson, E., 1970. Calculation of Void Volume Fraction in the Subcooled and Quality Boiling Regions. International Journal of Heat and Mass Transfer, 13(2), pp.383-393.

122. Rozenblit, R., Gurevich, M., Lengel, Y., & Hetsroni, G., 2006. Flow Patterns and Heat Transfer in Vertical Upward Air–water Flow with Surfactant. International Journal of Multiphase Flow, 32(8), pp.889-901.

123. Rui, S.Z. and Xing, Y.M., 2011, March. Numerical simulation of two-phase flow with evaporation in supersonic cross flow. In Power and Energy Engineering Conference (APPEEC), 2011 Asia-Pacific (pp. 1-4). IEEE.

124. Rzehak, R. and Kriebitzsch, S., 2015. Multiphase CFD-simulation of bubbly pipe flow: A code comparison. International Journal of Multiphase Flow, 68, pp.135-152.

125. Sadatomi, M., Sato, Y. and Saruwatari, S. 1982. Two-phase flow in vertical noncircular channels. International Journal of Multiphase Flow, 8(6), pp.641-655.

126. Sanati, A. 2015. Numerical Simulation of Air–water Two–phase Flow in Vertical Pipe using k-ε Model. International Journal of Engineering & Technology, 4 (1) (2015) 61-70.

127. Sawai, T., Kaji, M., Kasugai, T., Nakashima, H., & Mori, T. 2004. Gas–liquid interfacial structure and pressure drop characteristics of churn flow. Experimental Thermal and Fluid Science, Vol. 28, 597-606.

128. Schlegel, J., Hibiki, T. and Ishii, M., 2010. Development of a comprehensive set of drift-flux constitutive models for pipes of various hydraulic diameters. Progress in Nuclear Energy, 52(7), pp.666-677.

129. Shen, X., R. Matsui, K. Mishima, & H. Nakamura (2010), Distribution parameter and drift velocity for two-phase flow in a large diameter pipe,Nucl. Eng. Des.,240, 3991–4000.

130. Shen, X., Mishima, K., & Nakamura, H., 2005. Two-phase phase distribution in a vertical large diameter pipe. Int. J. Heat Mass Transfer 48, 211–225.

131. Shen, X., Saito, Y., Mishima, K., Nakamura, H., 2006. A study on the characteristics of upward air–water two-phase flow in a large diameter pipe." Experimental Thermal and Fluid Science, Vol. 31. 21-36.

132. Shi, H., Holmes, J. A., Durlofsky, L. J., Aziz, K., Diaz, L., Alkaya, B., & Oddie, G. (2005, March 1). Drift-Flux Modeling of Two-Phase Flow in Wellbores. Society of Petroleum Engineers. doi:10.2118/84228-PA.

133. Shi, H., Holmes, J.A., Durlofsky, L.J., Aziz, K., Diaz, L.R., Alkaya, B. and Oddie, G., 2005, January. Drift-flux modeling of multiphase flow in wellbores. In SPE Annual Technical Conference and Exhibition. Society of Petroleum Engineers.

134. Shirdel, M., & Sepehrnoori, K. (2017, February 1). Development of transient mechanistic three-phase flow model for wellbores. Society of Petroleum Engineers. doi:10.2118/180928-PA

135. Sorgun, M., Osgouei, R. E., Ozbayoglu, M. E., and Ozbayoglu, A. M. 2011. Gas-liquid flow through horizontal eccentric annuli: CFD and experiments compared. In the Proceedings of the ASME-JSME-KSME 2011 Joints Fluids Engineering Conference, Shizuoka, Japan.

136. Sun, X., Kuran, S. and Ishii, M. 2004. Cap Bubbly-to-Slug Flow Regime Transition in a Vertical Annulus. Experiments in Fluids, 37(3), pp.458-464.

137. Taha, T. and Cui, Z.F., 2006. CFD modelling of slug flow in vertical tubes. Chemical Engineering Science, 61(2), pp.676-687.

138. Tengesdal, J. O., Sarica, C., Scmidt., Z., and Doty., D. (1999). “A Mechanistic Model for Predicting Pressure Drop in Vertical Two-Phaes Flow” Journal of Energy Resources Technology. ASME Vol 121, pp 1-8.

139. Torsvik, A., Skogestad, J. O., & Linga, H. (2017, December 1). An Experimental Study of Gas Influx in Oil-Based Drilling Fluids for Improved Modeling of High-Pressure, High-Temperature Wells. Society of Petroleum Engineers. doi:10.2118/178860-PA

140. Taitel, Y., Bornea, D. & Dukler, A.E. (1980). Modelling Flow Pattern Transitions for Steady Upward Gas-liquid Flow in Vertical Tubes. AIChE Journal, 26(3), pp.345-354.

141. Turner, J.C.R. (1966). On Bubble Flow in Liquids and Fluidised Beds. Chemical Engineering Science, 21(11), pp.971-974.

142. Venkateswararao, P., Semiat, R. and Dukler, A.E. 1982. Flow Pattern Transition for Gas-Liquid Flow in a Vertical Rod Bundle. International Journal of Multiphase Flow, 8(5), pp.509-524.

143. Venkateswaran, S., Lindau, J.W., Kunz, R.F. & Merkle, C.L., 2002. Computation of multiphase mixture flows with compressibility effects. Journal of Computational Physics, 180(1), pp.54-77.

144. Vogel, J. V. (1968, January 1). Inflow Performance Relationships for Solution-Gas Drive Wells. Society of Petroleum Engineers. doi:10.2118/1476-PA

145. Wallis, G. B. 1969. One-dimensional Two-phase Flow. McGraw-Hill, New York.

146. Wallis, G.B. 1980. Critical Two-Phase Flow. International Journal of Multiphase Flow. 6(1): p. 97-112.

147. Waltrich, P. J., Falcone, G., & Barbosa Jr, J.R. (2013). Axial Development of Annular, Churn and Slug Flows in a Long Vertical Tube. Int J Multiphase Flow 57: 38–48. http://dx.doi.org/10.1016/j.ijmultiphaseflow.2013.06.008.

148. Waltrich, P. J., Hughes R., Tyagi M., Kam S., Williams W., Cavalcanti de Sousa P. Zulqarnain M., Lee W., & Capovilla S. M. (2015). Experimental Investigation of Two-Phase Flows in Large-Diameter Pipes and Evaluation of Flow Models Applied to Worst-Case-Discharge Calculations, BOEM Report M15PC00007, Craft & Hawkins Department of Petroleum Engineering, Louisiana State University, Baton Rouge.

149. Weisman, J., Duncan, D., Gibson, J., & Crawford, T. (1979). Effects of Fluid Properties and Pipe Diameter on Two-phase Flow Patterns in Horizontal Lines. International Journal of Multiphase Flow, 5(6), pp.437-462.

150. Worst Case Discharge 2016; Available from: http://geminisi.com/?q=consulting/worst-case-discharge.

151. Yuan, Z., Hashemian, Y. & Morrell, D., 2015. Ultra-deepwater blowout well control analysis

under worst case blowout scenario. Journal of Natural Gas Science and Engineering, 27, pp.122-129.

152. Zabaras, G. J, Schoppa, W., Menon, R., and Wicks, M. 2013. Gaps and advancements for deepwater production and remote processing: large diameter riser laboratory gas-lift tests. Offshore Technology Conference. doi:10.4043/23968-MS https://www.onepetro.org/conferencepaper/OTC-23968-MS

153. Zuber, N. & J.A. Findlay (1965). Average Volumetric Concentration in Two-Phase Flow Systems. Journal of Heat Transfer. 87(4): p. 453-468.

154. Zubir, M. A., and M. Z. Zainon. "Two-Phase Flow Behaviour and Pattern in Vertical Pipes." Journal of Applied Sciences 11, no. 9 (2011): 1491-1500.

155. Zangana, M., Van der Meulen, G.P. and Azzopardi, B.J., 2010. The effect of gas and liquid velocities on frictional pressure drop in two phase flow for large diameter vertical pipe. In 7th International Conference on Multiphase Flow, ICMF.

Appendix A: Onshore Blowout Data for the US

Table A. 1 Onshore Blowouts in the US

	Date	Field Name	Remarks
1	10/24/'16	Frye Ranch (consolidated)	Well is being worked over and had wellhead removed when well kicked and blew out.
2	7/6/'16	Penwell	Uncontrolled gas release from an unknown source breaking out to the surface from the outside of the surface casing of the above well.
3	5/3/'16	Lohn (Strawn 900)	Well blowing mud ~ 7 ft. above the rig floor, with mud around the well bore. They were pulling out of the hole preparing to RIH with casing. TD of the well is 994'. There are 450 of drill collars in the hole with a wiper rubber on the drill pipe. Southwest fluids from Abilene is on location with additional mud to kill the well. Well is located ~ 150' north of CR 504. This is a single string completion. The cementers and casing are on location.
4	4/6/'16	Phantom (Wolfcamp)	Well Completed, fracked, and was blowing the well down when it was plugged up. They currently have a rig on well that had been working to unplug the well. The BOP's are shut, and the well is blowing out through a connection that failed below the BOP's.
5	12/15/'15	Salt Flat (Edwards)	Corrosion on a cap on the well caused the blowout.
6	12/3/'15	Loma Novia, NE. (Wilcox)	Closed US-59. Producing well started blowing out.
7	3/11/'15	Eagleville (Eagle Ford - 2)	Blowout while conducting fracing.
8	3/28/'15	East Texas	When pulling tubing and packer got stuck. The well began to flow while working packer, blowing oil out into vacuum truck.
9	1/6/'14	Wasson	The blowout occurred during the drilling of the surface hole.
10	12/16/'14	Phantom (Wolfcamp)	During the flowback and after the frac stimulation the well blew out.
11	12/15/'14	Phantom (Wolfcamp)	The blowout of oil and frac water when operator drilled out of the fracture stimulation. BOP would not close
12	6/6/'13	Chesterville	Well blew out after flowing gas and sand up to the casing. Wild Well Control was sent to the site.

13	4/10/’13	Phantom (Wolfcamp)	Sick line deviation survey was being run when the gas blew out.
14	4/5/’13	Phantom (Wolfcamp)	During the installation of a sub-pump, the well had been killed and the donut lifted when the well blew out.
15	11/5/’12	Kelly-Snyder	During plugging operations well started blowing out through the tubing when the tubing was approximately 10 ft. in the air.
16	8/25/’12	Needville	Well blew out and caught fire.
17	7/6/’12	Begert	Well blew out and caused a fire. Well plugged.
18	6/19/’12	Markham	Workover rig was pulling rods out when well blew out.
19	3/7/’12	Mooringsport (Lime)	Well blew out and caused a fire. Operator pumped in mud to kill the well. Moving rig to bring in a new one and is going to try to complete the well.
20	10/23/’11	Polzer	The blowout occurred while tripping drill string and the new bit in hole.
21	10/3/’11		After perforating at 3850' and pulling out of the hole with the perforating gun to almost the surface the well blew out.
22	7/14/’11	Wildcat	Production tubing sanded up and blew out covering A 2 Acre area.
23	6/27/’11	Spraberry (Trend Area)	Casing had just been completed and BOP was removed to install wellhead when well started to kick and blew out from the side.
24	4/15/’11	Thompson	Hit a gas pocket during drilling and well started blowing gas and mud. Plan is to plug well once all the gas is out of the hole.
25	11/14/’10	Frio	Virtex was drilling new well about 50 +/- feet away from old well and old well blew out. CR 1581 closed.
26	9/29/’10	Hockley	Replacing packing when well blew out. Well pressured up and blew the packing rubbers.
27	9/22/’10	Hardin	Workover operations were finished at 5:00 pm and well appeared to be stable. At around 8:00 a homeowner in the area called in the blowout.
28	11/24/’09	Jim Wells	Well was assumed dead the BOP was removed. Well pressured up and the blowout began.
29	10/26/’09	Carthage, North (Bossier Shale)	Leaking packer was being snubbed out of the well when the tubing parted and well blew out.
30	8/8/’09	Alliance "L" Pad	During drill-out operations they suspect the tubing split and blowout occurred through casing.

31	2/9/’09	Saxet Field	Well kicked when the operator was entering the hole with 2 joints of drill pipe. Considered a short duration blowout; loss of 30bbls.
32	1/9/’09	Wildcat, Mendota Ranch	The blowout occurred during a bit change tip.
33	9/17/’08	Tenaha, South (Cotton Valley) field	The operator was having problems with well; controlling it with 12.3 ppm mud. Closed BOPS and well blew out
34	8/24/’08	Rachel (Cotton Valley Lime)	The person ran over wellhead, causing a blowout
35	5/8/’08		Well blew out through the Kelly, well was being re-completed

Appendix B: Flow loop components

Air Supply System

The air supply system included compressors (C01, C02, and C03), two Coriolis flowmeters (F1 and F2), pressure gauges, bypass valves, and check valves. The compressors had a capacity of 0.76 cubic meters per second at a nominal working pressure of 1.03 MPa. Coriolis flow meters were installed in parallel to measure the upstream air mass flow rates, while the gauge pressures to measure the upstream pressures. Bypass valve (BPV2) on the air flowline was used to dispose of the trapped air in the system to the water tank. The main function of the check valves (CV1) was to avoid the entrance of the water to the air supply line.

Water Supply System

An 11.35 m^3 storage tank was utilized for water supply through primary and secondary pumps. These pumps were guided by Variable Frequency Drives which can deliver the water flow rate of 0.6 m3/min at 1 MPa. The water supply system also consisted of a ball valve, Coriolis flow meter, bypass valve, and check valves. The ball valves were used to connect the primary pump with a water tank which was connected in series with a secondary pump. Coriolis flowmeter was used for flow rate measurement and bypass valve for returning the trapped water to the water tank. The check valve prevents the entrance of air into the water flow line.

(a) (b)

Figure C.1 Centrifugal pumps: (a) Primary; and (b) Secondary

Gas-Liquid Mixing Section

The air-water mixing junction was installed at the bottom of the test section. The air and water were injected into the system through steel pipes having 150 mm and 89 mm, respectively. It is also worthy to note that water is injected through perforated steel plated with different mesh sizes to all the thorough mixing of both phases.

Data Acquisition System

Each instrumentation such as pressure transducers, temperature transmitters, and flowmeters installed on the flow loop was connected to a multi-channel Data Acquisition card, and the data was transmitted in real-time to the connected personal computer. The analog data were converted to digital data, monitored, and recorded through the in-house VBA based Data Acquisition (DAQ) system.

Flowmeters

Overall, three Coriolis flowmeters (Endress Hauser Promass 83F) were installed to measure gas and liquid flow rates at different points of the vertical flow loop as shown in Figure C.2. Two of them were used for measuring the gas flow rate and other for the liquid flow rate. Two of these flow meters had a deliverable capacity of 0 to 1,160 kg/min with an accuracy of ±0.15%. The third flowmeter was comparatively at the lower end of the capacity (0 to 248 kg/min) with the same accuracy as the previous one.

Figure C.2 Coriolis flowmeter

Pressure Sensors

Pressure sensors across the different points of test loops were used to characterize the pressure profiles across the whole section. Two of the differential pressure (DP1 and DP2) transmitters were used for measurement of pressure gradients during the steady-state fluid flow in the test sections. The third DP sensor (L1) was used to measure liquid holdup and installed at the bottom of the test section. The transmitters had the range of -5 to 5 MPa (DP1 and L1) and -1 to 1 KPa (DP2). All these transmitters had an accuracy of 0.05% with an operating temperature of -40 to 105^{o}C.

(a) (b)

Figure C.3 Differential pressure transmitter and (b) Pressure transducer

Temperature Sensors

Two types of six temperature transmitters were installed on the annulus and pipe test sections. The measurement ranges from -50 to 200℃ with accuracy ±0.1-0.2% accuracy.

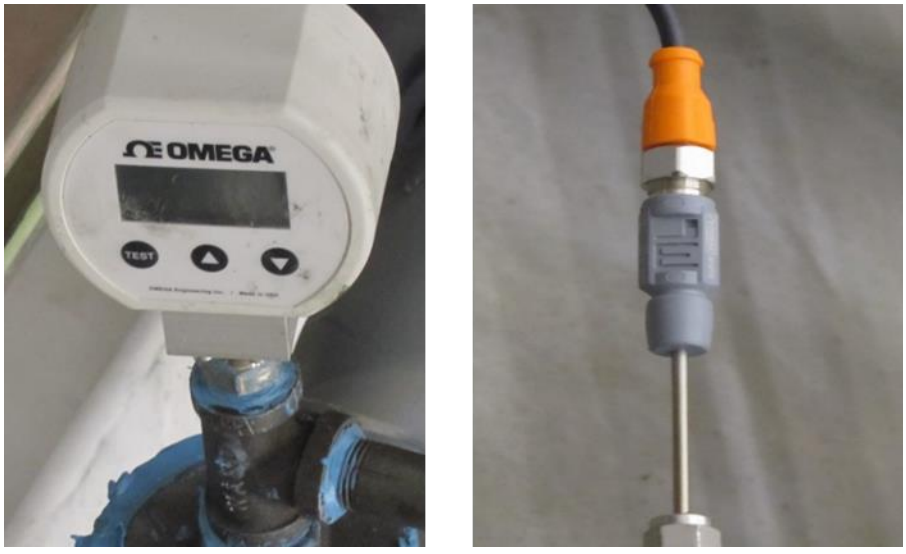

Figure C. 4 Temperature transmitters

Holdup Valves

Figure C.5 Quick closing valves

Four fast reacting butterfly valves were used in the flow loop at different locations to determine the liquid holdup. The valves were controlled through the data acquisition program. These valves had operating temperature and pressure range of -50 to 200℃ and 0-1.6 MPa.

Bypass Valves

Two butterfly valves were also installed to divert the liquid and gas phase to the water tank in case of entrapment of fluid by the abrupt closing of the holdup valves.

Relief Valves

Figure C.6 Relief valve

Two relief valves (Figure C.6) were installed at the exits of the test sections. The relief valves were set to open at 10 bars to avoid over-pressurization and damage to the experimental setup.

Air Compressor

Three air compressors with a standard air capacity of 0.76 cubic meters per second each at 1.03 MPa were utilized during the experiment. The snapshot of the compressors employed to supply air during the experiment is depicted in Figure C.7.

Figure C.7 Air Compressors

Appendix C: Equations for WCD

PVT Models

PVT Properties Calculation for Gas Reservoir

Gas formation volume factor (B_g) can be calculated using equation A.1.

$$B_g = 0.0282\, Z_f\, (T + 460)/P \tag{C.1}$$

where P is the reservoir or wellbore pressure, and T stands for temperature. Z_f is the gas compressibility factor which can be obtained from the concept of reduced gas density as presented in the following equations (Ahmed, 2006):

$$Z_f = \frac{0.27\, P_{pr}}{\rho_r T_{pr}} \tag{C.2}$$

$$P_{pr} = \frac{P}{P_{pc}} \tag{C.3}$$

$$T_{pr} = \frac{T}{T_{pc}} \tag{C.4}$$

$$P_{pc} = 677 + 15\gamma_g - 37.5\gamma_g^2 \tag{C.5}$$

$$T_{pc} = 168 + 325\gamma_g - 12.5\gamma_g^2 \tag{C.6}$$

$$f(\rho_r) = (R_1)\rho_r - \frac{R_2}{\rho_r} + (R_3){\rho_r}^2 - (R_4){\rho_r}^5 + (R_5)\left(1 + A_{11}\,{\rho_r}^2\right) exp\left[-A_{11}\,{\rho_r}^2\right] + 1 \tag{C.7}$$

$$R_1 = \left[A_1 + \frac{A_2}{T_{pr}} + \frac{A_3}{T_{pr}^3} + \frac{A_4}{T_{pr}^4} + \frac{A_5}{T_{pr}^5}\right] \tag{C.8}$$

$$R_2 = \left[\frac{0.27\, P_{pr}}{T_{pr}}\right] \tag{C.9}$$

$$R_3 = \left[A_6 + \frac{A_7}{T_{pr}} + \frac{A_8}{T_{pr}^2}\right] \tag{C.10}$$

$$R_4 = A_9\left[\frac{A_7}{T_{pr}} + \frac{A_8}{T_{pr}^2}\right] \tag{C.11}$$

$$R_5 = \left[\frac{A_{10}}{T_{pr}^3}\right] \tag{C.12}$$

where A_1 = 0.3265, A_2 = -1.0700, A_3 = -0.5339, A_4 = 0.01569, A_5 = -0.05165, A_6 = 0.5475, A_7 = -0.7361, A_8 = 0.1844, A_9 = 0.1056, A_{10} = 0.6134, A_{11} = 0.7210

The gas density is dependent on pressure and temperature and can be calculated using the equation A.13.

$$\rho_g = \frac{M_a P(62.40*1000)}{Z_f R(T+460)} \quad \text{(C.13)}$$

where P is pressure (psia), T is the temperature in °R, R is gas universal constant, and M_a is an apparent molecular weight for gas, given by the following equation:

$$M_a = 29\,\gamma_g \quad \text{(C.14)}$$

where γ_g is gas specific gravity. In addition, the gas viscosity can be calculated using the correlation proposed by (Beggs and Robinson, 1975) as shown below:

$$\mu_g = A \exp\left[B\left(\frac{\rho_g}{1000}\right)^C\right] * 10^{-7} \quad \text{(C.15)}$$

$$A = \frac{9.379+0.01607M_a(T^{1.5}+460)}{209.2+19.26M_a+(T+460)} \quad \text{(C.16)}$$

$$B = 3.448 + \frac{986.4}{T+460} + 0.01009M_a \quad \text{(C.17)}$$

$$C = 2.447 - 0.224 * B \quad \text{(C.18)}$$

PVT Properties Calculation for Oil and Gas Condensate

The solution gas ratio at bubble point pressure is given by the following equation:

$$R_s = \begin{cases} \gamma_g P_b^{1.18026}\left[\text{antilog}_{10}\left\{-1.2179 + 0.4636\left(API/T\right)\right\}\right] \; for\; API \le 30 \\ P_b^{0.94776}\gamma_g^{0.04439}API^{1.1394}\left[\text{antilog}_{10}\left\{-2.188 + 0.0008392T\right\}\right] \; for\; API > 30 \end{cases} \quad \text{(C.19)}$$

where Pb is the bubble point pressure, API is the gravity of the gas, T is the temperature. In addition, the oil formation volume factor (B_o) is calculated by equation C.20.

$$B_o = B_{ob}\exp\left(c_o(P_b - P)\right) \quad \text{(C.20)}$$

$$B_{ob} = 1 + 5.53 * 10^{-7}[R_s(T - 60)] + 1.81 * 10^{-4}R_s\left(\frac{R_s}{\gamma_o}\right) + \frac{4.49*10^{-4}(T-60)}{\gamma_o} + 2.06 *$$

$$10^{-4}\left(\frac{R_s\gamma_g}{\gamma_o}\right) \quad \text{(C.21)}$$

where c_o denotes isothermal compressibility and is calculated as follows:

$$c_o = 10^{(-5.4531+5.03*10^{-4}X-3.5*10^{-8}X^2)} \quad \text{(C.22)}$$

where X is a variable and is influenced by solution gas-oil ratio, pressure, temperature, bubble point pressure, and oil specific gravity. X can be obtained from the following equation:

$$X = R_s^{0.1982}T^{0.6685}\gamma_o^{-0.21435}P_b^{-0.1616} \quad \text{(C.23)}$$

where γo is the specific gravity of oil based on API. Additionally, the oil viscosity is given by the following correlation:

$$\mu_{ob} = 10.715(R_s + 100)^{-0.515}(\mu_{oD})^{5.44(R_s+150)^{-0.338}} \quad \text{(C.24)}$$

where μ_{oD} is dead oil viscosity and can be calculated using the following equation:

$$\mu_{oD} = [3.141(10^{10})](T - 460)^{-3.444}[\log(API)]^{10.313[\log(T-460)]-36.447} \quad \text{(C.25)}$$

PVT Properties Calculation for Water Reservoir

In water reservoirs, water formation factor, density, and water viscosity are the main parameters. Firstly, the water volume formation factor, B_w is given by:

$$B_w = (A_1 + A_2)P + A_3P^2 \quad \text{(C.26)}$$

$$A_1 = \begin{cases} 0.9947 + 5.8 * 10^{-6}T + 1.02 * 10^{-6}T^2 \; for \; P > P_b \\ 0.9911 + 6.35 * 10^{-5}T + 8.5 * 10^{-7}T^2 \; for \; P \leq P_b \end{cases} \quad \text{(C.27)}$$

$$A_2 = \begin{cases} -4.228 * 10^{-6} + 1.8376 * 10^{-8}T - 6.77 * 10^{-11}T^2 for \; P > P_b \\ -1.093 * 10^{-6} - 3.497 * 10^{-9}T + 4.57 * 10^{-12}T^2 \; for \; P \leq P_b \end{cases} \quad \text{(C.28)}$$

$$A_3 = \begin{cases} 1.3 * 10^{-10} - 1.3855 * 10^{-12}T - 4.285 * 10^{-15}T^2 for \; P > P_b \\ -5 * 10^{-11} + 6.429 * 10^{-13}T - 1.43 * 10^{-15}T^2 \; for \; P \leq P_b \end{cases} \quad \text{(C.29)}$$

The viscosity (cP) and density (kg/m^3) of water are calculated using the following correlation given by:

$$\mu_w = \exp^{\left(1.003-1.479*10^{-2}T+1.982*10^{-5}T^2\right)} \quad \text{(C.30)}$$

$$\rho_w = \frac{62.368+0.438603Y+1.60074*10^3Y^2}{62.43*1000} \quad \text{(C.31)}$$

where Y denotes the salt concentration in PPM

Production parameters

Using Darcy's equation, the fluid flow rate can be obtained from a well with a closed outer boundary and is given by the following equation:

$$q_s = J(P_r - P_{wf}) \quad \text{(C.32)}$$

where q_s flowrate (STB/d), J is the productivity index, P_r average reservoir pressure (psia), and P_{wf} is well-flowing pressure (psia). Different types of reservoirs have different productivity index and can be given by the following equations.

Productivity Calculation for Gas Reservoir

$$q_g = \begin{cases} \frac{1.406kk_{rg}\,h\left(\overline{P}/1000*\overline{\mu_g}\overline{Z_f}\right)(P_r-P_{wf})}{(T_R+460)\left[\log\left(\frac{r_e}{r_w}\div 12\right)-0.75+S_k\right]} for\ P_b > 2300\ \text{psi} \\ \frac{0.703kk_{rg}\,h\left(P_r^2-P_{wf}^2\right)}{1000\overline{\mu_g}\overline{Z_f}(T_R+460)\left[\log\left(\frac{r_e}{r_w}\div 12\right)-0.75+S_k\right]} for\ P_b \leq 2300\ \text{psi} \end{cases} \quad \text{(C.33)}$$

where q_g stands for gas production rate in terms of reservoir parameters in STB from (scf /d), k and k_{rg} are absolute and relative gas permeability, h is the thickness of producing gas layer, $\overline{P}$ is an average pressure, $\overline{\mu_g}$ is average gas viscosity, $\overline{Z_f}$ is the average compressibility factor, P_r and P_{wf} are the reservoir and flowing bottom hole pressure, T_R is the reservoir temperature, r_e and r_w are reservoir and wellbore radius, and S_k is skin factor. The average gas PVT properties can be calculated by equations A.34 and A.35. The average viscosity formula is given below:

$$\bar{\mu}_g = \frac{\mu_{gP_r} + \mu_{gP_{wf}}}{2} \quad \text{(C.34)}$$

where μ_{gP_r} and $\mu_{gP_{wf}}$ are gas viscosity at the reservoir and bottom hole pressure conditions. It can be calculated using the PVT gas properties models as described earlier. Furthermore, the average gas compressibility factor ($\bar{Z}_f$) is obtained as follows:

$$\bar{Z}_f = \frac{Z_{P_r} + Z_{P_{wf}}}{2} \tag{C.35}$$

where Z_{fPr} and Z_{fPwf} are compressibility factor at the reservoir and bottom hole conditions, respectively.

Productivity Calculation for Oil Reservoir

Different scenarios can exist in the oil reservoir which impacts the oil flow rate. It can be categorized into three conditions based on reservoir and bottom hole pressure which can be calculated using the following equations:

$$q_o = \begin{cases} \frac{0.00708 k k_o h}{\bar{\mu}_o \bar{B}_o \left[\log\left(\frac{r_e}{r_w} \div 12\right) - 0.75 + S_k\right]} (\bar{P}_r - P_{wf}) for\ \bar{P}_r \text{ and } P_{wf} > P_b \\ \frac{0.00708 k k_o h}{\bar{\mu}_o \bar{B}_o \left[\log\left(\frac{r_e}{r_w} \div 12\right) - 0.75 + S_k\right]} \left(\frac{1}{2P_b}\right) (P_r^2 - P_{wf}^2) for\ \bar{P}_r \text{ and } P_{wf} \leq P_b \\ \frac{0.00708 k k_o h}{\bar{\mu}_o \bar{B}_o \left[\log\left(\frac{r_e}{r_w} \div 12\right) - 0.75 + S_k\right]} \left[\frac{1}{2P_b}\left(P_b^2 - P_{wf}^2\right) + (\bar{P}_r - P_b)\right] for\ P_{wf} \leq P_b\ and\ \bar{P}_r > P_b \end{cases} \tag{C.36}$$

where q_o is oil flow rate in STB/d, $\bar{P}_r$ and P_{wf} are average reservoir and bottom hole pressure, respectively, $\bar{B}_o$ and $\bar{\mu}_o$ are average oil formation factor and oil viscosity, k and k_o are absolute and effective oil permeability, P_b is a bubble point pressure (psi)

$$q_w = \begin{cases} \frac{0.00708 k k_w h}{\bar{\mu}_w \bar{B}_w \left[\log\left(\frac{r_e}{r_w} \div 12\right) - 0.75 + S_k\right]} (P_r - P_{wf}) for\ \bar{P}_r \text{ and } P_{wf} > P_b \\ \frac{0.00708 k k_w h}{\bar{\mu}_w \bar{B}_w \left[\log\left(\frac{r_e}{r_w} \div 12\right) - 0.75 + S_k\right]} \left(\frac{1}{2P_b}\right) (P_r^2 - P_{wf}^2) for\ \bar{P}_r \text{ and } P_{wf} \leq P_b \\ \frac{0.00708 k k_w h}{\bar{\mu}_w \bar{B}_w \left[\log\left(\frac{r_e}{r_w} \div 12\right) - 0.75 + S_k\right]} \left[\frac{1}{2P_b}\left(P_b^2 - P_{wf}^2\right) + (\bar{P}_r - P_b)\right] for\ P_{wf} \leq P_b\ and\ \bar{P}_r > P_b \end{cases} \tag{C.37}$$

where $\bar{B}_w$ and $\bar{\mu}_w$ are average water formation volume factor and average water viscosity, k_w is relative water permeability

$$q_g = \begin{cases} \dfrac{1000(kh)k_{rg}\left(P_r^2 - P_{wf}^2\right)}{1422\bar{\mu}_g\bar{Z}_f 1000(T+460)\left[log\left(\frac{r_e}{r_w}\div 12\right)-0.75+S_k\right]} for\ \bar{P}_r \text{ and } P_{wf} \le P_b \\ \dfrac{1000(kh)k_{rg}\left(P_r^2 - P_{wf}^2\right)}{1422\bar{\mu}_g\bar{Z}_f 1000(T+460)\left[log\left(\frac{r_e}{r_w}\div 12\right)-0.75+S_k\right]} for\ P_{wf} \le P_b\ and\ \bar{P}_r > P_b \end{cases} \quad \text{(C.38)}$$

where k_{rg} is relative gas permeability

Pipe Flow Model (Based on Ansari et al., 1994)

Ansari et al. (1994) developed a comprehensive mechanistic model for pipe flow considering different flow regimes. The bubbly flow regime characteristics are established based on observations of Caetano et al. (1992a; 1992b). The liquid holdup is predicted by solving the following implicit equation:

$$1.53\left[\frac{g\sigma\left(\rho_l - \rho_g\right)}{\rho_l^{\,2}}\right]^{0.25} H_L^{\,0.5} = \frac{V_{sg}}{1-H_L} - 1.2V_M \quad \text{(C.39)}$$

where V_{sg} represents superficial gas velocity, V_m represents mixture velocity, ρ_l is liquid density, ρ_g is the gas density, σ is surface tension of the liquid in the presence of gas, and H_L is the liquid holdup. The pressure gradient is given by the following equation:

$$\left(\frac{dp}{dz}\right)_T = \rho g + \frac{f\rho V^2}{2d} \quad \text{(C.40)}$$

where $(dp/dz)_T$ represents the total pressure gradient, V represents the mixture velocity, d is the pipe diameter of the casing, and f is fanning friction factor.

The slug flow model is developed based on modeling formulations of Caetano et al. (1992a; 1992b). Accordingly, the holdup is calculated by solving the following implicit equation.

$$\left(9.916\sqrt{gd}\right)\left(1-\sqrt{1-H_{LTB}}\right)^{0.5} H_{LTB} - V_{TB}\left(1-H_{LTB}\right) + H_{gLS}V_{TB} + \left(1-H_{gLS}\right) \times\left[V_M - H_{gLS}\left\{1.53\left[\frac{\sigma g\left(\rho_l-\rho_g\right)}{\rho_l^{\,2}}\right]^{0.25}\left(1-H_{gLS}\right)^{0.5}\right\}\right] \quad \text{(C.41)}$$

where H_{gLS} is liquid slug void fraction, H_{LTB} liquid Taylor bubble holdup, V_{TB} is the velocity of the Taylor bubble.

Following a similar modeling procedure, the annular flow model is formulated considering the conservation of mass and momentum. The momentum is conserved for the liquid film. The gas core is assumed a homogenous mixture of gas and entrained liquid droplets moving at the same speed. The final equations comprise of the pressure gradient that can be solved implicitly with the initial guess of dimensionless film thickness.

$$\frac{Z}{4\bar{\delta}\left(1-\bar{\delta}\right)\left(1-2\bar{\delta}\right)^5}\left(\frac{dp}{dz}\right)_{SC}-\left(\rho_L-\rho_C\right)g-\frac{\left(1-Fe\right)^2}{64\bar{\delta}^3\left(1-\bar{\delta}\right)^3}\frac{f_f}{f_{SL}}\left(\frac{dp}{dz}\right)_{SL}=0 \tag{C.42}$$

where Z is the correction factor for interfacial friction. The film thickness is obtained using equations given by Wallis (1969). $\bar{\delta}$ is dimensionless film thickness, $(dp/dz)_{SC}$ is the superficial friction pressure gradient in the core, $(dp/dz)_{SL}$ is the superficial liquid friction pressure gradient, Fe is the entrained liquid fraction in the gas core and calculated using the Wallis equation, f_f is the fanning friction factor in the film, and f_{SL} is the fanning friction factor for the superficial liquid velocity. The non-dimensional form of the Lockhart Martinelli parameter can be applied to determine the total pressure gradient using the following equation:

$$\left(\frac{dp}{dz}\right)_T=\phi_c^{\,2}\left(\frac{dp}{dz}\right)_{SC}+\rho_c g=\phi_F^{\,2}\left(\frac{dp}{dz}\right)_{SL}+\rho_L g \tag{C.43}$$

where the non-dimensional parameter can be calculated using Equations A.44 and A.45.

$$\phi_c^{\,2}=\frac{\left(dp/dz\right)_c-g\rho_c}{\left(dp/dz\right)_{SC}} \tag{C.44}$$

$$\phi_F{}^2 = \frac{\left(dp/dz\right)_F - g\rho_L}{\left(dp/dz\right)_{SL}} \tag{C.45}$$

where $(dp/dz)_T$ is the total pressure gradient, $(dp/dz)_C$ is the pressure gradient in the core, $(dp/dz)_F$ is the pressure gradient in the film.

Appendix D: List of Publications

1. Kiran, R., Salehi, S., Ahmed, R. 2019. Characteristics of Multiphase Flow in Annulus using CFD Modeling and Experimental Studies. Chemical Engineering Research and Design (Manuscript Under Review).

2. Kiran, R. and Salehi, S., 2018, June. Mathematical Modeling and Analysis of Riser Gas Unloading Problem. In ASME 2018 37th International Conference on Ocean, Offshore and Arctic Engineering (pp. V008T11A063-V008T11A063). American Society of Mechanical Engineers.

3. Salehi, S., Madani, S.A. and Kiran, R., 2016. Characterization of drilling fluids filtration through integrated laboratory experiments and CFD modeling. Journal of Natural Gas Science and Engineering, 29, pp.462-468.

4. Salehi, S. Ahmed, R., Elgaddafi, R. and Kiran R. 2019. WCD Literature Review - Research and Development on Critical (Sonic) Flow of Multiphase Fluids through Wellbores in Support of Worst-Case-Discharge Analysis for Offshore Wells, BOEM Report Prepared under Contract Award M16PS00059, Mewbourne School of Petroleum and Geological Engineering, University of Oklahoma, Norman, OK. https://www.boem.gov/WCD-Literature-Review/
5. Salehi, S. Ahmed, R., Elgaddafi, R. and Kiran R. 2019. CFD Modeling Report - Research and Development on Critical (Sonic) Flow of Multiphase Fluids through Wellbores in Support of Worst-Case-Discharge Analysis for Offshore Wells, BOEM Report Prepared under Contract Award M16PS00059, Mewbourne School of Petroleum and Geological Engineering, University of Oklahoma, Norman, OK. https://www.boem.gov/CFD-Modeling-Report/

6. Salehi, S. Ahmed, R., Elgaddafi, R., Fajemidupe, O., and Kiran R. 2019. Experimental Report - Research and Development on Critical (Sonic) Flow of Multiphase Fluids through Wellbores in Support of Worst-Case-Discharge Analysis for Offshore Wells, BOEM Report Prepared under Contract Award M16PS00059, Mewbourne School of Petroleum and Geological Engineering, University of Oklahoma, Norman, OK. https://www.boem.gov/Experimental-Report/

7. Salehi, S. & Kiran, R. 2019. Worst Case Discharge Estimation in Subsonic and Sonic Conditions. Selected for Presentation at IADC Well Control Conference of the Americas & Exhibition, Galveston, TX. August 27-28, 2019.

8. Kiran R., Salehi, S., and Mokhtari, M. 2019. Effect of Irregular shape and Wellbore Breakout on Fluid Dynamics and Wellbore Stability. American Rock Mechanics Association (Manuscript Under Review).

Appendix E: Biography

Raj Kiran is a graduate student currently a Ph.D. candidate in Petroleum Engineering from the Mewbourne School of Petroleum and Geological Engineering at The University of Oklahoma. from the University of Louisiana at Lafayette. He has completed his Master of Science in Engineering with majors in Petroleum Engineering from the University of Louisiana at Lafayette in 2014. He received his Bachelor of Technology in Civil Engineering in 2009 from Indian Institute of Technology, BHU, Varanasi, India. His current research interests focus on the multiphase flow in pipe and annulus, well control operations, human factors in oil and gas operations, and reservoir geomechanics. During his graduate studies, Raj has several peer-reviewed journal and conference papers. Apart from the regular work, he has been a technical reviewer for several journals. He had also worked as Operations Intern for Nabors Drilling in Summer 2018. Prior to his graduate studies, he has worked for three years after his undergraduate in Samsung Engineering (September ’09 – December ’12) with focus on Finite Element Analysis of heavy structures.